

DEPARTMENT OF PHYSICS, UNIVERSITY OF JYVÄSKYLÄ  
RESEARCH REPORT No. ??/2019

**JET TRANSVERSE MOMENTUM DISTRIBUTIONS  
FROM RECONSTRUCTED JETS  
IN P+PB COLLISIONS AT  $\sqrt{s_{\text{NN}}} = 5.02 \text{ TeV}$**

**BY  
TOMAS SNELLMAN**

Academic Dissertation  
for the Degree of  
Doctor of Philosophy

Jyväskylä, Finland  
June 2019

<b>Author</b>	Tomas Snellman University of Jyväskylä Finland
<b>Supervisors</b>	Dr. Kim Dong Jo University of Jyväskylä Finland
	Prof. Jan Rak University of Jyväskylä Finland
<b>Reviewers</b>	Prof. Stefan Bathe Baruch College, CUNY USA
	Prof. Marcin Chrząszcz Instytut Fizyki Jądrowej PAN Poland
<b>Opponent</b>	Prof. Jamie Nagle University of Colorado Boulder USA

<sup>1</sup> \*Acknowledgements

# **Contents**

<b>3</b>	<b>1</b>	<b>Introduction</b>	<b>3</b>
4	1.1	Quantum chromodynamics . . . . .	5
5	1.1.1	Foundation of QCD . . . . .	5
6	1.1.2	Asymptotic Freedom . . . . .	8
7	1.2	Heavy-ion physics . . . . .	10
8	1.2.1	History . . . . .	11
9	1.3	Features of Heavy-Ion Collisions . . . . .	12
10	1.3.1	Collision Geometry . . . . .	12
11	1.3.2	Collective motion . . . . .	16
12	1.4	Hard processes . . . . .	23
13	1.4.1	pQCD factorization . . . . .	23
14	1.4.2	Jet showering . . . . .	25
15	1.4.3	Soft gluon radiation and angular ordering . . . . .	26
16	1.4.4	Jet hadronisation . . . . .	28
17	1.4.5	Interactions between jet and medium . . . . .	32
18	1.4.6	New paradigm of jet Quenching . . . . .	36
19	1.5	QGP in Small systems . . . . .	41
20	1.5.1	Collective phenomena . . . . .	41
21	1.5.2	Absence of jet quenching . . . . .	42
22	1.5.3	Centrality determination in small systems . . . . .	45
<b>23</b>	<b>2</b>	<b>Experimental Setup</b>	<b>48</b>
24	2.1	CERN . . . . .	48
25	2.2	Large Hadron Collider . . . . .	49
26	2.2.1	LHC experiments . . . . .	50
27	2.3	ALICE . . . . .	51
28	2.3.1	Tracking . . . . .	52
29	2.3.2	TPC . . . . .	54
30	2.3.3	Particle identification . . . . .	55
31	2.3.4	Electromagnetic Calorimeter . . . . .	56
32	2.3.5	Forward and trigger detectors . . . . .	57
33	2.3.6	Muon spectrometer . . . . .	59
34	2.3.7	Triggers . . . . .	59
35	2.4	TPC upgrade . . . . .	61
36	2.4.1	ALICE upgrade during LS2 . . . . .	61
37	2.4.2	TPC upgrade . . . . .	61

38	<b>3 Event and track selection</b>	<b>65</b>
39	3.1 Event selection . . . . .	65
40	3.2 Track reconstruction . . . . .	65
41	3.3 Cluster selection . . . . .	69
42	<b>4 Analysis method</b>	<b>71</b>
43	4.1 Jet Finding . . . . .	71
44	4.1.1 Anti $k_T$ algorithm . . . . .	71
45	4.2 Definition of $j_T$ . . . . .	72
46	4.3 Unfolding detector effects . . . . .	74
47	4.3.1 Bayesian unfolding . . . . .	75
48	4.3.2 Toy Monte Carlo . . . . .	77
49	4.3.3 Pythia Response matrices . . . . .	78
50	4.3.4 Unfolding closure test . . . . .	79
51	4.4 Background . . . . .	82
52	4.4.1 Perpendicular cone background . . . . .	82
53	4.4.2 Random background . . . . .	84
54	4.5 Fitting . . . . .	85
55	<b>5 Systematic errors</b>	<b>87</b>
56	5.1 Background . . . . .	87
57	5.2 Unfolding . . . . .	87
58	5.2.1 Effect of number of iterations . . . . .	88
59	5.2.2 Effect of different prior . . . . .	88
60	5.2.3 Effect of $p_T$ truncation . . . . .	88
61	5.3 Tracking . . . . .	91
62	5.4 EMCAL clusters . . . . .	92
63	5.5 Summary of systematic uncertainties . . . . .	94
64	<b>6 Results</b>	<b>95</b>
65	6.1 High multiplicity events . . . . .	97
66	<b>7 Discussion</b>	<b>99</b>
67	7.1 Comparing dihadron and jet $j_T$ results . . . . .	99
68	7.1.1 Different $R$ parameters . . . . .	100
69	7.1.2 Leading tracks versus jet . . . . .	101
70	<b>8 Summary</b>	<b>104</b>

# 71 1 Introduction

72 This thesis focuses on studying Quantum Chromodynamics (QCD) [1], a part of  
73 the standard model of particle physics [2], which is the theory describing the strong  
74 interactions. Strong interaction is the force responsible for interactions that holds  
75 the nucleus of an atom together. Fundamentally it describes the interactions be-  
76 tween quarks and gluons, the elementary constituents of the building blocks of the  
77 nucleus, protons and neutrons. Because of specifics of this interaction quarks and  
78 gluons, together dubbed partons, can never be seen free [3]. Under ordinary con-  
79 ditions they are confined into bound states called hadrons. In extreme conditions  
80 they can form a medium of asymptotically free quarks and gluons, quark-gluon  
81 plasma (QGP) [4].

82 Indirectly quarks can be seen in high energy particle collisions as jets, colli-  
83 mated streams of particles observed in high energy particle collisions [5]. The  
84 physics of these jets is the primary topic discussed in this thesis. Understanding  
85 jets is important when one is interested in the processes that produce the partons  
86 that eventually fragment into jets. By themselves jets can provide an insight into  
87 QCD when the fragmentation is studied. Jets can also be used as probes of the  
88 QGP medium.

89 Experimentally jets are often studied with a jet reconstruction algorithm which  
90 clusters observed tracks to find a reasonable estimate of the initial parton. That is  
91 also the case in this thesis. The main observable studied is the jet fragmentation  
92 transverse momentum  $j_T$  which is defined as the perpendicular component of the  
93 momentum of jet constituents with respect to the jet axis, the best estimate of  
94 the initial parton.  $j_T$  measures the transverse nudge that fragmentation products  
95 receive.

96 The analysis studies collisions between protons and lead nuclei. Originally  
97 meant as a reference for lead-lead collisions to rule out possible cold nuclear mat-  
98 ter effects [6]; effects caused by the regular 'cold' nuclear matter of a nucleus as  
99 opposed to QGP. However, p-Pb collisions have provided interesting physics by  
100 themselves. Many of the collective phenomena that in Pb-Pb collisions were att-  
101 tributed to QGP have been observed also in high multiplicity p-Pb collisions [7]  
102 and even in ultra high multiplicity pp collisions [7]. However observables of jet  
103 modification show no conclusive signals in p-Pb collisions [6, 7].

104 This thesis is organised as follows: Section 1 first gives a general introduction  
105 into the history and properties of QCD and Heavy-Ion physics. It is followed by a  
106 description of hard processes, jet fragmentation and hadronisation and how these  
107 processes might look like in a Heavy-Ion environment. Finally there is a discussion  
108 on the physics of small systems.

109 The experimental setup that was used to collect the data in this thesis is  
110 described in Section 2. It starts by explaining the accelerator facilities at CERN

111 and LHC in more detail. This is followed by a description of the ALICE experiment  
112 and its sub-detectors. A part of Section 2 is dedicated to coming upgrades of  
113 ALICE as this is a timely topic. In 2019-2020 ALICE will be upgraded and I have  
114 made a personal contribution to the TPC upgrade.

115 Section 3 gives a description of the event, track and cluster selection criteria  
116 used in the analysis. This is followed in Section 4 by the specific analysis methods  
117 used in this thesis. First the jet reconstruction algorithm used, anti- $k_T$ , is de-  
118 scribed. Section 4 continues by introducing the  $j_T$  observable, how it is obtained  
119 and what methods are used to estimate background contribution and correct for  
120 detector effects. Finally the fitting method used for the final results is described.  
121 Section 5 gives the different systematic uncertainties that arise from the analysis.

122 Finally the results from the analysis are presented in Section 6. The results  
123 are compared to PYTHIA and Herwig Monte Carlo generators. Further discussion  
124 of the results is given in Section 7 when the results are compared to  $j_T$  results  
125 obtained with a different analysis method. Section 8 summarises the main results  
126 and gives an outlook for future.

127 **1.1 Quantum chromodynamics**

128 **1.1.1 Foundation of QCD**

129 There are four known basic interactions in the universe: gravity, electromagnetic,  
130 weak and strong interactions. The standard model of particle physics [2] includes  
131 three of these, electromagnetic, weak and strong interactions. The fourth one,  
132 gravity, is described well in all but the most extreme of cases by the theory of  
133 general relativity [8]. The standard model is a quantum field theory where particle  
134 interactions are dictated by local gauge symmetries [5].

135 The first interaction included in the standard model was the electromagnetic  
136 interaction. The foundations of quantum field theory and Quantum Electrody-  
137 namics (QED) were already laid out by the work by Dirac in 1927 [9]. The full  
138 theory of QED was formulated in 1946-1949 by Tomonaga [10], Schwinger [11, 12],  
139 Feynman [13]

140 Motivated by the success of a quantum field theory approach for the elec-  
141 tromagnetic interaction physicists started working on the remaining interactions.  
142 However, the weak and strong nuclear interactions proved more challenging to  
143 formulate [14]. In the end the weak interaction was unified with the electromag-  
144 netic interaction into the electroweak theory. The final theory was formulated by  
145 Glashow [15], Salam [16] and Weinberg [17].

146 The theory of strong interactions became to be known as Quantum Chromo-  
147 dynamics (QCD). The search for a theory of strong interactions began after the  
148 formulation of QED and drew further inspiration from the introduction of new  
149 powerful particle accelerators that were capable of particle physics research in the  
150 1950s. Before this particles were mainly discovered from cosmic rays. Positrons,  
151 neutrons and muons were discovered in the 1930s and charged pions were discov-  
152 ered in 1947 [18, 19]. The neutral pion was discovered in 1950 [20].

153 The Lawrence Berkeley National Laboratory started the Bevalac accelerator in  
154 1954, Super Proton Synchrotron (SPS) in CERN began operating in 1959 and the  
155 Alternating Gradient Synchrotron (AGS) at Brookhaven started in 1960. With  
156 an energy of 33 GeV AGS was the most powerful accelerator of that time. By the  
157 beginning of 1960s several new particles had been discovered. These included an-  
158 tiprotons [21], antineutrons [22],  $\Delta$ -particles and the six hyperons ( $\Xi^0$  [23],  $\Xi^-$  [24],  
159  $\Sigma^\pm$  [25],  $\Sigma^0$  [26] and  $\Lambda$  [27]).

160 Facing this avalanche of new particles, physicists started the search for symme-  
161 tries within them. Already in 1932 Heisenberg [28] had proposed an isospin model  
162 to explain similarities between the proton and the neutron. In 1962 Gell-Mann  
163 and Ne’eman presented that particles sharing the same quantum numbers (spin,  
164 parity) could be organised using the symmetry of SU(3). [29] Heisenberg’s Isospin  
165 model followed the symmetry of SU(2). Using the SU(3) model known baryons

<sup>166</sup> and mesons could be presented as octets. This also lead to the discovery of the  
<sup>167</sup>  $\Omega^-$  [30] particle since this was missing from the SU(3) decouplet that included  
<sup>168</sup> heavier baryons.

<sup>169</sup> The most simple representation of SU(3) was a triplet. Inside this triplet  
<sup>170</sup> particles would have electric charges  $2/3$  or  $-1/3$ . However, these had not been  
<sup>171</sup> detected. In 1964 Gell-Mann [31] and Zweig [32] proposed that baryons and mesons  
<sup>172</sup> would be bound states of these three hypothetical triplet particles that Gell-Mann  
<sup>173</sup> called quarks and Zweig called aces. Now we know that these are the  $u$ ,  $d$  and  $s$   
<sup>174</sup> quarks. However, this original quark model without colour was violating the Pauli  
<sup>175</sup> exclusion principle. For example the  $\Omega^-$  particle is comprised of three  $s$  quarks,  
<sup>176</sup> two of which would have exactly the same quantum states, since spin can only  
<sup>177</sup> have two values.

<sup>178</sup> The idea of colour had already been presented by Greenberg in 1964 [33]. In  
<sup>179</sup> 1971 Gell-Mann and Fritzsch presented their model [34], which solved the antisym-  
<sup>180</sup> metry problem. They added a colour quantum number to quarks, which separated  
<sup>181</sup> quarks of the same species. In the new colour model the baryonic wave function  
<sup>182</sup> became

$$(qqq) \rightarrow (q_r q_g q_b - q_g q_r q_b + q_b q_r q_g - q_r q_b q_g + q_g q_b q_r - q_b q_g q_r), \quad (1)$$

<sup>183</sup> The colour model was also supported by experimental evidence. The decay rate  
<sup>184</sup> of a neutral pion with the addition of colours is

$$\Lambda(\pi^0 \rightarrow \gamma\gamma) = \frac{\alpha^2}{2\pi} \frac{N_c^2}{3^2} \frac{m_\pi^3}{f_\pi^2}. \quad (2)$$

<sup>185</sup> For  $N_c = 3$  this gives 7.75 eV and the measured value is  $(7.86 \pm 0.54)$  eV [35].

<sup>186</sup> Another observable that combines the colour information also to the number  
<sup>187</sup> of quark flavours is the Drell-Ratio  $R$  [36]

$$R = \frac{\sigma(e^+ + e^- \rightarrow \text{hadrons})}{\sigma(e^+ + e^- \rightarrow \mu^+ + \mu^-)} = N_c \sum_f Q_f^2. \quad (3)$$

<sup>188</sup> This ratio has the numerical value 2 when including the three light quarks  $u$ ,  $d$   
<sup>189</sup> and  $s$ . When the collision energy reaches the threshold of heavy quark ( $c$  and  
<sup>190</sup>  $b$ ) production processes this increases to  $^{10}/3$  (for  $f = u, d, s, c$ ) and  $^{11}/3$  (for  $f =$   
<sup>191</sup>  $u, d, s, c, b$ ). The energy threshold ( $\sqrt{s} \approx 350$  GeV) of  $t\bar{t}$  production, has not been  
<sup>192</sup> reached so far by any  $e^+e^-$  colliders.

<sup>193</sup> The colour model explained why no free quarks had been observed as only  
<sup>194</sup> colour neutral states are possible. The simplest ways of producing a colour neu-  
<sup>195</sup> tral object are the combination of three quarks, and the combination of a quark-  
<sup>196</sup> antiquark pair. These are known as baryons and mesons.

197      First experimental indication of the existence of quarks came in 1969 when a  
198 series of experiments at the Stanford Linear Accelerator Center (SLAC) revealed  
199 that protons and neutrons appeared to have some substructure [37, 38]. For this  
200 discovery they eventually received the Nobel Prize in Physics in 1990 [39]. Bjorken  
201 demonstrated that these results could be explained if protons and neutrons were  
202 composed of virtually noninteracting pointlike particles [40, 41]. Feynman [42]  
203 interpreted these objects as real particles and suggested they would be the quarks  
204 of Gell-Mann’s model. At the time, however, this seemed mysterious; if all strongly  
205 interacting particles, hadrons, were composed of quarks, then quarks should surely  
206 be strongly interacting themselves. Why would they appear to be almost free  
207 inside hadrons? This turned out to be a key clue in formulating the theory of  
208 strong interactions. [14]

209      After the addition of colour the main ingredients of QCD had been established.  
210 The final quantum field theory of Quantum Chromodynamics formed quickly be-  
211 tween 1972 and 1974. Main part of this was the work by Gross, Wilczek, Politzer  
212 and George for non-abelian gauge field theories [1, 43–46]. The work showed that  
213 quarks would indeed be asymptotically free in a non-abelian theory, which ex-  
214 plained the results from SLAC. Gross, Wilczek and Politzer received the Nobel  
215 Prize in Physics for their work [47]. The role of gluons as a colour octet was pre-  
216 sented by Fritzsch, Gell-Mann and Leutwyler in 1973 [48]. The theory had now 8  
217 massless gluons to mediate the strong interaction.

218      The quark model was extended in 1974 when the discovery of the charm quark  
219 and the first charmed hadron,  $J/\Psi$ , was simultaneously published by teams from  
220 the SLAC [49], from Brookhaven National Laboratory [50] and from the ADONE  
221 collider in Frascati, Italy [51]. In 1976 the Nobel Prize in Physics was awarded to  
222 Richter and Ting for the discovery of the charm quark [52]. The existence of a  
223 fourth quark had already been speculated in 1964 by Bjorken and Glashow [53], but  
224 a proper prediction was provided by Glashow, Iliopoulos and Maiani in 1970 [15]  
225 based on symmetries between leptons and quarks in weak interactions.

226      However, these gluons had not been discovered. Indirect evidence of the ex-  
227 istence had been seen as it was observed that only about half of the momentum  
228 of protons was transported by the quarks [54]. Direct evidence should be seen in  
229 electron-electron collisions as a third, gluonic, jet in addition to two quark jets.  
230 Three jet events were first seen in 1979 at the PETRA accelerator at DESY [55–57].

231      The two remaining quarks, bottom and top, were introduced by Kobayashi  
232 and Maskawa to explain CP-violation [58]. For this they received the Nobel Prize  
233 in Physics in 2008 [59]. Bottom quark was discovered soon after, in 1977, at  
234 Fermilab [60]. The heaviest quark, top quark, would eventually be discovered in  
235 1995 by the CDF [61] and DØ [62] experiments at Fermilab.

236 **1.1.2 Asymptotic Freedom**

237 In Quantum Electrodynamics (QED) the electric charge is screened. In the vicinity  
238 of a charge, the vacuum becomes polarized. Virtual charged particle-antiparticle  
239 pairs around the charge are arranged so that opposing charges face each other.  
240 Since the pairs also include an equal amount opposite charge compared to the  
241 original charge the average charge seen by an observer at a distance is smaller.  
242 When the distance to the charge increases the effective charge decreases until the  
243 coupling constant of QED reaches the fine-structure constant  $\alpha = \frac{1}{137}$ . [5]

244 Contrary to QED, QCD is a non-abelian theory. In other words the generators  
245 of the symmetry group of QCD, SU(3), do not commute. This has the practical  
246 consequence that gluons interact also with other gluons, whereas in QED the  
247 neutral carrier particles, photons, only interact with charged particles. There  
248 is screening also in QCD because of the colour charges, but in addition to that  
249 there is antiscreening because of the gluon interactions. In QCD the antiscreening  
250 effect dominates over screening. Thus for larger distances to the colour charge  
251 the coupling constant is larger. This explains why no free colour charges can be  
252 observed. When the distance between charges increases the interaction strengthens  
253 until it is strong enough to produce a new quark-antiquark pair. On the other  
254 hand, at very small distances the coupling constant approaches zero. This is  
255 called asymptotic freedom. [5]

256 In 1975 Collins [63] predicted a state where individual quarks and gluons are  
257 no longer confined into bound hadronic states. Instead they form a bulk QCD  
258 matter that Edward Shuryak called Quark-Gluon plasma in his 1980 review of  
259 QCD and the theory of superdense matter [4]. QGP can be seen as a separate  
260 state of matter. A schematic view of a phase diagram for QCD matter is shown  
261 in Figure 1.

262 In the early universe at the age of  $10^{-6}$ s after the Big Bang the conditions  
263 preferred the existence of QGP instead of hadronic matter. Nowadays bulk QCD  
264 matter, its properties and its phase transitions between hadronic matter and the  
265 quark-gluon plasma (QGP) can be explored in the laboratory, through collisions  
266 of heavy atomic nuclei at ultra-relativistic energies. The study of QCD matter at  
267 high temperature is of fundamental and broad interest. The phase transition in  
268 QCD is the only phase transition in a quantum field theory that can be probed by  
269 any present or foreseeable technology.

270 One important property of the QGP is the shear viscosity to entropy ratio,  $\eta/s$ .  
271 It is believed that this ratio has an universal minimum value of  $1/4\pi \approx 0.08$ , among  
272 all substances in nature. This limit would be reached in the strong coupling limit  
273 of certain gauge theories [65]. The temperature dependance of the ratio is shown  
274 in Figure 2. The minimum value of  $\eta/s$  is found in the vicinity of the critical  
275 temperature,  $T_c$  [66]. Finding the  $\eta/s$  values in QGP matter would therefore also

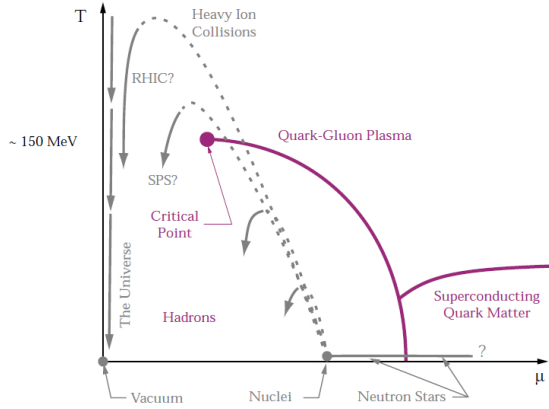


Figure 1: A schematic outline for the phase diagram of QCD matter at ultra-high density and temperature. The quark chemical potential  $\mu$  that is on the x-axis represents the imbalance between quarks and antiquarks. At zero temperature this corresponds to the number of quarks but at higher temperatures there are also additional pairs of quarks and antiquarks. Along the horizontal axis the temperature is zero, and the density is zero up to the onset transition where it jumps to nuclear density, and then rises with increasing  $\mu$ . Neutron stars are in this region of the phase diagram, although it is not known whether their cores are dense enough to reach the quark matter phase. Along the vertical axis the temperature rises, taking us through the crossover from a hadronic gas to the quark-gluon plasma. This is the regime explored by high-energy heavy-ion colliders. [64]

276 provide a way of determining the critical point of QCD matter.

277 The  $\eta/s$  value for the matter created in Au-Au collisions at RHIC ( $\sqrt{s_{NN}} =$   
 278 200 GeV) has been estimated to be  $0.09 \pm 0.015$  [66], which is very close to the  
 279 lowest value for a wide class of thermal quantum field theories [65] for all relativistic  
 280 quantum field theories at finite temperature and zero chemical potential. This  
 281 suggests that the the matter created goes through a phase where it is close to the  
 282 critical point of QCD.

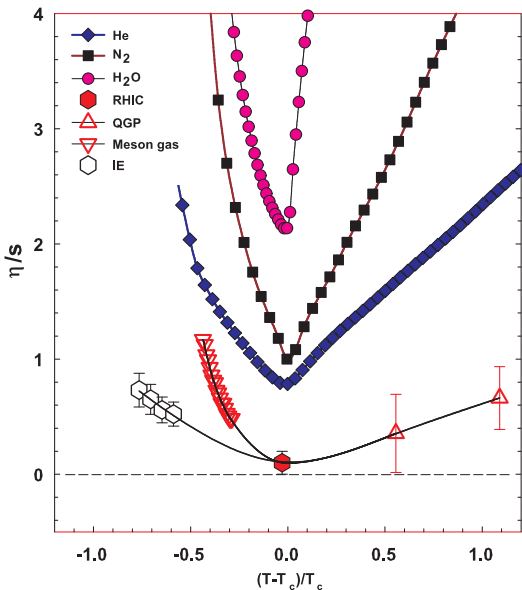


Figure 2:  $\eta/s$  as a function of  $(T - T_c)/T_c$  for several substances as indicated. The  $\eta/s = 0.09 \pm 0.015$  estimate at RHIC comes from Au-Au collisions at  $\sqrt{s_{NN}} = 200$  GeV. The calculated values for the meson-gas have an associated error of  $\sim 50\%$ . The lattice QCD value  $T_c = 170$  MeV is assumed for nuclear matter. The lines are drawn to guide the eye. [66]

## 283 1.2 Heavy-ion physics

284 The Quark Gluon Plasma (QGP) is experimentally accessible by colliding heavy-  
 285 ions at high energies. Nowadays research of Heavy-Ion Collisions is mainly per-  
 286 formed at two particle colliders; The Relativistic heavy-ion Collider (RHIC) at  
 287 BNL in New York, USA and the Large Hadron Collider (LHC) at CERN in Switzer-  
 288 land. Energy densities at these colliders should be enough to produce QGP and  
 289 convincing evidence of the creation has been seen at both colliders. Complimen-  
 290 tary research with heavy nuclei is also performed at the Super Proton Synchrotron  
 291 (SPS) at CERN.

292 The development of heavy-ion physics is strongly connected to the development  
 293 of particle colliders. Experimental study of relativistic heavy-ion collisions has been  
 294 carried out for three decades, beginning with the Bevalac at Lawrence Berkeley  
 295 National Laboratory (LBNL) [67], and continuing with the AGS at Brookhaven  
 296 National Laboratory (BNL) [68], CERN SPS [69], RHIC at BNL and LHC at  
 297 CERN.

298 **1.2.1 History**

299 The first heavy-ion collisions were performed at the Bevalac experiment at the  
300 Lawrence Berkeley National Laboratory [67] and at the Joint Institute for Nu-  
301 clear Research in Dubna [70] at energies up to 1GeV per nucleon. In 1986 the  
302 Super Proton Synchrotron (SPS) at CERN started to look for QGP signatures in  
303 O+Pb collisions. The center-of-mass energy per colliding nucleon pair ( $\sqrt{s_{NN}}$ )  
304 was 19.4 GeV [69]. These experiments did not find any decisive evidence of the  
305 existence of QGP. In 1994 a heavier lead (Pb) beam was introduced for new experi-  
306 ments at  $\sqrt{s_{NN}} \approx 17$  GeV. At the same time the Alternating Gradient Synchrotron  
307 (AGS) at BNL, Brookhaven collided ions up to  $^{32}\text{S}$  with a fixed target at energies  
308 up to 28 GeV [68]. In 2000 CERN [71] presented compelling evidence for the ex-  
309 istence of a new state of matter. Now SPS is used with 400 GeV proton beams  
310 for fixed-target experiments, such as the SPS heavy-ion and Neutrino Experiment  
311 (SHINE) [72], which tries to search for the critical point of strongly interacting  
312 matter.

313 The Relativistic heavy-ion Collider (RHIC) at BNL in New York, USA started  
314 its operation in 2000. The top center-of-mass energy per nucleon pair at RHIC,  
315 200 GeV, was reached in the following years. The results from the experiments at  
316 RHIC have provided a lot of convincing evidences that QGP was created [73–76].  
317 The newest addition to the group of accelerators capable of heavy-ion physics is the  
318 Large Hadron Collider (LHC) at CERN, Switzerland. LHC started operating in  
319 November 2009 with proton-proton collisions. First Pb-Pb heavy-ion runs started  
320 in November 2010 with  $\sqrt{s_{NN}} = 2.76$  TeV, over ten times higher than at RHIC.  
321 Since then LHC has provided both Pb-Pb and p-Pb collisions and a short period  
322 of XeXe collisions. Table 1 shows a summary of these. Among the six experiments  
323 at LHC, the Large Ion Collider Experiment (ALICE) is dedicated to heavy-ion  
324 physics. Also CMS and ATLAS have active heavy-ion programs and LHCb uses  
325 its SMOG [77] to perform unique fixed target collisions with heavy ions.

Table 1: Summary of datasets. The integrated luminosities are from ALICE.

Run 1 (2009-2013)			Run 2 (2015-2018)		
pp	0.9 TeV	$\sim 200 \mu\text{b}^{-1}$	pp	5.02 TeV	$\sim 1.3 \text{ pb}^{-1}$
	2.76 TeV	$\sim 100 \text{ nb}^{-1}$		13.0 TeV	$\sim 25 \text{ pb}^{-1}$
	7.0 TeV	$\sim 1.5 \text{ pb}^{-1}$	p-Pb	5.02 TeV	$\sim 3 \text{ nb}^{-1}$
	8.0 TeV	$\sim 2.5 \text{ pb}^{-1}$		8.16 TeV	$\sim 25 \text{ nb}^{-1}$
p-Pb	5.02 TeV	$\sim 15 \text{ nb}^{-1}$	XeXe	5.44 TeV	$\sim 0.3 \mu\text{b}^{-1}$
Pb-Pb	2.76 TeV	$\sim 75 \mu\text{b}^{-1}$	Pb-Pb	5.02 TeV	$\sim 1 \text{ nb}^{-1}$

326 **1.3 Features of Heavy-Ion Collisions**

327 **1.3.1 Collision Geometry**

328 In contrast to protons atomic nuclei are objects with considerable transverse size.  
329 The properties of a heavy-ion collision depend strongly on the impact parameter  
330  $\vec{b}$  which is the vector connecting the centres of the two colliding nuclei at their  
331 closest approach. One illustration of a heavy-ion collision is shown in Figure 3.

332 Impact parameter defines the reaction plane which is the plane spanned by  $b$   
333 and the beam direction.  $\Psi_{RP}$  gives the angle between the reaction plane and some  
334 reference frame angle. Experimentally the reference frame is fixed by the detector  
335 setup. Reaction plane angle cannot be directly measured in high energy nuclear  
 collisions, but it can be estimated with the event plane method [78].

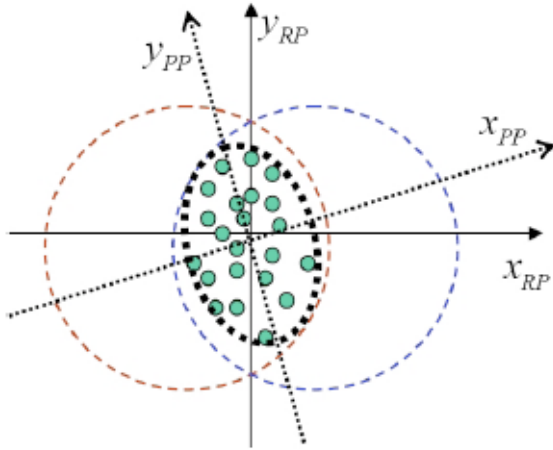


Figure 3: The definitions of the Reaction Plane and Participant Plane coordinate systems [79]. The dashed circles represent the two colliding nuclei and the green dots are partons that take part in the collision.  $x_{PP}$  and  $x_{RP}$  are the participant and reaction planes. The angle between  $x_{RP}$  and  $x_{PP}$  is given by Eq. (4).  $y_{PP}$  and  $y_{RP}$  are lines perpendicular to the participant and reaction planes.

336  
337 Participant zone is the area containing the participants. The distribution of  
338 nucleons in the nucleus exhibits time-dependent fluctuations. Because the nucleon  
339 distribution at the time of the collision defines the participant zone, the axis of  
340 the participant zone fluctuates and can deviate from the reaction plane. The angle  
341 between the participant plane and the reaction plane is defined by [80]

$$\psi_{PP} = \arctan \frac{-2\sigma_{xy}}{\sigma_y^2 - \sigma_x^2 + \sqrt{(\sigma_y^2 - \sigma_x^2)^2 + 4\sigma_{xy}^2}}, \quad (4)$$

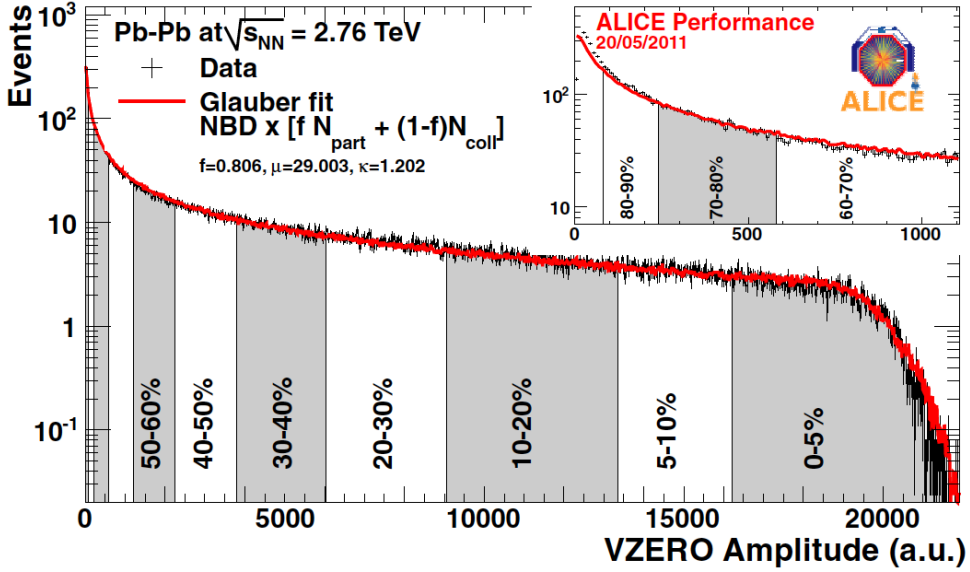


Figure 4: An illustration of the multiplicity distribution in ALICE measurements. The red line shows the fit of the Glauber calculation to the measurement. The data is divided into centrality bins [81]. The size of the bins corresponds to the indicated percentile.

342 where the  $\sigma$ -terms are averaged over the energy density.

$$\sigma_y^2 = \langle y^2 \rangle - \langle y \rangle^2, \sigma_x^2 = \langle x^2 \rangle - \langle x \rangle^2, \sigma_{xy} = \langle xy \rangle - \langle x \rangle \langle y \rangle \quad (5)$$

343 The impact parameter is one way to quantize the centrality of a heavy-ion  
 344 collision but it is impossible to measure in a collision. It can be estimated from  
 345 observed data using theoretical models, but this is always model-dependent and  
 346 to compare results from different experiments one needs an universal definition for  
 347 centrality.

348 Instead in practice centrality is defined by dividing collision events into per-  
 349 centile bins by the number participants or experimentally by the observed mul-  
 350 tiplicity. Centrality bin 0-5% corresponds to the most central collisions with the  
 351 highest multiplicity and higher centrality percentages correspond to more periph-  
 352 eral collisions with lower multiplicities. A multiplicity distribution from ALICE  
 353 measurements [81] illustrating the centrality division is shown in Figure 4. The  
 354 distribution is fitted using a phenomenological approach based on a Glauber Monte  
 355 Carlo [82] plus a convolution of a model for the particle production and a negative  
 356 binomial distribution.

357 The Glauber Model is often used to model the nuclear geometry in a heavy-

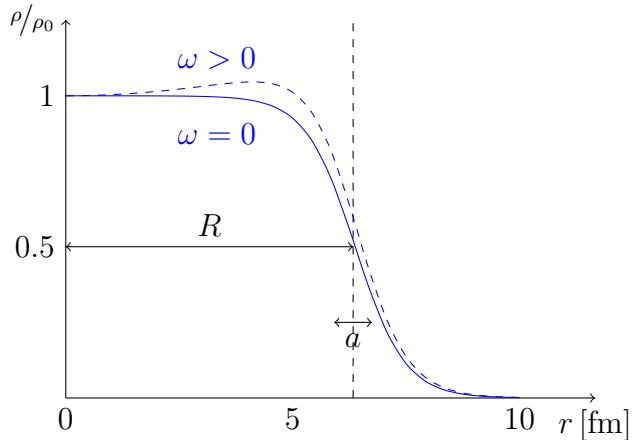


Figure 5: Woods-saxon distribution, with typical values for a Pb nucleus,  $a = 0.55\text{fm}$  and  $R = 6.6\text{fm}$ .

358 ion collision. The model was originally introduced already in 1958 [83] and the  
 359 modern terminology and tools were introduced in 1976 [84] by Białas, Bleszyński,  
 360 and Czyż to model inelastic nuclear collisions.

361 The model starts by defining the thickness function which is the integral of the  
 362 nuclear density over a line going through the nucleus with minimum distance  $s$   
 363 from its center

$$T_A(s) = \int_{-\infty}^{\infty} dz \rho(\sqrt{s^2 + z^2}), \quad (6)$$

364 where  $\rho(\sqrt{s^2 + z^2})$  is the number density of nuclear matter. This can be exper-  
 365 imently determined by studying the nuclear charge distribution in low-energy  
 366 electron-nucleus scattering experiments [82, 85]. For a spherically symmetric nu-  
 367 cleus a good approximation is given by the Woods-Saxon potential [86].

$$\rho(r) = \frac{\rho_0(1 + \omega r^2/R^2)}{1 + \exp(\frac{r-R}{a})}, \quad (7)$$

368 where  $\rho_0$  is the nucleon density in center of the nucleus,  $R$  is the nuclear radius,  
 369  $a$  parametrizes the depth of the skin and  $\omega$  can be used to introduce a surface  
 370 excess. Figure 5 shows how this distribution looks like. With  $\omega = 0$  the density  
 371 stays relatively constant as a function of  $r$  until around  $R$  where it drops to almost  
 372 0 within a distance given by  $a$ .

373 Overlap function is an integral of the thickness functions of two colliding nuclei  
 374 over the overlap area. This can be seen as the material that takes part in the  
 375 collision. It is given as a function of the impact parameter  $b$

$$T_{AB}(\vec{b}) = \int d^2s T_A(\vec{s}) T_B(\vec{s} - \vec{b}) \quad (8)$$

<sup>376</sup> The average overlap function,  $\langle T_{AA} \rangle$ , in an A-A collisions is given by [87]

$$\langle T_{AA} \rangle = \frac{\int T_{AA}(b) db}{\int (1 - e^{-\sigma_{pp}^{inel} T_{AA}(b)}) db}. \quad (9)$$

<sup>377</sup> Using  $\langle T_{AA} \rangle$  one can calculate the mean number of binary collisions

$$\langle N_{coll} \rangle = \sigma_{pp}^{inel} \langle T_{AA} \rangle, \quad (10)$$

<sup>378</sup> where the total inelastic cross-section,  $\sigma_{pp}^{inel}$ , gives the probability of two nucleons  
<sup>379</sup> interacting. As each binary collision has equal probability for direct production  
<sup>380</sup> of high-momentum partons, the number of binary collisions is related to the hard  
<sup>381</sup> processes in a heavy-ion collision. Thus the number of high momentum particles is  
<sup>382</sup> proportional to  $\langle N_{coll} \rangle$  [86, 88, 89]. This required knowledge of  $\sigma_{inel}^{NN}$ , which can be  
<sup>383</sup> measured in proton-proton collisions at different energies. At the LHC the most  
<sup>384</sup> precise cross section measurements come from TOTEM [90].

<sup>385</sup> Soft production on the other hand is related to the number of participants [88].  
<sup>386</sup> It is assumed that in the binary interactions participants get excited and further  
<sup>387</sup> interactions are not affected by previous interactions because the time scales are  
<sup>388</sup> too short for any reaction to happen in the nucleons. After the interactions excited  
<sup>389</sup> nucleons are transformed into soft particle production. The average number of  
<sup>390</sup> participants,  $\langle N_{part} \rangle$  can be calculated from the Glauber model

$$\begin{aligned} \langle N_{part}^{AB}(\vec{b}) \rangle &= \int d^2s T_A(\vec{s}) \left[ 1 - \left[ 1 - \sigma_{NN} \frac{T_B(\vec{s} - \vec{b})}{B} \right]^B \right] \\ &+ \int d^2s T_B(\vec{s}) \left[ 1 - \left[ 1 - \sigma_{NN} \frac{T_A(\vec{s} - \vec{b})}{A} \right]^A \right]. \end{aligned} \quad (11)$$

<sup>391</sup> There are two often used approaches to Glauber calculations. The optical ap-  
<sup>392</sup> proximation is one way to get simple analytical expressions for the nucleus-nucleus  
<sup>393</sup> interaction cross-section, the number of interacting nucleons and the number of  
<sup>394</sup> nucleon-nucleon collisions. In the optical Glauber it is assumed that during the  
<sup>395</sup> crossing of the nuclei the nucleons move independently and they will be essentially  
<sup>396</sup> undeflected.

<sup>397</sup> With increased appreciation of the physics emerging from fluctuations in the  
<sup>398</sup> collision geometry the Glauber Monte Carlo (GMC) approach has emerged as a

method to get a more realistic description of the collisions. In GMC the nucleons  
 are distributed randomly in a three-dimensional coordinate system according to  
 the nuclear density distributions [86]. A heavy-ion collision is then treated as  
 a series of independent nucleon-nucleon collisions, where in the simplest model  
 nucleons interact if their distance in the plane orthogonal to the beam axis,  $d$ ,  
 satisfies

$$d < \sqrt{\sigma_{\text{inel}}^{\text{NN}}} \quad (12)$$

The average number of participants and binary collisions can then be determined  
 by simulating many nucleus-nucleus collisions. The results of one GMC Pb-Pb  
 event with impact parameter  $b = 9.8$  fm is shown in Figure 6

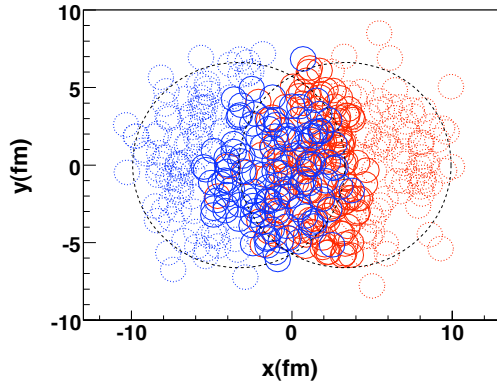


Figure 6: The results of one Glauber Monte Carlo simulation for a Pb–Pb collision. Big circles with black dotted boundaries represent the two colliding nuclei. The participant zone is highlighted with the solid red line. Small red and blue circles represent nucleons. Circles with solid boundaries are participants i.e. they interact with at least one nucleon from the other nucleus. Circles with dotted boundaries are spectators which do not take part in the collision. Figure from [91]

### 1.3.2 Collective motion

Quite often the evolution of a heavy-ion event can be divided into four stages. A schematic representation of the evolution of the collisions is shown in Figure 7.  
 Stage 1 follows immediately the collision. This is known as the pre-equilibrium stage. The length of this stage is not known but it is assumed to last about  $1 \text{ fm}/c$  in proper time  $\tau$ .

The second stage is the regime where thermal equilibrium or at least near-equilibrium is reached. This lasts about  $5 - 10 \text{ fm}/c$  until the temperature of

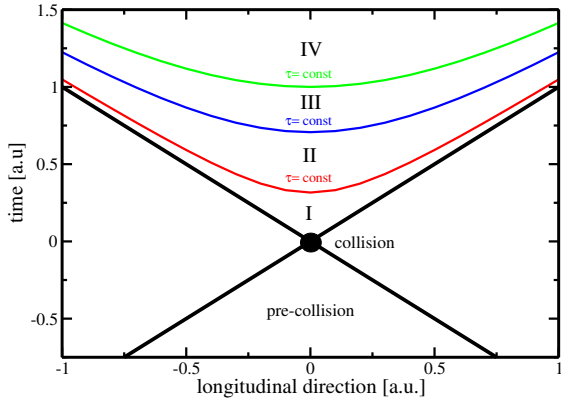


Figure 7: Schematic representation [92] of a heavy-ion collision as the function of time and longitudinal coordinates  $z$ . The various stages of the evolution correspond to proper time  $\tau = \sqrt{t^2 - z^2}$  which is shown as hyperbolic curves separating the different stages.

416 the system sinks low enough for hadronization to occur and the system loses its  
 417 deconfined, strongly coupled state. The third stage is the hadron gas stage where  
 418 the hadrons still interact with each other. This ends when hadron scattering  
 419 becomes rare and they no longer interact. In the final stage hadrons are free  
 420 streaming and they fly in straight lines until they reach the detector.

421 In a heavy-ion collision the bulk collective particle production that is emitted  
 422 from the QGP medium is referred to as flow. After the formation of the QGP, the  
 423 matter begins to expand as it is driven outwards by the strong pressure difference  
 424 between the center of the collision zone and the vacuum outside the collision vol-  
 425 ume. The pressure-driven expansion is transformed into flow of low-momentum  
 426 particles in the hadronization phase. Since the expansion is mainly isotropic the  
 427 resulting particle flow is isotropic with small anisotropic corrections that are of the  
 428 order of 10% at most. The isotropic part of flow is referred to as radial flow.

429 The transverse momentum spectra  $dN/dp_T$  in heavy-ion collisions is shown in  
 430 Figure 8. The vast majority of produced particles have small  $p_T$ . The difference  
 431 between the yield of 1 GeV/c and 4 GeV/c particles is already 2-3 orders of mag-  
 432 nitude. Any observables that are integrated over  $p_T$  are therefore dominated by  
 433 the small momentum particles.

434 The geometry of the heavy-ion collision produces an anisotropic component to  
 435 the collective motion. In a non-central heavy-ion collision, with a large impact  
 436 parameter, the shape of the impact zone is almond-like. In a central collision  
 437 the overlap region is almost symmetric in the transverse plane. In this case the  
 438 impact parameter is small. Collisions with different impact parameters are shown  
 439 in Figure 9.

440 The pressure gradient is largest in-plane, in the direction of the impact parameter  $b$ , where the distance from high pressure, at the collision center, to low  
 441 pressure, outside the overlap zone, is smallest. This leads to stronger collective  
 442 flow along the direction of  $b$ , which in turn results in enhanced thermal emission  
 443 through a larger effective temperature into this direction, as compared to out-of-  
 444 plane [94–96]. The resulting flow is illustrated in Figure 9.

446 Flow is typically quantified in the form of a Fourier composition

$$E \frac{d^3N}{dp^3} = \frac{1}{2\pi p_T} \frac{d^2N}{dp_T d\eta} \left( 1 + \sum_{n=1}^{\infty} 2v_n(p_T, \eta) \cos(n(\phi - \Psi_n)) \right), \quad (13)$$

447 where the coefficients  $v_n$  give the relative strengths of different anisotropic flow

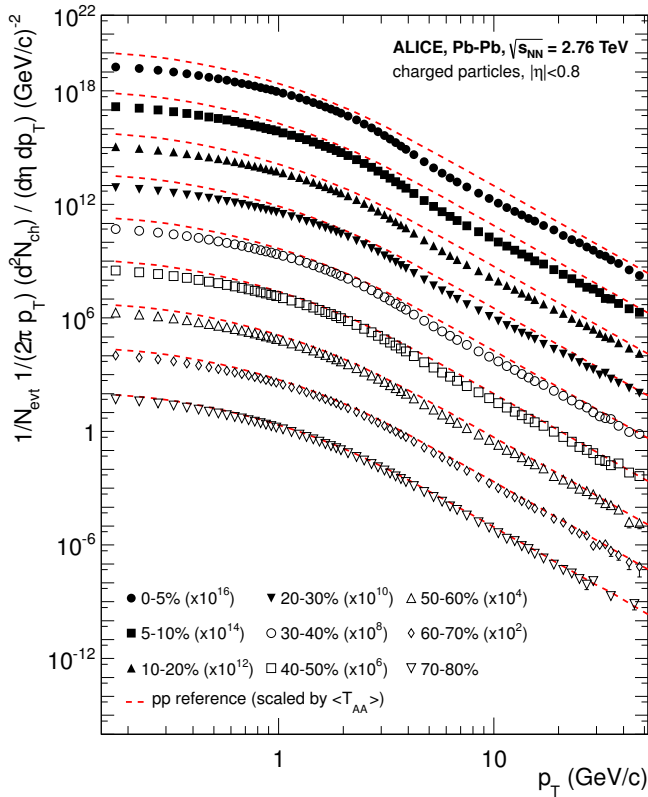


Figure 8: Charged particle spectra measured by ALICE [93] for the 9 centrality classes given in the legend. The distributions are offset by arbitrary factors given in the legend for clarity. The distributions are offset by arbitrary factors given in the legend for clarity. The dashed lines show the proton-proton reference spectra scaled by the nuclear overlap function determined for each centrality class and by the Pb-Pb spectra scaling factors [93].

448 components and the overall normalisation gives the strength of radial flow. Elliptic  
 449 flow, i.e. flow with two maxima, is represented by  $v_2$  and  $v_3$  represents triangular  
 450 flow. The first coefficient,  $v_1$ , is connected to directed flow [97]. This will however  
 451 in total be zero because of momentum conservation. It can be nonzero in some  
 452 rapidity or momentum regions but it must be canceled by other regions.

453 In a peripheral collision  $v_2$  is the dominant part of anisotropic flow as it arises  
 454 from the asymmetric geometry of the collision region. Higher harmonics, the  
 455 most notable of which is the triangular flow, come from fluctuations in the initial  
 456 conditions [98]. As the colliding nuclei are not static objects, the arrangement of  
 457 the nucleons at the time of the collision is random. The shape of the collision zone  
 458 is not a perfect almond. Instead it can have a more complex shape. Also inside  
 459 the collision zone the density of the created medium is not homogenous but it can  
 460 have denser hot spots

461 It has been noted that higher harmonics of  $v_n$  would be suppressed by vis-  
 462 cos effects and that the shape of  $v_n$  as a function of  $n$  would provide another  
 463 valuable tool for studying  $\eta/s$  [99]. For a long time it was believed that the odd  
 464 harmonics would be negligible. In 2007 Mishra et al. [100] argued that density  
 465 inhomogeneities in the initial state would lead to non-zero  $v_n$  values for higher  
 466 harmonics including  $v_3$ .

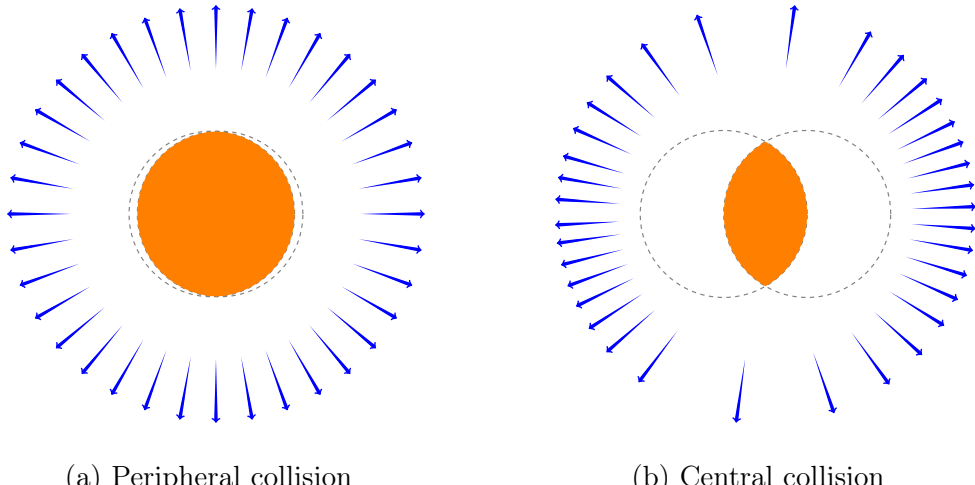
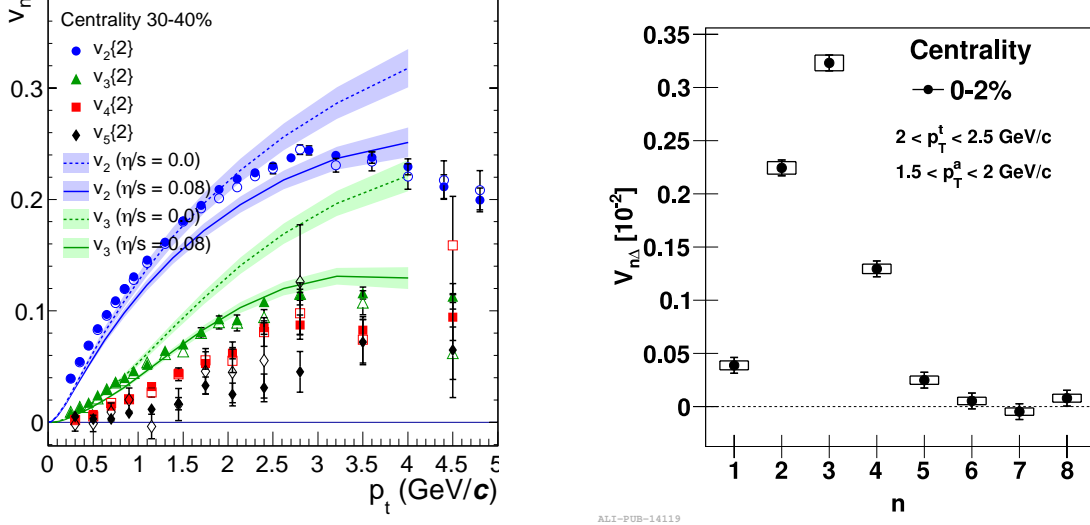


Figure 9: Illustration of flow in momentum space in central and peripheral collisions. The density of the arrows represent the magnitude of flow seen at a large distance from the collision in the corresponding azimuthal direction. In a peripheral collision momentum flow into in-plane direction is strong and flow into out-of-plane direction is weak. In a central collision anisotropy in flow is smaller, but the total yield of particles is larger.



(a) ALICE measurement of  $v_2, v_3, v_4, v_5$  as a function of transverse momentum. The flow coefficients are determined by two-particle correlations using different rapidity separations. The full and open symbols are for  $\Delta\eta > 0.2$  and  $\Delta\eta > 1.0$ . The results are compared to hydrodynamic predictions [102] with different values of  $\eta/s$  [103].

(b) Amplitude of  $v_n$  harmonics as a function of  $n$  for the 2% most central collisions as measured by ALICE [104].

Figure 10: Flow measurements of higher harmonics

467 The first one to predict anisotropic flow in heavy-ion collisions was Ollitrault  
 468 in 1992 [94]. However, the first papers on anisotropy did not discuss the Fourier  
 469 composition. Instead they approached the problem with a classic event shape  
 470 analysis. (sphericity) The first experimental studies of anisotropy were performed  
 471 at the AGS [101] in 1993, where it was noted that the anisotropy of particle  
 472 production in one rapidity region correlates with the reaction plane angle defined  
 473 in another rapidity region. The first ones to present the Fourier decomposition  
 474 were Voloshin and Zhang in 1996 [97]

475 Measurements of different flow harmonics are shown in Figure 10. The left  
 476 panel shows different flow harmonics as a function of  $p_T$  as measured by AL-  
 477 ICE [103] in peripheral collisions. In general flow coefficients decrease as a function  
 478 of  $n$  after  $n = 2$ . Central collisions are an exception. The right panel of Figure 10  
 479 shows  $v_n$  as a function of  $n$  in central collisions as measured by ALICE [104]. The  
 480 results are compared to hydrodynamic predictions [102].

481        The measured collective flow in heavy-ion collisions has been successfully mod-  
482        elled with the relativistic version of hydrodynamics. The power of relativistic  
483        hydrodynamics lies in its simplicity and generality. Hydrodynamics only requires  
484        that there is local thermal equilibrium in the system. In order to reach thermal  
485        equilibrium the system must be strongly coupled so that the mean free path is  
486        shorter than the length scales of interest, which is assumed to hold for QGP phase  
487        of a heavy-ion collision [92].

488        The use of relativistic hydrodynamics in high-energy physics dates back to  
489        Landau [105] and the 1950's, before QCD was discovered. Back then it was used  
490        in proton-proton collisions. Development of hydrodynamics for the use of heavy-  
491        ion physics has been active since the 1980's, including Bjorken's study of boost-  
492        invariant longitudinal expansion and infinite transverse flow [106]. Major steps  
493        were taken later with the inclusion of finite size and and dynamically generated  
494        transverse size [107, 108], a part of which was done at the University of Jyväskylä.

495        Understanding of the properties of the QGP has been improved with the help  
496        of new data from LHC and RHIC and theoretical developments over the years.  
497        For example, as shown in Figure 11(a), the quantification of the temperature de-  
498        pendence shear viscosity over entropy ratio has been tested with event-by-event  
499        Eskola-Kajantie-Ruuskanen-Tuominen (EKRT) + viscous hydrodynamic calcula-  
500        tions [109], where the first qualitative possibilities were investigated. In this hy-  
501        drodynamic calculations, the initial energy density profiles are calculated using a  
502        next-to-leading order perturbative-QCD + saturation model (EKRT) [110, 111].  
503        The subsequent space-time evolution is described by relativistic dissipative fluid  
504        dynamics with different parametrisations for the temperature dependence of the  
505        shear viscosity to entropy density ratio  $\eta/s(T)$ . This model gives a good descrip-  
506        tion of the charged hadron multiplicity and the low- $p_T$  region of the charged hadron  
507        spectra at RHIC and the LHC [109]. Each of the  $\eta/s(T)$  parametrisations have  
508        been adjusted to reproduce the measured  $v_n$  from central to mid-peripheral col-  
509        lisions. The model calculations in which the temperature of the phase transition  
510        is larger than for "param1" are ruled out by the previous measurements [112] and  
511        their studies. The remaining two sets of parameters which described most of data  
512        is labeled as "best fits" in Figure 11(a). For the "param1" parametrisation the  
513        phase transition from the hadronic to the QGP phase occurs at the lowest temper-  
514        ature, around 150 MeV. This parametrisation is also characterised by a moderate  
515        slope in  $\eta/s(T)$  which decreases (increases) in the hadronic (QGP) phase.

516        The estimation of the  $\eta/s$  has been also established with Bayesian analysis,  
517        which is applied to form the initial conditions with no assumptions on the physi-  
518        cal mechanisms of the entropy production [113]. The robust statistical analytical  
519        methods allows performing the model to data calibration in a multi-dimensional  
520        parameter space. In addition to finding the most likely combination of input pa-

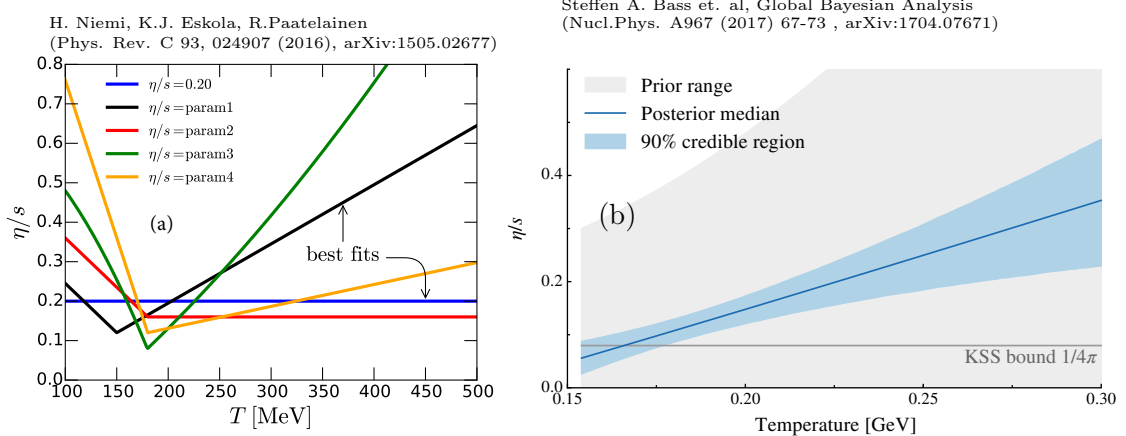


Figure 11: Temperature dependence of  $\eta/s$ . *left:* Different parametrisations of  $\eta/s(T)$  that have been tested in hydrodynamical simulations. *right:* Result of a global Bayesian analysis narrowing down the possible  $\eta/s(T)$  behaviour [113]

521 parameters, the Bayesian statistical method also provides the full uncertainty quan-  
 522 tification in the form of posterior probability distributions for all the parameters.  
 523 The resulting  $\eta/s(T)$  parametrisation is shown in Figure 11(b).

524 Based on the aforementioned model calculations, the phase transition from the  
 525 hadronic to the QGP phase occurs at the lowest temperature, around 150 MeV.  
 526 Although the temperature dependence of the  $\eta/s$  is currently not well known, the  
 527 calculations generally suggest a minimum value of  $\eta/s$  from 0.08 to 0.12, close to  
 528 the universal limit  $1/(4\pi)$  [65].

529 Recently, several advancements have been made in order to further constrain  
 530 the temperature dependence of  $\eta/s$ . New observables, such as the symmetric  
 531 cumulants [112, 114], have provided detailed information on the temperature de-  
 532 pendence over the evolution of the QGP. Furthermore, the non-linear formalism  
 533 has resulted in remarkable new constraints on the initial conditions [115], and the  
 534  $\eta/s$  at the freeze-out conditions, for which is among the least understood parts of  
 535 hydrodynamic calculations.

536 **1.4 Hard processes**

537 **1.4.1 pQCD factorization**

538 The term Hard Scattering is used in connection with the scattering of two point-  
539 like constituents (partons) of colliding nucleons, when the momentum transfer  $Q^2$   
540 is large ( $Q \gg \Lambda_{\text{QCD}}$ ). Figure 12 shows the incoming partons, quarks or gluons, as  
541 they exchange a space-like virtual gluon and produce two highly virtual outgoing  
542 partons. The outgoing partons will eventually fragment into collimated showers of  
543 partons, referred to as jets.

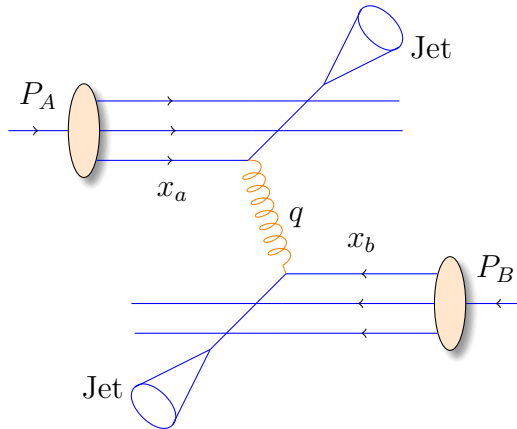


Figure 12: Schematic view of hard scattering process between 2 protons, producing 2 jets

544 Historically one would study hard scatterings foremost with inclusive hadron  
545 spectra. In this context hadron production from hard scatterings can be factorised  
546 into three components; the parton distribution functions  $f_a$ ,  $f_b$  that give the prob-  
547 ability of getting a parton with momentum fraction  $x$  of the proton, the cross  
548 section of the elementary scattering  $ab \rightarrow cd$ , and the fragmentation functions  
549 that give the probability of getting hadron  $h$  from the parton.

$$\frac{d\sigma_{pp}^h}{dy d^2p_T} = K \sum_{abcd} \int dx_a dx_b f_a(x_a, Q^2) f_b(x_b, Q^2) \frac{d\sigma}{dt} (ab \rightarrow cd) \frac{D_{h/c}^0}{\pi z_c}, \quad (14)$$

550 where

$$x_{a,b} = \frac{|p_{a,b}|}{|p_{\text{proton}}|}. \quad (15)$$

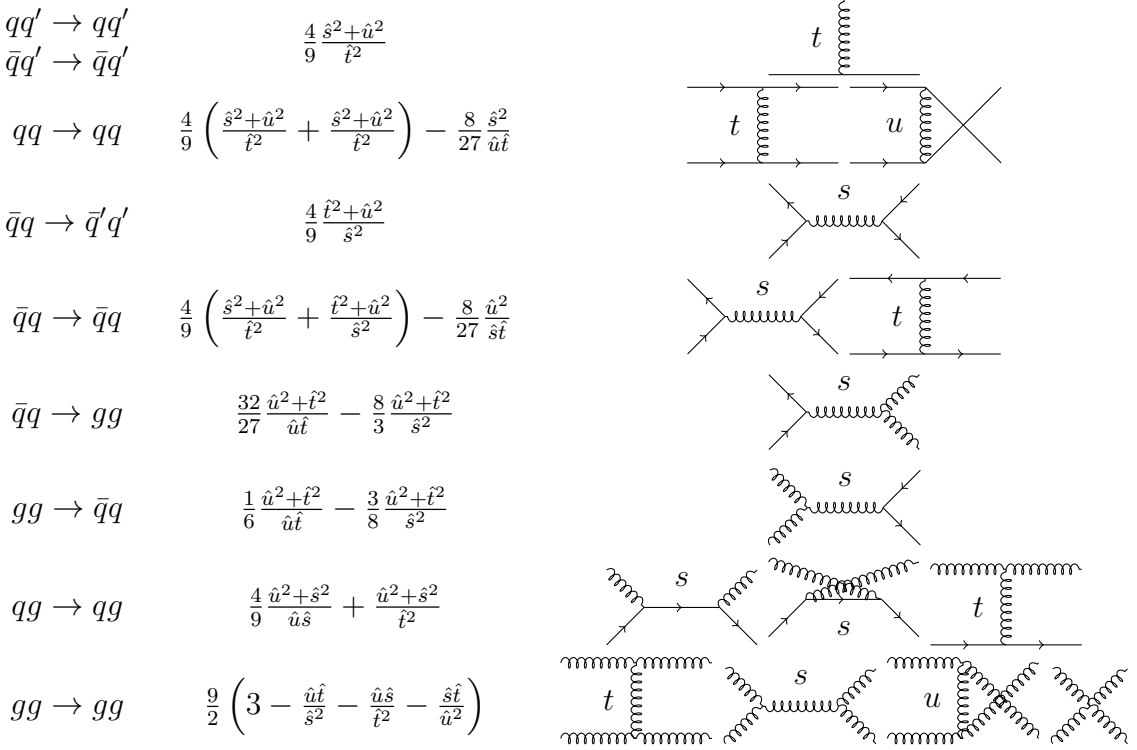


Figure 13: The basic pQCD processes and their quadratic matrix elements

551 Parton distribution functions will be discussed further in the following section.  
 552 The elementary cross section  $ab \rightarrow cd$  can be calculated from QCD. A summary  
 553 of the first order  $2 \rightarrow 2$  processes in QCD is shown in Figure 13.

554 The final component in the factorization, fragmentation functions, describe the  
 555 distribution of the fractional momenta of fragments radiated from the outgoing  
 556 parton. In a leading order picture, it can be interpreted as the probability that  
 557 the observed final state originates from a given parton [116]. Like the PDFs they  
 558 are non-perturbative and must be determined experimentally. The measurement  
 559 is usually performed in  $e^+e^-$  collisions where the kinematics are better controlled.

## 560 Parton Distribution Function

561 Parton Distribution Functions (PDFs)  $f_a(x)$  give the differential probability for  
 562 parton  $a$  to carry momentum fraction  $x$  of the proton momentum. As the PDFs  
 563 cannot be calculated from first principles they are measured in Deeply Inelastic  
 564 Scattering (DIS) experiments [117] and are extrapolated to the relevant momen-  
 565 tum scales using the Dokshitzer-Gribov-Lipatov-Altarelli-Parisi (DGLAP) evolu-  
 566 tion scheme [118–120]

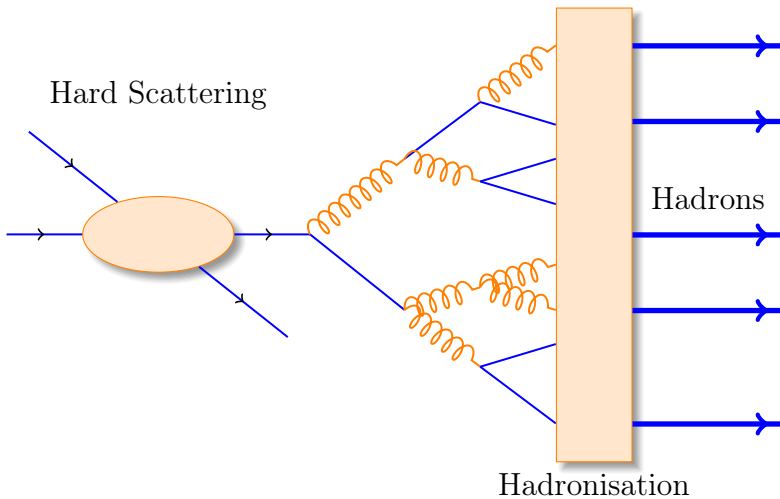


Figure 14: An illustration of jet showering. The highly virtual parton from the hard scattering will produce a shower of softer partons. When the virtuality is low enough the shower will go through a hadronisation process that produces the hadrons, which will be eventually observed in the detector.

$$\mu_F^2 \frac{\partial f_i(x, \mu_F^2)}{\partial \mu_F^2} = \sum_j \frac{\alpha_s(\mu_F)}{2\pi i} \int_x^1 \frac{dz}{z} P_{ij}(z) f_j\left(\frac{x}{z}, \mu_F^2\right), \quad (16)$$

where  $\mu_F$  is a factorization scale. The splitting functions  $P_{ij}$  describe a probability to radiate parton  $i$  from parton  $j$  as a function of the momentum fraction  $z$  carried away by the offspring parton. Different theory interpretation and experimental data gives rise to different PDF's. Thus there are several commonly used PDF sets: CTEQ [121], HERAPDF [122], PDF4LHC [123], etc.

#### 1.4.2 Jet showering

More detailed studies of the hard processes require a formulation of the showering process. The full picture is a complicated  $2 \rightarrow n$  scattering, but it is typically seen as a series of  $1 \rightarrow 2$  splittings with decreasing virtuality following the initial  $2 \rightarrow 2$  scattering [124].

To first order the cascade is governed by the DGLAP evolution equation [118–120]

$$dP_a(z, Q^2) = \frac{dQ^2}{Q^2} \frac{\alpha_s}{2\pi} P_{a \rightarrow bc}(z) dz, \quad (17)$$

which gives the differential probability that parton  $a$  (mother) will branch to two partons  $b$  and  $c$  (daughters), at a virtuality scale  $Q^2$ . Daughter  $b$  takes a fraction

$z$  of the parton  $a$  energy and daughter  $c$  takes energy fraction  $1 - z$ . The splittings kernels  $P_{a \rightarrow bc}(z)$  are

$$P_{q \rightarrow qg}(z) = \frac{4}{3} \frac{1+z^2}{1-z} \quad (18)$$

$$P_{g \rightarrow gg}(z) = 3 \frac{(1-z)(1-z)^2}{z(1-z)} \quad (19)$$

$$P_{g \rightarrow q\bar{q}}(z) = \frac{n_f}{2} (z^2 + (1-z)^2), \quad (20)$$

where  $n_f$  is the kinematically allowed number of quark flavours. There is some freedom in how the evolution variable  $Q^2$  is chosen. If  $Q^2 = f(z)m^2$  and  $f(z)$  is a positive and a smooth function it holds that

$$\frac{dQ^2}{Q^2} dz = \frac{dm^2}{m^2} dz. \quad (21)$$

Of the Monte Carlo generators used in this thesis PYTHIA uses  $m^2$  as the evolution variable [125], while HERWIG uses an energy-weighted emission angle  $E^2(1 - \cos \theta) \approx m^2/z(1-z)$  [126].

Formally eq 17 corresponds to the emission of an infinite number of partons. However very soft and collinear gluons need not be considered and one can introduce an effective cut-off scale  $Q_0$ , usually taken to be of the order of 1 GeV.

Going further one approach is to introduce time ordering, i.e. to decide which of the emissions occurs first. This is done in the form of a Sudakov form factor [127]

$$P_a^{no}(Q_{\max}^2, Q^2) = \exp \left( - \int_{Q^2}^{Q_{\max}^2} \int_{z_{\min}}^{z_{\max}} dP_a(z', Q'^2) \right), \quad (22)$$

which gives the probability that no emissions occur between the initial maximum scale  $Q_{\max}^2$  and a given  $Q^2$  and within limits  $z_{\min} < z < z_{\max}$ . Thus the probability for the first branching to occur at  $Q^2 = Q_a^2$  is given by

$$d\Delta_a(z, Q_a^2, Q_{\max}^2) = dP_a(z, Q_a^2) P_a^{no}(Q_{\max}^2, Q_a^2). \quad (23)$$

Partons  $b$  and  $c$  that were produced will further branch with maximum virtuality scale  $Q_{\max}^2$  given by  $Q_a^2$ . Similarly their daughters will continue branching until the cutoff scale is reached, thus producing a shower.

#### 1.4.3 Soft gluon radiation and angular ordering

Let us now consider a case where a gluon splits into two quarks, and one of the created quarks emits a soft gluon as seen in Figure 15. In the laboratory frame the time it takes for a gluon to be emitted from a quark can be estimated to be [128]

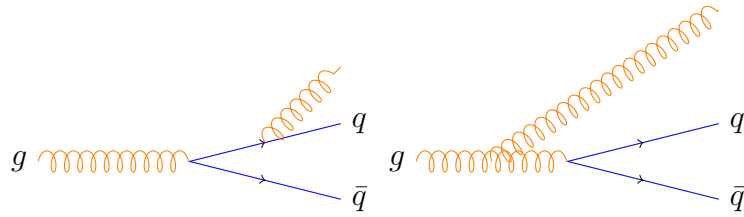


Figure 15: Soft gluon production

$$t_{\text{emit}} \approx \frac{1}{E_q}, \quad (24)$$

where the energy of the quark is given by  $E_q$ . In the rest frame of the quark its energy is given by its virtuality  $M_{\text{virt}}$  and assuming the quark is massless the Lorentz factor between the rest frame the laboratory frame is

$$\gamma = \frac{E_q}{M_{\text{virt}}}. \quad (25)$$

Thus the emission time can be written as

$$t_{\text{emit}} \approx \frac{E_q}{M_{\text{virt}}^2} = \frac{E_q}{(k + p)^2}, \quad (26)$$

where  $k$  and  $p$  are the four-momenta of the gluon and the quark after the gluon emission. This can be written open in the laboratory frame. Through assuming that the end products are massless and Taylor-expanding the resulting cosine term gives a form that expresses the emission time using the opening angle  $\theta_{kq}$  between the quark and the gluon

$$t_{\text{emit}} \approx \frac{1}{k\theta_{kq}^2}. \quad (27)$$

The transverse wavelength of the emitted gluon is  $\lambda_{\perp}^{-1} = k_{\perp} \approx k\theta_{kq}$ . Thus we get

$$t_{\text{emit}} \approx \frac{\lambda_{\perp}}{\theta_{kq}}. \quad (28)$$

The secondary gluon can only probe the quark of the earlier splitting if the transverse wavelength is smaller than the transverse separation of the produced  $q\bar{q}$  pair. The transverse separation is given by

$$r_{\perp}^{q\bar{q}} \approx \theta_{q\bar{q}} t_{\text{emit}} \approx \lambda_{\perp} \frac{\theta_{q\bar{q}}}{\theta_{kq}}. \quad (29)$$

613 Thus in order for the emission to probe the individual quark, the opening angle  
614 of the  $q\bar{q}$  splitting,  $\theta_{q\bar{q}}$ , must be larger than  $\theta_{kq}$ . If the opening angle  $\theta_{kq}$  is larger,  
615 the gluon can't distinguish between the quark and the antiquark, so it probes the  
616 state of the system before the splitting, i.e. it can be treated like it was emitted  
617 from the primary gluon.

618 This leads to the angular ordering of soft gluon radiation. Each successive angle  
619 must be smaller than the previous one. The effect can be calculated in all orders  
620 [128] and in the DGLAP formalism one can select the evolution variable  $Q^2$  in a  
621 way that ensures angular ordering as is done in the Herwig MC generator [126].  
622 In PYTHIA 8 this is strictly not included, but the transverse momentum ordered  
623 showers are as accurate in describing the soft gluon emissions as the angular or-  
624 dered showers [127].

#### 625 1.4.4 Jet hadronisation

626 When the virtuality of the shower is low enough, the shower starts to hadronise. In  
627 this regime the parton shower reaches a scale close to  $\Lambda_{\text{QCD}}$  and the perturbative  
628 description is no longer valid. Thus the hadronisation stage must be described in a  
629 non-perturbative manner. In general hadronisation is assumed to be universal, i.e.  
630 it shouldn't depend on the collision energy or system. The most simple scenario  
631 that is used in several theory calculations is the so-called local parton-hadron  
632 duality [129]. In the local parton-hadron duality hypothesis it is assumed that  
633 there exists a low virtuality scale  $Q_0$  in which the hadronisation happens, that is  
634 independent of the scale of the primary hard process. At this scale the partons  
635 are transformed into hadrons, assuming that the flow of momentum and quantum  
636 numbers for the hadrons can be directly obtained from those of partons introducing  
637 only small normalising constants.

638 The next sections will present more complicated hadronisation models used in  
639 Monte Carlo generators, PYTHIA and Herwig.

#### 640 Lund string model

641 One common implementation in MC generators is the Lund string fragmentation  
642 algorithm [130]. The string model is based on the fact that in QCD linear confine-  
643 ment is expected over large distances [127]. This can be modelled by imagining  
644 a colour flux tube being stretched between the outgoing partons. The left side of  
645 Figure 16 illustrates this point for a  $q\bar{q}$ -pair. The tube is assumed to have a uni-  
646 form fixed transverse size of about 1 fm along its length, which leads to a linearly  
647 rising potential  $V(r) = \kappa r$ , where the string constant  $\kappa$  describes the amount of  
648 energy per unit length. A value of  $\kappa \approx 1 \text{ GeV/fm} \approx 0.2 \text{ GeV}^2$  can be obtained  
649 from hadron mass spectroscopy [127].

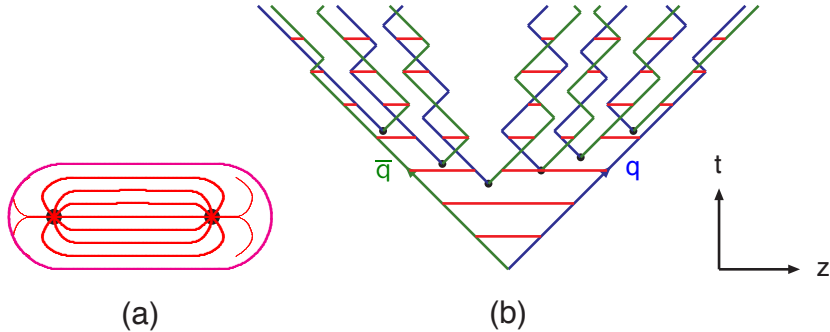


Figure 16: (a) A flux tube spanned between a quark and an antiquark. (b) The motion and breakup of a string system, with the two transverse degrees of freedom suppressed (diagonal lines are (anti)quarks, horizontal ones snapshots of the string field) [127].

650 The evolution of string fragmentation is illustrated schematically on the right  
 651 side of Figure 16. This figure is drawn in a light cone presentation, so the initial  
 652 quark and antiquark are going to separate directions at the speed of light. The  
 653 string between them, illustrated in the figure by the red line, stretches until its  
 654 potential energy becomes high enough that it can break, forming a new quark-  
 655 antiquark pair. If the original pair was  $q\bar{q}$  and the new pair  $q'\bar{q}'$ , now two new  
 656 pairs  $q\bar{q}'$  and  $q'\bar{q}$  have formed. As these particles are also moving away from each  
 657 other, the strings between them can stretch and break, creating yet more pairs.  
 658 The process continues until the invariant mass of the system connected by the  
 659 string becomes small enough and a final state meson is formed.

660 To mathematically model the string one can use a massless relativistic string  
 661 with no transverse degrees of freedom. The gluons are represented as energy and  
 662 momentum carrying kinks on the string with incoherent sums of one colour charge  
 663 and one anticolour charge. When this string breaks, it is classically required that  
 664 the created quark and antiquark are produced at a certain distance if they are to  
 665 have any mass or transverse momentum. However, taking into account quantum  
 666 mechanics, the pair must be created at one point and then tunnel out to the  
 667 classically allowed region. Thus the probability to create a new quark-antiquark  
 668 pair becomes proportional to the tunnelling probability [130].

$$P_{\text{tunnelling}} \propto \exp\left(\frac{-\pi m_\perp^2}{\kappa}\right) = \exp\left(\frac{-\pi m^2}{\kappa}\right) \left(\frac{-\pi p_\perp^2}{\kappa}\right), \quad (30)$$

669 where the transverse mass  $m_\perp$  is defined as  $m_\perp^2 = m^2 + p_\perp^2$ . The transverse  
 670 momentum is now defined to be transverse to the string axis. This formula gives  
 671 flavour-independent Gaussian  $p_\perp$ -distribution for the created  $q\bar{q}$  pairs.

672 As explained above the string fragmentation would only produce mesons in  
 673 the final state, but we know that also baryons are created in the process. In the  
 674 string fragmentation model baryon production is included by adding a probability  
 675 that a diquark-antidiquark pair is created instead of a quark-antiquark pair when  
 676 a string breaks.

677 The kinematics of each string breaking are determined iteratively. Since there  
 678 is no natural ordering, the string breaking can be considered in any order and  
 679 the answer obtained must be the same. One can start from the q leg and work  
 680 one's way to the  $\bar{q}$  leg, or vice versa. This give a left-right symmetry of the  
 681 string fragmentation. In the Lund model this is taken into account by defining a  
 682 symmetric fragmentation function

$$f(z) \propto \frac{1}{z} (1-z)^a \exp\left(-\frac{bm_\perp^2}{z}\right) \quad (31)$$

683 to break the string into a hadron and a remainder system. Here  $z$  is the fraction  
 684 of light-cone momentum  $p^+$  given to the hadron in the string breaking,  $m_\perp$  is the  
 685 transverse mass of the hadron and  $a$  and  $b$  are tuneable parameters of the model.  
 686 For heavy quarks this is modified as

$$f(z) \propto \frac{1}{z^{1+bm_Q^2}} (1-z)^a \exp\left(-\frac{bm_\perp^2}{z}\right). \quad (32)$$

687 The process can be thought as follows: first start from the q-leg of a  $q\bar{q}$  system  
 688 and choose to consider the breaking to new  $q'\bar{q}'$  pair closest to this leg. Now the  
 689 breaking will produce a hadron  $q\bar{q}'$  and a remainder system spanning from  $q'\bar{q}$ .  
 690 Then the process is continued until the  $\bar{q}$ -leg is reached. A small detail here is  
 691 that in equation (31) it is assumed that the mass of the remainder system is large.  
 692 Thus some patching up is needed for the last two hadrons coming from a string.  
 693 The patching up is done such that the place where it happens looks as closely like  
 694 any other string break as possible.

695 One additional possibility one must consider is that a string can have such a  
 696 low mass that it cannot break at all. In this case a single hadron is generated out  
 697 of the string and if necessary energy and momentum are exchanged with other  
 698 partons in the event.

699 After all the hadrons are produced, the short-lived ones can still decay before  
 700 the set of final state particles in the simulation is obtained [125]

## 701 Cluster model

702 Instead of a string model HERWIG [126] uses a cluster model for hadronisation.  
 703 The advantage of cluster models is that they require a smaller number of param-  
 704 eters than string models. The model is based on the preconfinement property of

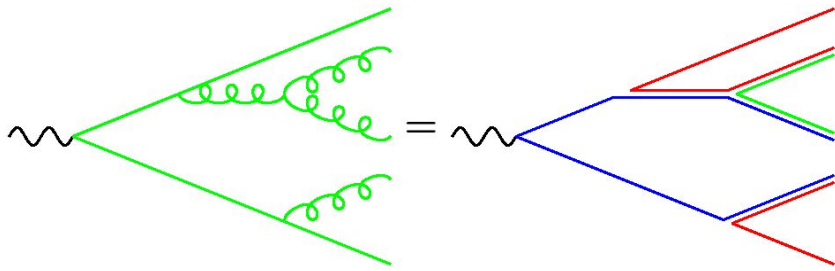


Figure 17: Colour structure of a parton shower to leading order in  $N_c$ . [127]

705 parton showers, i.e. the colour structure of the shower at any evolution scale  $Q_0$  is  
 706 such that colour singlet combinations of partons can be formed with an asymptot-  
 707ically universal invariant mass distribution. The invariant mass does not depend  
 708 on the initial hard process scale  $Q$ , but only on  $Q_0$  and the QCD scale  $\Lambda_{\text{QCD}}$ , when  
 709  $Q \gg Q_0$  [127].

710 The cluster model starts from transforming all gluons non-perturbatively into  
 711  $q\bar{q}$  pairs, which requires that the gluons get a mass, which must be at least twice  
 712 the lightest quark mass. After the gluons are transformed into quarks, the adjacent  
 713 colour lines can be clustered together to colour singlet states with mesonic quantum  
 714 numbers. The momentum of these clusters is defined to be the sum of the momenta  
 715 of the clustering partons. The principle of colour-preconfinement states that the  
 716 mass distribution of these clusters is independent of the hard scattering process  
 717 and its centre-of-mass energy [126].

718 Some of these initial clusters are too heavy to reasonably describe an excited  
 719 state of a hadron. These must be split before they are allowed to decay. The  
 720 cluster  $C$  is split if its mass fulfills the condition [126]

$$M_C^p \geq M_{\max}^p + (m_1 + m_2)^p, \quad (33)$$

721 where  $m_{1,2}$  are the masses of the constituents partons of the cluster.  $M_{\max}$  and  $p$   
 722 are parameters given defined the model. These have to be chosen separately for  
 723 clusters containing light, charmed and bottom quarks. When a cluster splits, a pair  
 724 of light quarks is generated from the vacuum, which form two new clusters, both  
 725 containing one quark from the original cluster and one from the newly generated  
 726 pair. The splitting continues until no clusters with masses fulfilling the equation  
 727 33 remains.

728 When the clusters are light enough, they decay into final state hadrons. If  
 729 the cluster mass is high enough for decaying into a baryon-antibaryon pair, it  
 730 can undergo either a mesonic or a baryonic decay. The probabilities of mesonic  
 731 and baryonic decays are parameters in the model [126] For a mesonic decay a  
 732 quark-antiquark pair is created from the vacuum and for the baryonic decay a

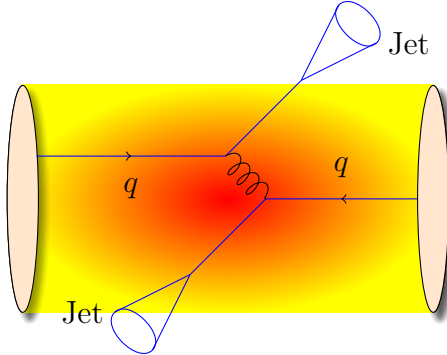


Figure 18: If hard scatterings happen in conjunction with QGP medium the produced jets must traverse the medium. Thus they are subject to interactions with the medium. Note that the dijet pair can be created anywhere within the medium volume and thus the two jets will have differing path lengths through the medium.

diquark-antidiquark pair is made. Then the exact decay products are chosen and the cluster decays isotropically in the rest frame of the cluster. If there are partons produced in the perturbative phase involved in the decay, they retain their original direction in the cluster rest frame, up to some Gaussian smearing. If the cluster mass is too low to decay into a pair of mesons, it decays into the lightest possible hadron and some energy and momentum is exchanged with the adjacent clusters. At the end we are left with the final state hadrons, some of which might still decay until the end of the simulation if they are very short-lived. [126]

#### **1.4.5 Interactions between jet and medium**

Let us now look at what happens to jet production in heavy-ion collisions. Figure 18 shows a dijet produced inside QGP medium. High momentum particles are very rare and they are only produced in the initial collisions. In a heavy ion collision, where a QGP medium is formed, the hard scattered quarks and gluons are expected to interact strongly with the medium due to their colour charges and thus lose energy, either through collisions with medium partons, or through gluon bremsstrahlung [6]. This is referred to as jet quenching. Studying the modification of jets inside the medium gives another key approach to constraining the properties of QGP. Modification can be also observed in jet shapes, particle composition, fragmentation, splitting functions and many others.

752 **Discovery of jet quenching via leading hadron suppression**

753 First evidence of jet quenching comes from observing high  $p_T$  tracks, i.e. the  
754 leading hadrons of jets. In this picture jet quenching in heavy-ion collisions is  
755 usually quantified with the nuclear modification factor  $R_{AA}$ , which is defined as

$$R_{AA}(p_T) = \frac{(1/N_{AA}^{evt}) dN^{AA}/dp_T}{\langle N_{coll} \rangle (1/N_{pp}^{evt}) dN^{pp}/dp_T} \quad (34)$$

756 where  $dN^{AA}/dp_T$  and  $dN^{pp}/dp_T$  are the yields in heavy-ion and proton-proton  
757 collisions, respectively and  $\langle N_{coll} \rangle$  is the average number of binary nucleon-nucleon  
758 collisions in one heavy-ion event. The number of binary collisions can be calculated  
759 from the Glauber model as shown in Section 1.3.1. From the point of view of direct  
760 production at high  $p_T$  a heavy-ion collision can be estimated relatively well to be  
761 only a series of proton-proton collisions. At low  $p_T$  this scaling breaks down as the  
762 determining factor in direct production is the number of participants.

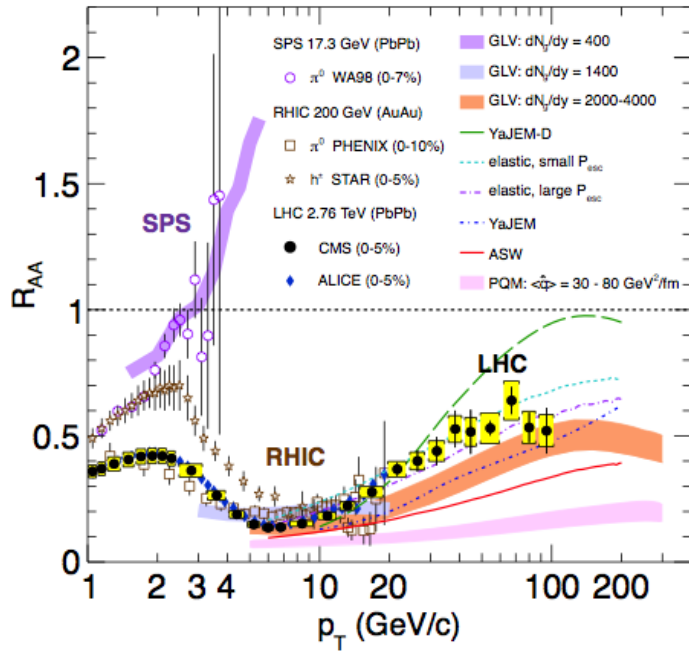


Figure 19: Measurements of the nuclear modification factor  $R_{AA}$  in central heavy-ion collisions at three different center-of-mass energies, as a function of  $p_T$ , for neutral pions ( $\pi^0$ ), charged hadrons ( $h^\pm$ ), and charged particles [131–135], compared to several theoretical predictions [69, 136–140]. The error bars on the points are the statistical uncertainties, and the yellow boxes around the CMS points are the systematic uncertainties. The bands for some of the theoretical calculations represent their uncertainties [141].

If the medium has no effect on high  $p_T$  particles the nuclear modification factor should be 1. As seen in Figure 19  $R_{AA}$  at RHIC and LHC has been observed to be as low as 0.2, which is a clear signal that jet quenching is happening. However, the physical interpretation is not that 80 % of high momentum tracks disappear, rather they are shifted to smaller momenta. The relation between the shift in momentum and  $R_{AA}$  depends on the steepness of the  $dN/dp_T$  spectra. At LHC energies the spectrum is flatter and thus the same  $R_{AA}$  value as in RHIC requires a larger momentum shift, which results from the larger temperature of the medium at LHC.

The reaction plane dependence of inclusive particle  $R_{AA}$  demonstrates that energy loss is path length dependent [142], as expected from models. The path length can be affected by collisions centrality and system size. However, the temperature and lifetime of the QGP also changes with changing centrality and system size. Thus to study different path lengths the angle relative to the reaction plane gives the cleanest signal, as the properties of medium remain the same. Additionally it was concluded that there is no suppression for path lengths below  $L = 2 \text{ fm}$ . Similar indications about path length dependence are given by jet  $v_2$  both at RHIC [143] and at LHC [144, 145].

## QED Bremsstrahlung

Many of the energy loss models exploit the analogy between the QCD interaction of parton propagating through the coloured medium and the QED energy loss of electron propagating through material. An electron propagating through matter loses its energy by photon Bremsstrahlung radiation. In the simplest case, each individual scattering center results in a single emission of a photon. This is known as the Bethe-Heitler regime [146]. The energy spectrum of radiated photons  $dN/dE$  is, in this case, proportional to  $1/E$ . However, the Bremsstrahlung photon, can be radiated only when the distance between the scattering centers is larger than the formation length. In the limit, when the scattering centers are closer than the formation length, the Bremsstrahlung process is suppressed. This phenomenon is known as the Landau-Pomeranchuk-Migdal (LPM) [147, 148] suppression. The radiated spectrum in this regime is proportional to  $1/\sqrt{E}$ .

Lower energy photons are further suppressed by the destructive interference leading to the suppression of Bremsstrahlung photons of  $E < \gamma\omega_p$ , where  $\omega_p$  is the plasma frequency of the radiator. This is known as Dielectric suppression. The photon energy distribution in this regime is proportional to the energy of the photon. A schematic view of the effect of these three regimes is shown in Figure 20.

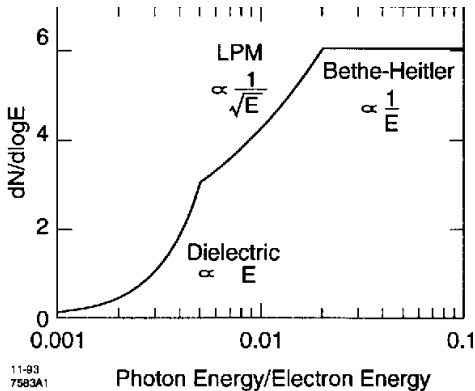


Figure 20: The expected bremsstrahlung spectrum for an electron propagating through material. [149].

## 799 QCD

800 In QCD the radiative energy loss mechanism is given in terms of the transport co-  
 801 efficient  $\langle \hat{q} \rangle$ , which describes the average momentum transfer between the medium  
 802 and parton [150]. The exact definition of this depends on the theoretical formalism  
 803 used to describe the energy loss mechanism.

804 The simplest energy loss process is elastic QCD scattering off the medium par-  
 805 tons. In elastic scatterings the recoil energy of the scattered partons are absorbed  
 806 by the thermal medium, which reduces the energy of the initial parton. The mean  
 807 energy loss from elastic scatterings can be estimated by

$$\langle \Delta E \rangle_{\text{el}} = \sigma \rho L \langle E \rangle_{\text{1scatt}} \propto L, \quad (35)$$

808 where  $\sigma$  is the interaction cross section and  $\langle E \rangle_{\text{1scatt}}$  is the mean energy transfer  
 809 of one individual scattering [151]. This assumption holds if the mean energy is  
 810 independent of the total energy of the parton ( $E$ ). The transport coefficient of  
 811 elastic scattering,  $\langle \hat{q}_{\text{el}} \rangle = \langle \Delta E \rangle / L$ , is defined as the mean energy loss per unit path  
 812 length.

813 Another energy loss mechanism is medium-induced radiation. In QCD this  
 814 radiation is mainly due to the elementary splitting processes,  $q \rightarrow qg_r$  and  $g \rightarrow gg_r$ .  
 815 Assuming that the parton is moving with the speed of light radiation energy loss  
 816 can be estimated by

$$\langle \Delta E \rangle_{\text{rad}} \propto T^3 L^2, \quad (36)$$

817 where  $L$  is the length of the medium and  $T$  is its temperature [152]. The differ-  
 818 ent exponents of  $L$  in equations 35 and 36 indicate that radiative energy loss is  
 819 dominant over elastic energy loss.

820 There are several models that attempt to describe the nature of the energy loss  
821 mechanism. The most used models can be divided into four formalisms.

822 In the Gyulassy-Levai-Vitev (GLV) [153] opacity expansion model the radiative  
823 energy loss is considered on a few scattering centers  $N_{scatt}$ . The radiated gluon  
824 is constructed by pQCD calculation as summing up the relevant scattering amplitudes  
825 in terms of the number of scatterings. Another approach into opacity expansion is the ASW  
826 model by Armesto, Salgado and Wiedermann [154].

827 Thermal effective theory formulation by Arnold, Moore and Yaffe (AMY) [155]  
828 uses dynamical scattering centers. It is based on leading order pQCD hard thermal  
829 loop effective field theory. This model assumes that because of the high temperature  
830 of the plasma the strong coupling constant can be treated as small. The parton propagating  
831 through the medium will lose energy from soft scatterings and hard scatterings.

833 The above models calculate the energy loss while the parton propagates through  
834 the medium, focusing on the pQCD part. The higher twist (HT) approach by Wang  
835 and Guo [156] implements the energy loss mechanism in the energy scale evolution  
836 of the fragmentation functions.

837 The last category is formed by the Monte Carlo methods. The PYTHIA event  
838 generator [157] is widely used in high-energy particle physics. Two Monte Carlo  
839 models based on PYTHIA describing the energy loss mechanism are PYQUEN [158]  
840 and Q-Pythia [159]. Other Monte Carlo models include JEWEL [160] and Ya-  
841 JEM [161].

#### 842 1.4.6 New paradigm of jet Quenching

843 As described in the previous sections the first indications of jet quenching, such  
844 as  $R_{AA}$ , looked essentially at the leading hadrons of jets, the hard part, ignoring  
845 the soft scale part of jet phenomena. However, experimental methods have since  
846 improved; jet reconstruction algorithms have become reliable in the LHC era.  
847 Instead of the leading hadron we can study the entire jet shower and its structure.  
848 In jet observables one must consider what happens to the lost energy. Radiated  
849 gluons may end up being clustered with the jet, depending on the radiation angle,  
850 the parameters of jet reconstruction and whether the gluon reaches equilibrium  
851 with the medium or not. Thus the suppression on the jet level is expected to  
852 be smaller. Figure 21 shows jet  $R_{AA}$  in central Pb–Pb collisions measured by  
853 ALICE,ATLAS and CMS and indeed jet  $R_{AA}$  is about 0.5 instead of 0.2.

854 Thus, on the level of the reconstructed jet, energy loss manifests itself as broadening  
855 and softening of the jet. This is seen for example in jet-hadron correlations.  
856 Figure 22 shows  $\Delta\eta$  correlations with the leading jet.  $\Delta\phi$  correlations have similar  
857 trends. Jets in Pb–Pb are observed to be broader, with the greatest increase in  
858 the width for low momentum associated particles. This is consistent with expec-

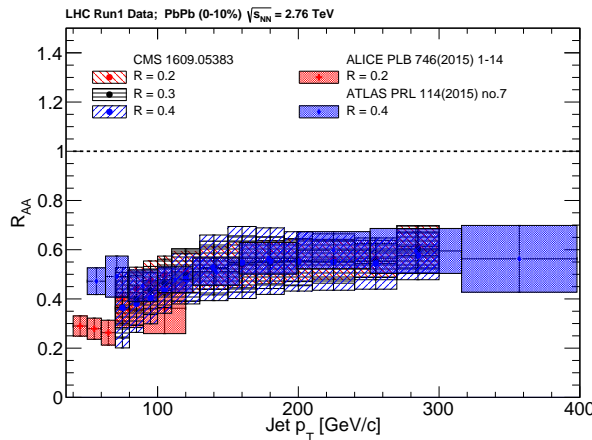


Figure 21: Reconstructed anti- $k_T$  jet  $R_{AA}$  from ALICE [162] with  $R = 0.2$  for  $|\eta| < 0.5$ , ATLAS [163] with  $R = 0.4$  for  $|\eta| < 2.1$ , and CMS [164] with  $R = 0.2, 0.3$  and  $0.4$  for  $|\eta| < 2.0$ . The ALICE and CMS data are consistent within uncertainties while the ATLAS data are higher. The experiments use slightly different methods in selecting jets and subtracting the underlying event contribution. Compared to ALICE and CMS the ATLAS technique could impose a survivor bias and lead to a higher jet RAA at low momenta. Figure from [6]

tations from partonic energy loss. These studies found that the subleading jet was broadened even more than the leading jet, indicating a bias towards selecting less modified jets as the leading jet. Jet hadron correlations have also been studied at RHIC with similar conclusion [165].

### 863 Phase-space view of the medium modified parton cascade

The new paradigm in jet quenching in heavy-ion collisions involves multi-scale problems [167, 168]. The elementary scattering and the subsequent branching process down to non-perturbative scales are dominated by hard scales in the vacuum as well as in the medium. Soft scales, of the order of the temperature of the medium, characterise the interactions of soft partons produced in the shower with the QGP. Soft scales also rule hadronisation, which is expected to take place in vacuum for sufficiently energetic probes, even though some modifications can persist from modifications of colour flow [169–171]. Understanding the contributions from the different processes to the jet shower evolution in medium and their scale dependence is crucial to constrain the dynamics of jet energy loss in the expanding medium, the role of colour coherence [172], and fundamental medium properties like temperature dependent transport coefficient [173, 174].

Let us now look at medium modification of jets in a  $\log(p) - \log(\theta)$  plane

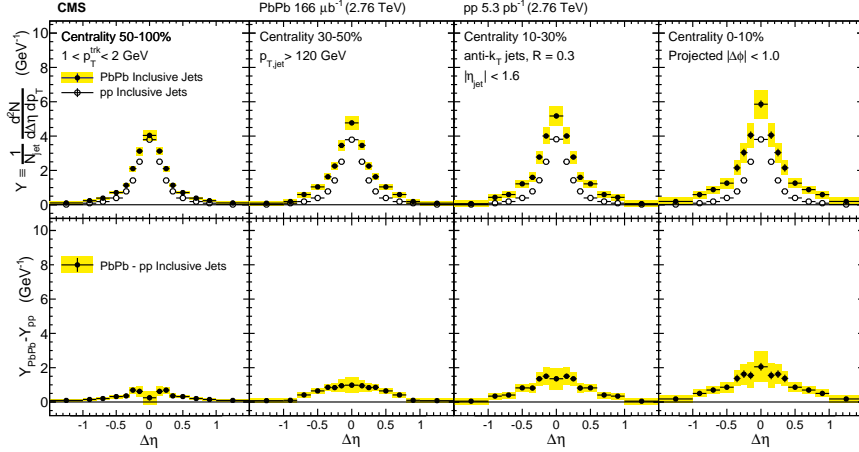


Figure 22: Measurement by CMS [166]. Symmetrized  $\Delta\eta$  distributions correlated with Pb–Pb and pp inclusive jets with  $p_T > 120$  GeV are shown in the top panels for tracks with  $1 < p_T < 2$  GeV. The difference between per-jet yields in Pb–Pb and pp collisions is shown in the bottom panels. These measurements indicate that the jet is broadened and softened, as expected. The effect is stronger in more central collisions.  $\Delta\phi$  correlations have similar trends.

as shown in [167]. The different momentum and angular scales are subject to different physical phenomena. Figure 23 shows the relevant medium modification phenomena for different regions of the phase space at time  $t$ , when a jet propagates through a thermal cloud of temperature  $T$ . As in practice jets propagate over a finite path-length  $L$  in QCD matter, Figure 23 can be taken as a representation of the distribution of partonic jet fragments at moment  $t \approx L$ , when the jet escapes the medium. [167]

The region marked as DGLAP is dominated by the primary vacuum splittings explained in section 1.4.2. This region is determined by  $\theta > \theta_{\text{vac}}$  with

$$\theta_{\text{vac}} \propto 1/\sqrt{p_T}. \quad (37)$$

Medium-induced parton branching fills the  $\log p$ - $\log \theta$ -plane from the bottom up (in  $p$ ) and from the inside out (in  $\theta$ ). This is because transverse momentum is acquired by Brownian motion in the medium,  $k_\perp^2 \propto \hat{q}t$ . The formation time constraint  $t \geq p/k_\perp^2 \approx p/\hat{q}t$  implies that medium-induced quanta can be formed in the region  $p \leq k_{\text{form}}$  where

$$k_{\text{form}}(t) = \hat{q}t^2. \quad (38)$$

For these splittees to survive without further splittings they must have

$$p \geq k_{\text{split}} \approx \alpha_s^2 k_{\text{form}}(t) \approx \alpha_s^2 \hat{q}t^2. \quad (39)$$

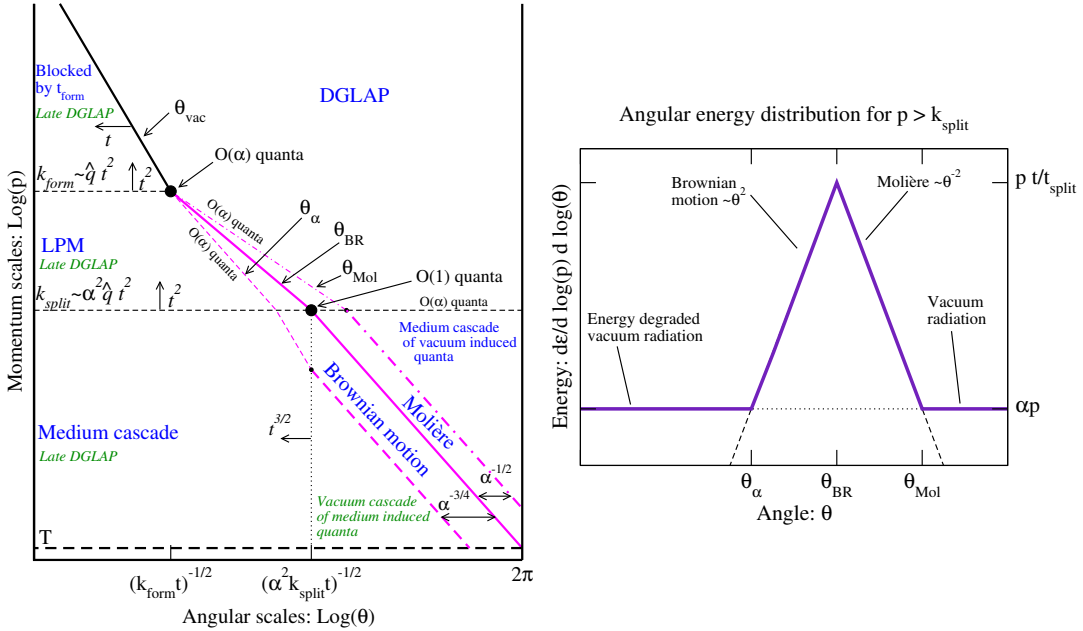


Figure 23: *Left:* Phase space view of dominant contributions in a medium-modified parton cascade. *Right* The distribution of energy as a function of angle for a fixed momentum with  $p > k_{\text{split}}$ . Large angular scales  $\theta > \theta_{\text{Mol}}$  are dominated by DGLAP vacuum radiation from the leading parton at the scale  $Q$ . At  $\theta < \theta_\alpha$  the energy density is dominated by vacuum radiation of the leading parton after it has degraded its energy propagating through the medium. Areas  $\theta_\alpha < \theta < \theta_{\text{BR}}$  and  $\theta_{\text{BR}} < \theta < \theta_{\text{Mol}}$  are dominated by Brownian motion and rare large angle (Molière) scatterings with medium partons [167].

892 Thus the region marked as LPM in Figure 23 is filled by the primary medium-  
 893 induced branchings. Fragments with  $p \leq k_{\text{split}}$  will have time to split further.  
 894 An approximately equal splitting where both splittees get momentum  $p/2$  from  
 895 the parent will degrade energy the most. These splittees will undergo the next  
 896 splitting in an even shorter time scale producing even softer fragments. Momenta  
 897 can continue cascading all the way to the thermal scale  $T$  of the medium within the  
 898 same time scale within which the first splitting occurred. Thus filling the region  
 899 marked as Medium cascade in Figure 23. Similarly splittees from vacuum radiation  
 900 can cascade inside the medium when they have  $p \leq k_{\text{split}}$ , filling the bottom right  
 901 corner of the  $\log p$ - $\log \theta$ -plane.

902 The angular distribution of the medium-induced radiation is driven by two  
 903 mechanisms; Multiple soft scatterings give rise to transverse Brownian motion,  
 904 which determines the distribution at small angles. The typical angle reached in  
 905 the LPM region is

$$\theta_{\text{BR}}(p) \approx \frac{\sqrt{\hat{q}t}}{p}, \text{ for } k_{\text{form}} > p > k_{\text{split}}, \quad (40)$$

906 while in the medium cascade region of the phase space this becomes

$$\theta_{\text{BR}}(p) \approx \left(\frac{T}{p}\right)^{\frac{3}{4}} \quad (41)$$

907 Large angular scales cannot be reached by Brownian motion, but can arise from  
908 rare large angle scatterings with partons in the medium, described first by Molière [175].  
909 The result is that medium-induced radiation is predominantly located in the  
910 bands marked as Brownian motion, where  $\theta_\alpha < \theta < \theta_{\text{BR}}$ , and Molière, where  
911  $\theta_{\text{BR}} < \theta < \theta_{\text{Mol}}$  in Figure 23.

912 The hard parton will naturally continue radiating after it leaves the medium.  
913 As there is no longer kinematic limits set by the time scale, the vacuum radiation  
914 can extend to smaller angular scales in the phase space. The results is that the  
915 regions, where  $\theta < \theta_\alpha$ , marked as Late DGLAP in Figure 23 will be dominated by  
916 the late time vacuum radiation. Naturally also the splittees from medium-induced  
917 radiation will undergo the late stage vacuum radiation phase, filling the triangular  
918 region with small  $p$  and  $\theta < \theta_\alpha$ .

### 919 Influence of jet on medium

920 Energy loss of hard partons is well established by experimental observations. Nat-  
921 urally energy can't just disappear, but is transferred to daughter partons or the  
922 medium. For radiation that stays inside the jet cone energy loss manifests itself  
923 as softening and broadening. If a daughter parton loses energy and becomes equi-  
924 librated with the medium it may no longer be correlated with the parent parton.  
925 This energy would then be distributed at distances far from the jet cone. There is  
926 some evidence for out-of-cone radiation by CMS [176], but the interpretation is not  
927 clear. Other possible phenomena include the mach cone and Molière scattering,  
928 but there is no experimental evidence for these. Evidence for all of these effects  
929 is difficult to find as the underlying event gives already a large and fluctuating  
930 background. Additionally its unclear how this energy would be different from the  
931 underlying event [6].

## 932 1.5 QGP in Small systems

933 After the existence of QGP in heavy-ion collisions has been established, attention  
934 has been turned to small systems. Proton-proton ( $pp$ ) and proton-Lead ( $p\text{-Pb}$ )  
935 collisions have been studied at LHC and RHIC has studied a host of different  
936 collision systems; namely proton-gold ( $p\text{Au}$ ) [177], deuteron-gold ( $d\text{Au}$ ) [178–181]  
937 and helium<sup>3</sup>-gold ( $\text{He}^3\text{Au}$ ) [182] collisions starting from 2000.

938 Already before the era of modern colliders, collective behaviour in proton-  
939 proton collisions was considered by names like Heisenberg, Fermi and Bjorken [7].  
940 Eventually there were some experimental searches of QGP in  $pp$  and  $p\bar{p}$  collisions  
941 in E735 at Tevatron [183] and MiniMAX [184]. However no conclusive evidence  
942 was found.

943 In the early years of RHIC these small systems were mostly considered as control  
944 measurement, for example in constraining nuclear modified parton distribution  
945 functions (nPDFs) that determine the initial gluon distributions that determine  
946 the first epoch of heavy-ion collisions [185, 186].

947 In 2010 ultrahigh-multiplicity  $pp$  collisions were studied at CMS [187]. The  
948 study found that particles had a weak but clear preference to be emitted along a  
949 common transverse  $\phi$  angle across all rapidities [188]. This seemed like behaviour  
950 were similar to AA collisions, but it was argued that it could as well come from  
951 momentum correlations present in the earliest moments of the collision.

952 In 2012 LHC ran its first  $p\text{-Pb}$  data taking period. Around the same time  
953  $d\text{Au}$  data was re-examined at RHIC. Now it was revealed that most of the flow  
954 signatures attributed to hydrodynamic expansion in AA collisions also existed in  
955 smaller systems.

### 956 1.5.1 Collective phenomena

957 The most rugged analysis of collective behaviour concerns the two (or more) particle  
958 correlations, often parametrised via the relative azimuthal angle and pseudo-  
959 rapidity differences,  $\Delta\phi$  and  $\Delta\eta$  respectively. Figure 24 shows two-particle cor-  
960 relations measurements in  $\text{Pb-Pb}$ ,  $p\text{-Pb}$  and  $pp$  collisions at the LHC [189]. In  
961  $\text{Pb-Pb}$  collisions long-range correlations dominate over short-range phenomena.  
962 This shows in the two ridges at  $\Delta\phi = 0$  and  $\Delta\phi = \pi$ . At  $\Delta\phi \approx \Delta\eta \approx 0$ , there is a  
963 peak coming from single jet fragmentation. Since the away-side jet can be spread  
964 out in  $\Delta\eta$ , this contribution disappears when compared to the flow contribution  
965 at the away side ridge. In  $p\text{Pb}$ , and  $pp$  the near side peak is more distinguished  
966 and the away-side jet contribution starts to show. Still, one can see long-range  
967 correlations that seem like flow-like collective behaviour in both systems.

968 In addition to the two particle correlations, correlations have been observed in  
969 the form of  $v_n$  coefficients both at LHC [190] and at RHIC [177]. The results have

also been described with hydrodynamical models, although the applicability of said models might be questionable, because of the large Reynolds numbers in small systems [191, 192]. Figure 25 shows results for  $v_2$  in different collisions systems at RHIC as measured by PHENIX and Figure 26 shows the eccentricities and the resulting hydrodynamic evolution in the systems. These different systems provide also different initial geometries. dAu collisions naturally have an ellipsoidal form, while a He<sup>3</sup> collision has a triangular form and thus produces larger triangular flow,  $v_3$  components.

Other observations that produce flow-like results include mass ordered  $v_2$  coefficients [194] and higher order harmonics coming from fluctuations in the initial geometry [190]. Thus all the major collective flow phenomena observed in heavy-ion collisions have been also identified in small systems.

One open question is identifying the point the point, where flow-like correlations end. The question has proved challenging since low multiplicity events are dominated by non-flow phenomena. This makes observations in low multiplicity events model/method dependant. Different methods assess non-flow contributions differently. Thus some methods fail to observe a signal in cases, where others do and it is unclear whether this is true collective motion or it comes from non-flow contributions.

### 1.5.2 Absence of jet quenching

In A+A collisions, an important confirmation of the standard model comes from the energy loss of high  $p_T$  partons traversing the medium, as discussed in Section 1.4.5. Originally the interest in small systems was due to ruling out possible cold nuclear matter effects that might affect the results also in Pb-Pb. In 2003 the jet quenching effect was observed to disappear in d+Au collisions at RHIC [178–181]. This was taken as an indication that no QGP was created. Similarly at LHC no jet modification has been observed in pPb collisions. Figure 27

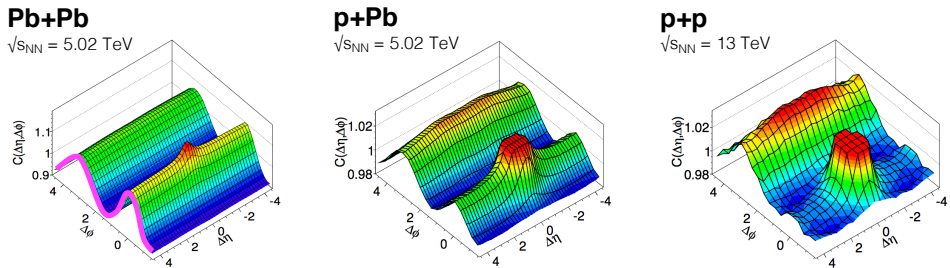


Figure 24: Two-particle correlation results in PbPb, pPb, and pp collisions at the LHC [189].

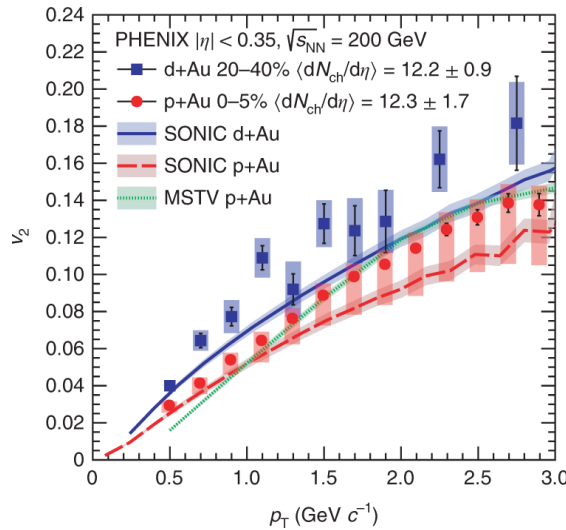


Figure 25: Comparison between hydrodynamic calculations and data from  $p + \text{Au}$ ,  $d + \text{Au}$  and  ${}^3\text{He} + \text{Au}$  collisions [193]

997 shows the nuclear modification factor  $R_{pA}$  and  $v_2$  in pPb collisions as measured at  
998 the LHC [195, 196].

999 Now the lack of jet modification seems surprising considering the multitude of  
1000 flow observations supporting the existence of QGP in small systems. One possible

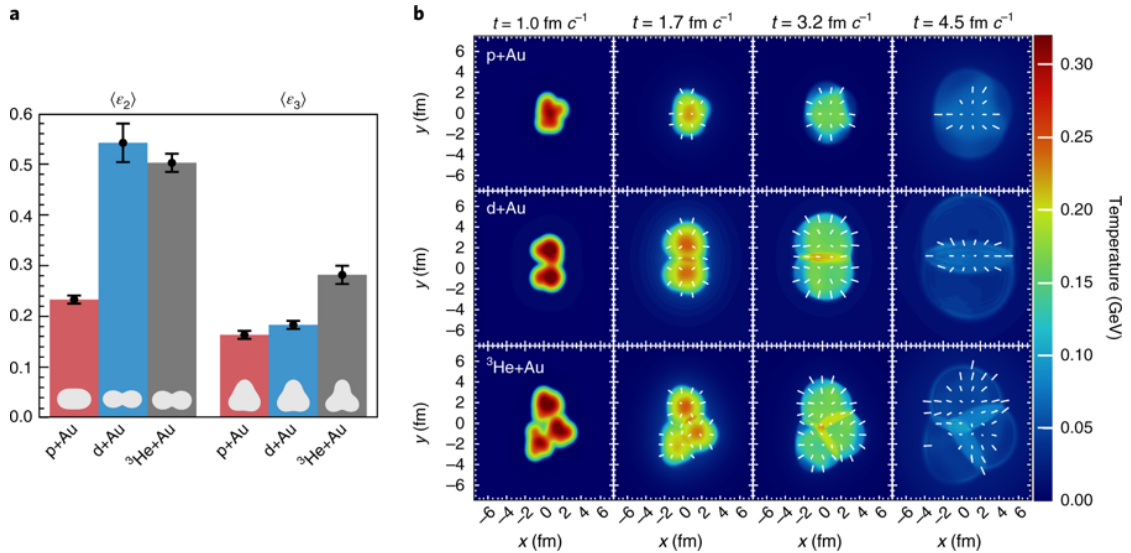


Figure 26: *left* Eccentricities in different systems. *right* Calculations of the initial energy density in small collision systems at RHIC and the resulting hydrodynamic evolution [193].

explanation is simply the size of medium. In PbPb collision partons traversing through the medium lose energy to the medium. If the medium is very small there is limited time for interaction with the medium. Reaction plane dependent  $R_{AA}$  measurements [142] in Pb–Pb collisions indicated that 2 fm could be the minimum path length required for energy loss.

Some calculations [197–199] indicate that there should be modification in the most central p–Pb collisions, but selecting these in the analysis is complicated [7]. In Pb–Pb collisions most of the particle production comes from the medium and thus the total multiplicity is a good indicator of centrality. However in p–Pb collisions the total multiplicity is smaller and is more strongly influenced by jet phenomena. Events with jets have naturally larger multiplicities and are more likely to be classified as central events.

So far the only observable indicative of jet quenching in pPb collisions is the high  $p_T v_2$ . In heavy-ion collisions this is not explained by hydrodynamics. Instead it is assumed to come from jet quenching with different path lengths through the medium in different directions. In Figure 27 ATLAS [196] and CMS [200] measurements of  $v_2$  in pPb and PbPb collisions are shown. The pPb results seem to follow a very similar pattern. However, the non-flow effects in this high- $p_T$  region are not fully under control, so the physical interpretation is still under debate.

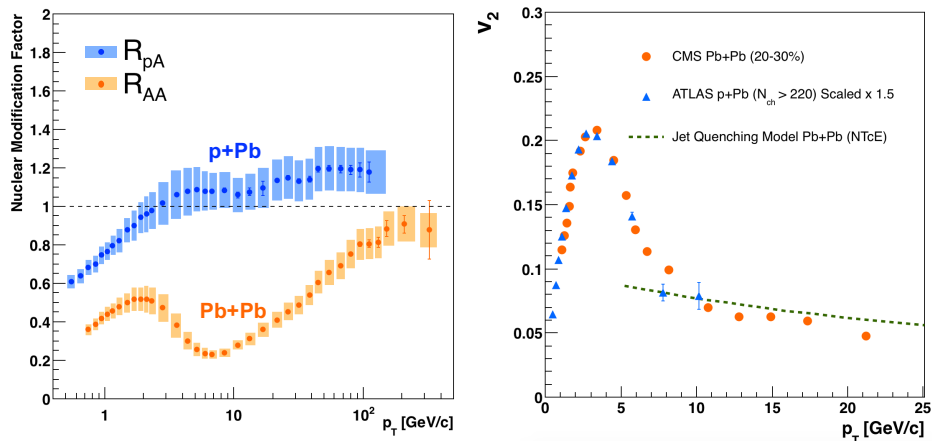


Figure 27: The nuclear modification factor  $R_{pA}$  in p–Pb collisions [195]. Compared to  $R_{AA}$   $R_{pA}$  shows no sign of modification. *right* The  $v_2$  coefficient as a function of  $p_T$  in Pb–Pb and p–Pb at the LHC [196, 200]. For shape comparison the p–Pb results have been scaled up by a factor 1.5. The green dotted curve [197] is from a jet quenching calculation where the anisotropy results from the directional dependence of the energy loss, rather than hydrodynamic flow.

### 1020 1.5.3 Centrality determination in small systems

1021 In lead-lead collisions the total multiplicity of the event is a good indicator of the  
 1022 geometric centrality of the collision [86]. In proton-lead collisions the connection  
 1023 between multiplicity and centrality is less clear [201]. In p-Pb collisions the im-  
 1024 pact parameter is only loosely correlated to  $N_{\text{part}}$  or  $N_{\text{coll}}$ . Hence, although one  
 1025 uses traditionally the term centrality to refer to these measurements, the relevant  
 1026 parameters are  $N_{\text{part}}$  and  $N_{\text{coll}}$  [201].

1027 As in Pb-Pb collisions the Glauber model [82] is generally used to calculate  
 1028 geometrical quantities of p-Pb collisions. In this model, the impact parameter  $b$   
 1029 controls the average number of participating nucleons  $N_{\text{part}}$  and the corresponding  
 1030 number of collisions  $N_{\text{coll}}$ . It is expected that variations of the amount of matter  
 1031 overlapping in the collision region will change the number of produced particles,  
 1032 and parameters such as  $N_{\text{part}}$  and  $N_{\text{coll}}$  have traditionally been used to describe  
 1033 those changes quantitatively, and to relate them to pp collisions. Figure 28 shows  
 1034 the measured V0A amplitude distribution in ALICE and the best NBD-Glauber  
 1035 fit to the distribution [201].

1036 The problem in p-Pb collisions is that fluctuations in multiplicity coming from  
 1037 for example hard scatterings are of the same order as the differences in multiplicity  
 1038 between centrality classes. In Pb-Pb collisions these multiplicity fluctuations  
 1039 have little influence on the centrality determination as the range of  $N_{\text{part}}$  or  $N_{\text{coll}}$  is  
 1040 large and both  $P(M|N_{\text{part}})$  and  $P(M|N_{\text{coll}})$  converge quickly to a Gaussian with

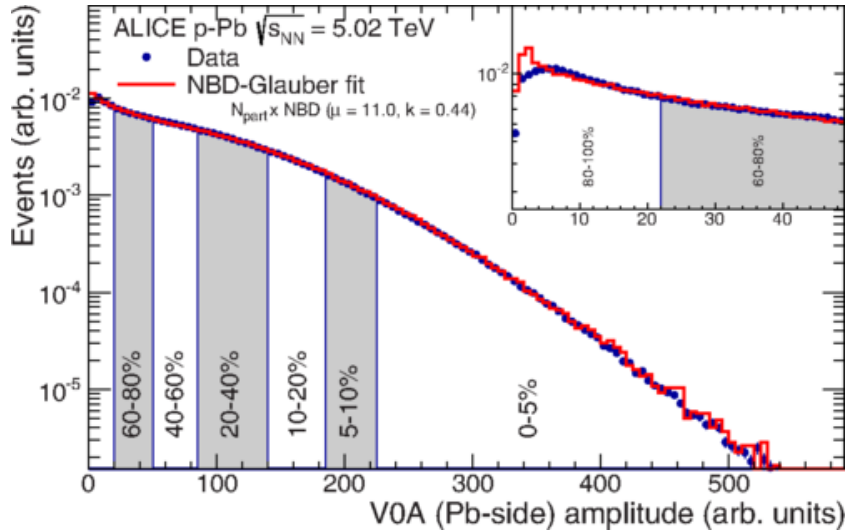


Figure 28: Distribution of the sum of amplitudes in the V0A hodoscopes (Pb-going), as well as the NBD-Glauber fit. Centrality classes are indicated by vertical lines. The inset shows a zoom-in on the most peripheral events. [201]

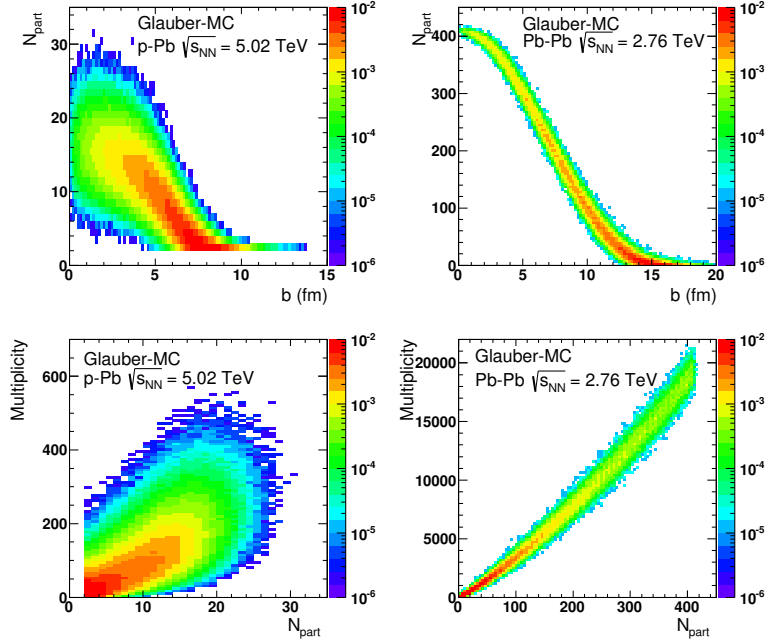


Figure 29: Top: Scatter plot of number of participating nucleons versus impact parameter; Bottom: Scatter plot of multiplicity versus the number of participating nucleons from the Glauber fit for V0A. The quantities are calculated with a Glauber Monte Carlo of p-Pb (left) and Pb-Pb (right) collisions. [201]

a small width relative to the range of  $N_{\text{part}}/N_{\text{coll}}$ . This is illustrated in Figure 29.  
 In practice selecting high multiplicity in p-Pb one chooses not only large average  
 $N_{\text{part}}$ , but also positive multiplicity fluctuations leading to deviations from the  
 binary scaling of hard processes. These fluctuations are partly related to qualitatively  
 different types of collisions. High multiplicity nucleon-nucleon collisions  
 show a significantly higher mean transverse momentum. They can be understood  
 either as harder collisions with larger momentum transfer  $Q^2$  or as nucleon-nucleon  
 collisions where multiple parton-parton interactions (MPI) take place.

Of particular interest are estimators from kinematic regions that are causally disconnected after the collision. The measurement of a finite correlation between them unambiguously establishes their connection to the common collision geometry. Typically these studies are performed with observables from well separated pseudorapidity ( $\eta$ ) intervals, e.g. at zero-degree (spectators, slow-nucleons, deuteron break-up probability) and multiplicity in the rapidity plateau.

One centrality selection that is argued not to induce a bias on the binary scaling of hard processes is provided by the energy measurement with the Zero Degree Calorimeters (ZDC) in ALICE, due to their large  $\eta$ -separation from the central

1058 barrel detectors. They detect the "slow" nucleons produced in the interaction by  
1059 nuclear de-excitation processes or knocked out by wounded nucleons [202].

1060 Additional kinematic biases exist for events containing high- $p_T$  particles, which  
1061 arise from the fragmentation of partons produced in parton-parton scattering with  
1062 large momentum transfer. Their contribution to the overall multiplicity increases  
1063 with increasing parton energy and thus can introduce a trivial correlation between  
1064 the centrality estimator and the presence of a high- $p_T$  particle in the event. For  
1065 very peripheral collisions, the multiplicity range that governs the centrality for the  
1066 bulk of soft collisions can represent an effective veto on hard processes. For the  
1067 nuclear modification factor this would lead to  $R_{\text{pPb}} < 1$  [201].

## 1068 2 Experimental Setup

### 1069 2.1 CERN

1070 The European Organization for Nuclear Research (CERN), established in 1954, op-  
1071 erates the largest particle physics laboratory in the world. In 2019 CERN consists  
1072 of 22 member states. Additionally CERN has contacts with a number of associate  
1073 member states and various individual institutions. The laboratory, also referred  
1074 to as CERN, itself is located near Geneva at the border of France and Switzerland  
1075 employs about 2500 people. Additionally some 12000 visiting scientists from over  
1076 600 institutions in over 70 countries come to CERN for their research. [203]

1077 The laboratory includes a series of accelerators, which are used to accelerate  
1078 the particle beams used. A schematic view of the complex as of 2019 is shown  
1079 in Figure 30. In the framework of this thesis the most important component is  
1080 the Large Hadron Collider (LHC), the largest collider in the world. LHC will be  
1081 discussed in more detail in Section 2.2. Other accelerators in the series are used  
1082 to inject the particle beams into LHC, but they are also used in itself for various  
1083 experimental studies.

1084 The second largest accelerator is the super proton synchrotron (SPS). It is the  
1085 final step before the particle beam is injected into LHC. Commissioned in 1976, it  
1086 was the largest accelerator at CERN until the the Large Electron-Positron Collider  
1087 (LEP) was finished in 1989. Originally it was used as a proton-antiproton collider  
1088 and as such provided the data for the UA1 and UA2 experiments, which resulted in  
1089 the discovery of the W and Z bosons [205]. At the moment there are several fixed  
1090 target experiments utilising the beam from the SPS. These study the structure  
1091 (COMPASS citeCOMPASS) and properties (NA61/SHINE [206]) of hadrons, rare  
1092 decays of kaons (NA62 [207]) and radiation processes in strong electromagnetic  
1093 fields (NA63 [208]). Additionally the AWAKE [209] and UA9 [210] experiments  
1094 are used for accelerator research and development.

1095 The third largest accelerator in CERN is the proton synchrotron (PS). Ca-  
1096 pable of accelerating beams up to an energy of 25 GeV PS provides the beam to  
1097 SPS. Additionally PS has experiments for studying strong force (DIRAC [211]),  
1098 the effect of cosmic rays on cloud formation (CLOUD [212]) and neutron-nucleus  
1099 interactions (nTOF [213]).

1100 Additionally PS provides the beam to the antiproton decelerator (AD), which  
1101 uses the beam and a block of metal to produce antiprotons. These are then  
1102 decelerated in AD into a useful low-energy beam, which is provided to a host of  
1103 experiments studying the properties of antimatter.

1104 PS gets proton beams from LINAC2 through BOOSTER and ion beams from  
1105 LINAC3 through LEIR. From BOOSTER beams are also provided to the On-Line  
1106 Isotope Mass Separator (ISOLDE). ISOLDE directs the beam into thick targets

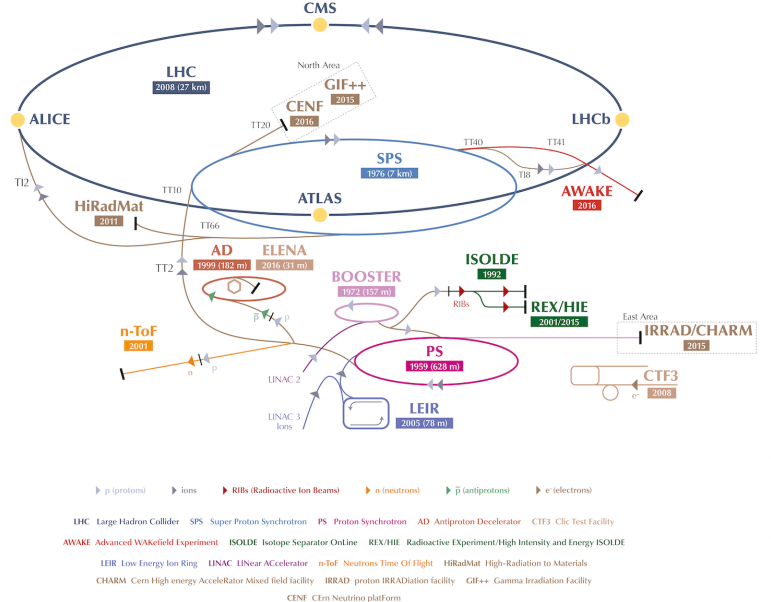


Figure 30: A schematic view of the accelerator complex at CERN. Before particles can be injected into the LHC they require a series of accelerators with increasing size. Until 2018 protons started their journey in LINAC2 (Linear Accelerator) and continue through the Booster, Proton Synchrotron (PS) and Super Proton Synchrotron (SPS). Between 2019 and 2020 LINAC2 will be replaced by LINAC4 [204]

to produce low energy beams of radioactive nuclei. These beams are used to study the properties of even the most exotic of atomic nuclei in a host of experiments.

More information of the various experiments at CERN can be found online in [214].

## 2.2 Large Hadron Collider

The Large Hadron Collider (LHC) [215, 216] with its circumference of 26.7 km is the largest accelerator at CERN and the largest particle collider ever built. The LHC is designed to accelerate protons up to an energy of 8 TeV and lead ions up to center of mass energies of 5.02 TeV per nucleon. The design luminosity of the LHC is  $10^{34} \text{ cm}^{-2}\text{s}^{-1}$ . In 2017 it achieved a record peak luminosity of  $2 \cdot 10^{34} \text{ cm}^{-2}\text{s}^{-1}$  which was also reached in 2018. For lead beams luminosities of up to  $6 \cdot 10^{27} \text{ cm}^{-2}\text{s}^{-1}$  were reached in 2018. All this is achieved with a ring consisting of 1232 superconducting dipole magnets that keep particles in orbit.

1120 The LHC receives beams with energies of 450 GeV from the SPS. In the LHC  
1121 the particles are accelerated through the use of radio-frequency (RF) cavities.  
1122 Electromagnetic waves become resonant and build up inside the cavity. As they  
1123 consist of electromagnetic waves, the field in the RF cavity oscillates. Charges  
1124 passing through the cavity feel the overall force and are pushed forward along the  
1125 accelerator. Particles must enter the cavity at the correct phase of oscillation to  
1126 receive a forward push. When timed correctly, the particles will feel zero acceler-  
1127 erating voltage when they have exactly the correct energy. Particles with higher  
1128 energies will be decelerated and particles with lower energies will be accelerated.  
1129 This focuses particles in distinct bunches. The RF oscillation frequency at the  
1130 LHC is 400.8 MHz. Thus RF "buckets" are separated by 2.5 ns. However only 10  
1131 % are actually filled with particles, so the bunch spacing in the LHC is 25 ns, at  
1132 a bunch frequency of 40 MHz. [215]

1133 With 7 TeV proton beams the dipole magnets used to bend the beam must  
1134 produce a magnetic field of 8.33 T. This can be only achieved through making  
1135 the magnets superconducting, which requires cooling them down with helium to a  
1136 temperature of 1.9 K. The 1232 dipole magnets make up roughly 2/3 of the LHC  
1137 circumference. The remaining part is made up of the RF cavities, various sensors  
1138 and higher multipole magnets used to keep the beam focused. The most notable  
1139 of these are the 392 quadrupole magnets. [215]

1140 The LHC is divided into octants, where each octant has a distinct function.  
1141 Octants 2 and 8 are used to inject beam into the LHC from SPS. The 2 beams  
1142 are crossed in octants 1,2,5 and 8. The main experiments are built around these  
1143 crossing points. Octants 3 and 7 are used for beam cleansing. This is achieved  
1144 through collimators that scatter particles with too high momentum or position  
1145 offsets off from the beam. The RF cavities used for acceleration are located in  
1146 octant 4 and octant 6 is used for dumping the beam. The beam dump is made  
1147 up of two iron septum magnets, one for each beam, that will kick the beam away  
1148 from machine components into an absorber when needed.

### 1149 2.2.1 LHC experiments

1150 As of 2018 there are four main experiments at the LHC; ALICE [217], ATLAS [218],  
1151 CMS [219] and LHCb [220] and three smaller ones LHCf [221], TOTEM [222] and  
1152 MoEDAL [223]. ALICE will be covered in detail in Section 2.3.

1153 ATLAS (A Toroidal LHC ApparatuS) [218] and CMS (Compact Muon Solenoid) [219]  
1154 are the two largest experiments at the LHC. They are both multipurpose exper-  
1155 iments designed to be sensitive to many different possible new physics signals,  
1156 such as extra dimensions and dark matter particles. The biggest discovery made  
1157 by these so far is the discovery of the Standard Model Higgs boson, which was  
1158 simultaneously published by the experiments in 2012 [224, 225].

1159 The LHCb (LHC beauty) experiment [220] is made for studying the bottom  
1160 (beauty) quark. Main physics goals of the LHCb include the measurement of the  
1161 parameters of CP violation with decays of hadrons containing the bottom quark.  
1162 One of the most important results published by LHCb is the first measurement of  
1163  $B_s^0 \rightarrow \mu^+ \mu^-$  decay, which was found to be in line with the Standard Model.

1164 In addition to the four large experiments there are three smaller experiments  
1165 along the LHC ring. LHCf (LHC forward) [221] is located at interaction point 1  
1166 with ATLAS. It aims to simulate cosmic rays by the particles thrown forwards by  
1167 the collisions in ATLAS.

1168 TOTEM (TOTal Elastic and diffractive cross section Measurement) is located  
1169 near the CMS experiment at point 5. This allows it to measure particles emerging  
1170 from CMS with small angles. The main goals is to measure the total, elastic and  
1171 inelastic cross-sections in pp collisions [222].

1172 The MoEDAL (Monopole and Exotics Detector At the LHC) experiment [223]  
1173 is located at the interaction point 8 together with the LHCb experiment. MoEDAL  
1174 tries to measure signatures of hypothetical particles with magnetic charge, mag-  
1175 netic monopoles.

### 1176 2.3 ALICE

1177 ALICE (A Large Ion Collider Experiment) [226] is the dedicated heavy ion ex-  
1178 periment at the LHC. ALICE was designed to cope with the expected very high  
1179 multiplicity environment of heavy ion collisions. The design allows measurement  
1180 of a large number of low momentum tracks. The different detector subsystems are  
1181 optimised to provide high momentum resolution and excellent particle identifica-  
1182 tion capabilities over a broad range of momentum.

1183 A schematic view of the ALICE detector in 2018 is presented in Figure 31.  
1184 This section will go through the composition of ALICE as it has been during run 2  
1185 between 2014 and 2018. The detector will go through significant upgrades during  
1186 Long Shutdown 2 (LS2) in 2019-2020.

1187 As in all the major high energy physics experiments the positioning of the de-  
1188 tectors follows a layered structure. Closest to the interaction point are the tracking  
1189 detectors. The main task of these detectors is to locate the position of the pri-  
1190 mary interaction vertex accurately and to record the tracks of charged particles.  
1191 To achieve this they need a very good spatial resolution close to the interaction  
1192 point. Tracking detectors do not significantly alter the tracks of traversing parti-  
1193 cles. Thus they can be located in the innermost layers.

1194 Calorimeters are designed to stop particles hitting them and thus use the ab-  
1195 sorption to measure the energy of the particles. Thus they must be located behind  
1196 the tracking detectors. ALICE has two separate calorimeter systems, the elec-  
1197 tromagnetic calorimeters measure mainly electrons and photons, while the muon

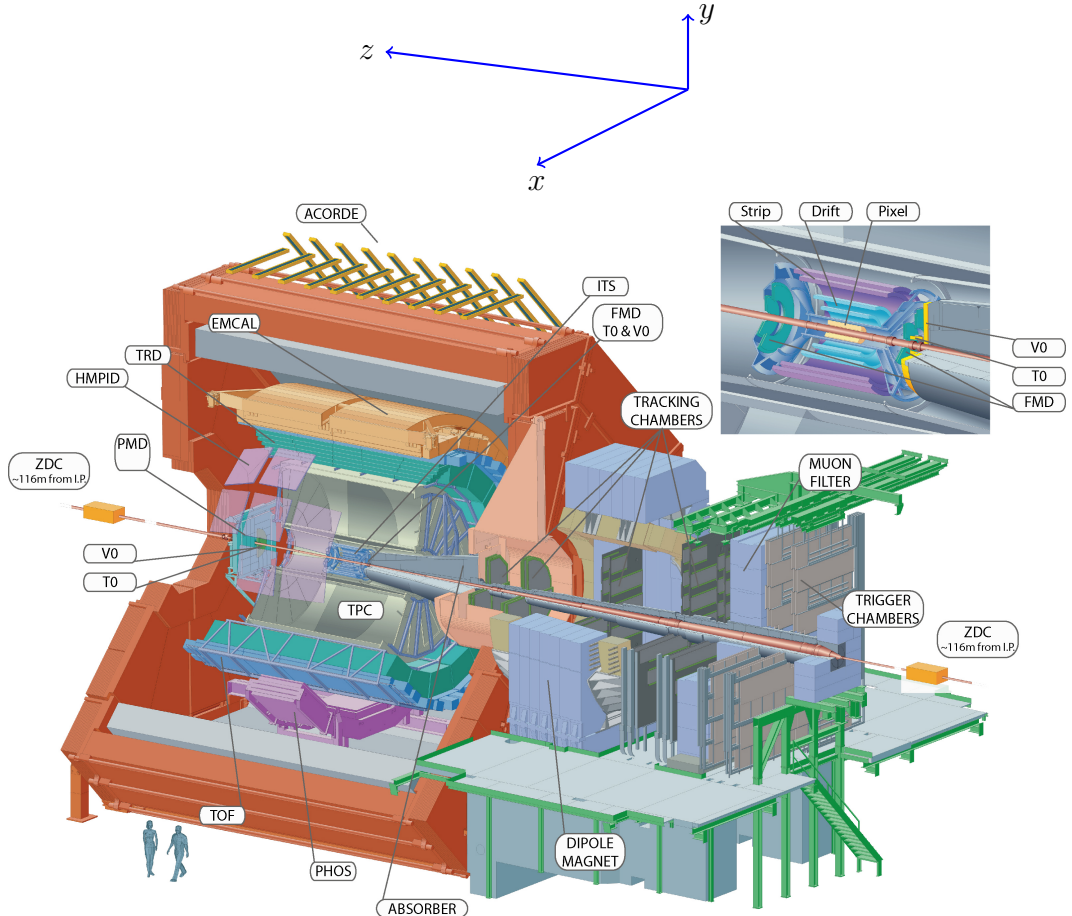


Figure 31: Schematic view of the ALICE detector with the definition of coordinates. The positive direction of  $z$  is also referred to as the A side and the negative direction as the C side

<sub>1198</sub> detection system measures muons.

### <sub>1199</sub> 2.3.1 Tracking

<sub>1200</sub> The main design guideline for the tracking detectors in ALICE was the require-  
<sub>1201</sub> ment to have good track separation and high granularity in the high multiplicity  
<sub>1202</sub> environment of heavy ion collisions. Before the LHC started heavy ion runs the  
<sub>1203</sub> wildest estimates put the particle density at 8000 charged particles per unit of ra-  
<sub>1204</sub> pidity [226]. In reality the particle density turned out to be significantly smaller,  
<sub>1205</sub> about 1600 charged particles per rapidity unit [227].

<sub>1206</sub> The main tracking detector in ALICE is the Time Projection Chamber  
<sub>1207</sub> (TPC) [228]. TPS is discussed in more detail in Section 2.3.2

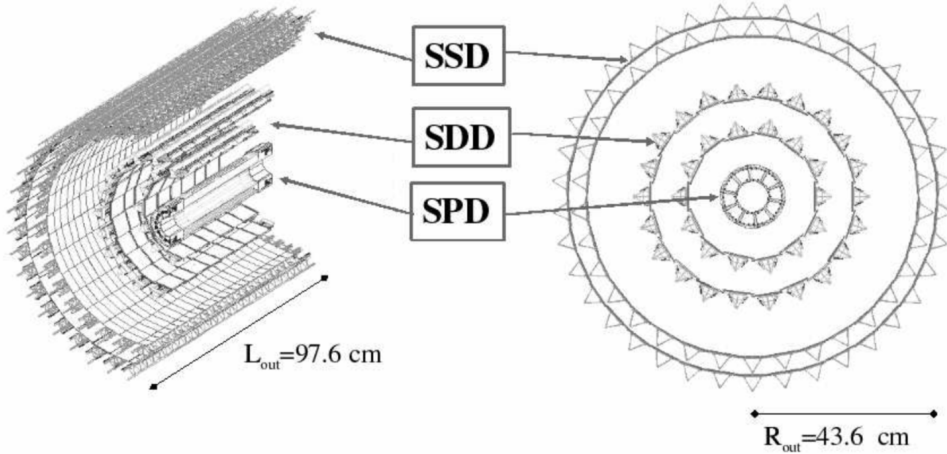


Figure 32: Schematic view of ALICE Inner Tracking System

1208 Between TPC and the beam pipe there is an array of six layers of silicon  
 1209 detectors, called the inner tracking system (ITS) [229]. The main tasks of the  
 1210 ITS are to locate the primary vertex with a resolution better than  $100 \mu m$ , to  
 1211 reconstruct the secondary vertices from decaying particles, to track and identify  
 1212 particles with momenta below 200 MeV and to compliment the momentum and  
 1213 angle measurements of TPC. During long shutdown 2 in 2019-2020 the entire ITS  
 1214 will be replaced [230]. As of 2018 the two innermost layers are made of the silicon  
 1215 pixel detector (SPD). As it is the closest detector to the interaction point it requires  
 1216 a very high spatial resolution. Thus the choice of pixel technology is natural. In  
 1217 heavy ion collisions the particle density is around 50 particles per  $cm^2$ .

1218 The next two layers together are the silicon drift detector (SDD). The layers  
 1219 are made out of homogeneous neutron transmutation doped silicon, that is ionized  
 1220 when a charged particle goes through the material. The generated charge then  
 1221 drifts to the collection anodes, where it is measured. The maximum drift time in  
 1222 SDD is about  $5 \mu s$ . This design gives very good multi-tracking capabilities and  
 1223 provides two out of the four  $dE/dx$  samples in the ITS.

1224 The two remaining layers in the ITS are the silicon strip detector (SSD). The  
 1225 strips work in a similar way as silicon pixels, but by itself one layer only provides  
 1226 good resolution in one direction. Combining two crossing grids of strips provides 2  
 1227 dimensional detection. Each charged particle will hit two intervening strips. The  
 1228 position of the hit can be deduced from the place where the strips cross each other.

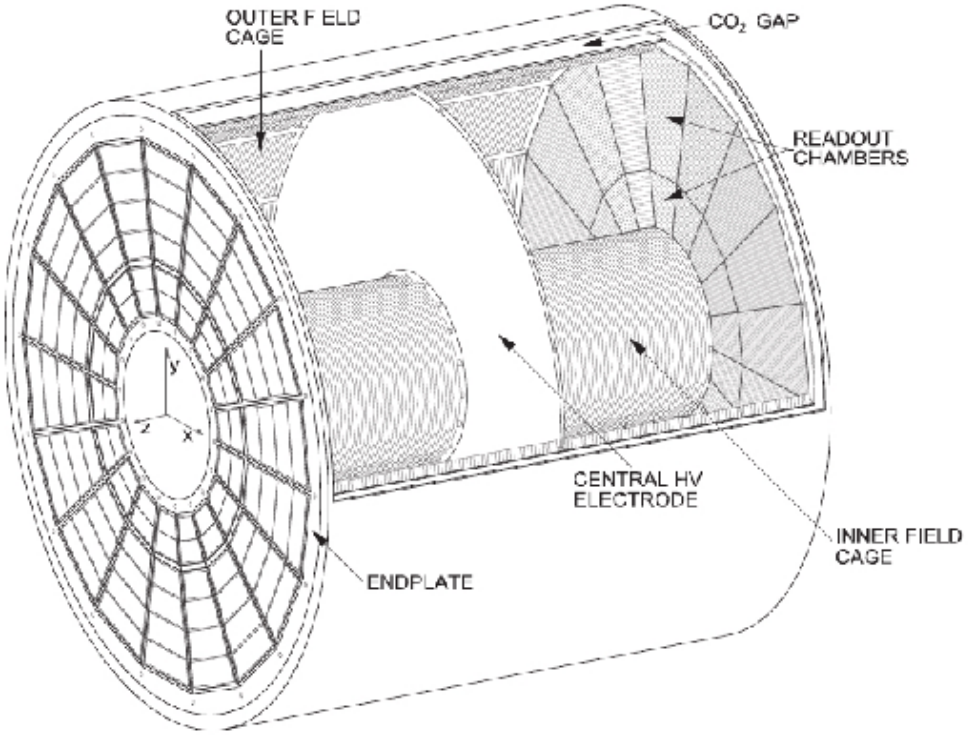


Figure 33: Schematic view of ALICE Time Projection Chamber

### **1229 2.3.2 TPC**

**1230** The time projection chamber (TPC) is a cylindrical detector filled with  $88\text{ m}^3$  of  
**1231** Ne –  $\text{CO}_2$  (90/10 %) gas mixture. The gas is contained in a field cage that provides  
**1232** an uniform electric field of  $400\text{ V/cm}$  along the z-axis. The gas content and field  
**1233** strength have been chosen for optimised charge transport, signal amplification and  
**1234** transparency for traversing particles [231] Charged particles traversing through  
**1235** the TPC volume will ionise the gas along their path. This liberates electrons that  
**1236** drift towards the end plates of the cylinder. A schematic of the TPC is shown in  
**1237** Figure 33.

**1238** The field cage is separated into two detection volumes by the central high  
**1239** voltage electrode. Both sides have a drift length of  $2.5\text{ m}$  and inner and outer  
**1240** diameters of  $1.2\text{ m}$  and  $5\text{ m}$  respectively. To provide the uniform electric field of  
**1241**  $400\text{ V/cm}$  the central electrode must provide a potential of  $100\text{ kV}$ . The maximum  
**1242** time required for electrons to drift through the chamber is about  $90\text{ }\mu\text{s}$ .

**1243** When electrons reach the end of the main cylinder they enter the readout  
**1244** chambers. The readout section of both sides consists of 18 outer chambers and

1245 18 inner chambers. Each of them is made of multiwire proportional chambers  
1246 with cathode pad readouts. This design has been used in many TPCs before.  
1247 During LS2 in 2019-2020, the multiwire chambers will be replaced by Gas Electron  
1248 Multipliers (GEMs, see Section 2.4).

1249 **2.3.3 Particle identification**

1250 One guiding principle in the design of ALICE was to achieve good particle iden-  
1251 tification (PID) over a large part of phases space and for several different particle  
1252 types. In ALICE there are several detectors taking part in the identification of  
1253 particles. In addition to the specific particle identification detectors, the general  
1254 purpose tracking detectors can be used for identification through the use of specific  
1255 energy loss  $dE/dx$  of charged particles traversing through a medium and the tran-  
1256 sition radiation emitted by charged particles when crossing the boundary between  
1257 two materials.

1258 Energy loss measurements are provided by the last four layers of the ITS de-  
1259 tector, i.e. the SDD and the SSD, thanks to their analog readout [232]. ITS can  
1260 provide particle identification in the low  $p_T$  region, up to 1 GeV, and pions re-  
1261 constructed in the standalone mode can be identified down to 100 MeV. Similar  
1262 to ITS the TPC detector provides specific energy loss measurements. TPC can  
1263 identify charged hadrons up to  $p_T$  1 – 2 GeV as well as light nuclei, He3 and He4,  
1264 providing the majority of PID information for ALICE.

1265 One of the particle identification detectors is the transition radiation detector  
1266 (TRD) [233]. Its main task is identifying electors with momenta larger than 1 GeV.  
1267 Transition radiation is produced when highly relativistic particles traverse the  
1268 boundary between two media having different dielectric constants. The average  
1269 energy of the emitted photon is approximately proportional to the Lorentz factor  $\gamma$   
1270 of the particle, which provides an excellent way of discriminating between electrons  
1271 and pion. ALICE TRD is made of a composite layer of foam and fibres. The  
1272 emitted photons are then measured in six layers of Xe/CO<sub>2</sub> filled time expansion  
1273 wire chambers.

1274 The time of flight (TOF) detector [234] uses a very simple physics principle,  
1275 i.e. calculating the velocity of the particle using the time of flight between two  
1276 points. Combining this with the momentum of particle, obtained from the tracking  
1277 detectors, one can calculate the mass of the particle, which identifies particles. The  
1278 TOF detector consists of multigap resistive wire chambers. These are stacks of  
1279 resistive plates spaced equally. They allow time of flight measurements in large  
1280 acceptance with high efficiency and with a resolution better than 100 ps.

1281 The third specific particle identification detector is the high momentum particle  
1282 identification (HMPID) detector [235]. The HMPID uses a ring imaging Cherenkov  
1283 counter to identify particles with momenta larger than 1 GeV. Particles moving

1284 through a material faster than the speed of light in the material will produce  
1285 Cherenkov radiation. The velocity of the particle determines the angle at which  
1286 the radiation is emitted. Measuring this angle gives the velocity of the particle.  
1287 This can be again used to calculate the mass of the particle, if the momentum is  
1288 known. In HMPID the material is a liquid radiator and the photons are measured  
1289 with multiwire proportional chambers in conjunction with photocathodes.

#### 1290 2.3.4 Electromagnetic Calorimeter

1291 Calorimeters are designed to measure the energy of particles. Electromagnetic  
1292 calorimeters specialise in detecting particles that interact primarily through the  
1293 electromagnetic interaction, namely photons and electrons. They are required in  
1294 many neutral meson [236] and direct photon [237] analyses. In addition the energy  
1295 information enhances jet measurements [238], as some of jet fragments can't be  
1296 detected with trackers.

1297 ALICE has two electromagnetic calorimeters, the photon spectrometer  
1298 (PHOS) [239] and the electromagnetic calorimeter (EMCal) [240]. PHOS is a  
1299 homogeneous calorimeter that consists of scintillating  $\text{PbWO}_4$  crystals, which  
1300 generate a bremsstrahlung shower and produce scintillation light. The energy of  
1301 the particle determines the amount of light produced. To improve the charged  
1302 particle rejection, PHOS includes a charged particle veto detector (CPV) [239].  
1303 PHOS is built to have a very fine granularity, making it well suited for measuring  
1304 direct photons and neutral mesons.

1305 In comparison to PHOS, EMCal has coarser granularity, but a significantly  
1306 larger acceptance, making it suitable for jet physics. The acceptance of EMCal in  
1307 the azimuthal angle is  $80 \text{ deg} < \phi < 187 \text{ deg}$ . During long shutdown 1 in 2013-2015,  
1308 EMCal was extended with the di-jet calorimeter (DCal) [241], giving an additional  
1309 acceptance region of  $260 \text{ deg} < \phi < 320 \text{ deg}$ . This provides partial back-to-back  
1310 coverage.

1311 EMcal is segmented into 10 full size super modules (SM), 5 for A side and 5 for  
1312 C side, and two 1/3 sized SMs, one for each side. This segmentation can be seen  
1313 in Figure 34. Each SM is divided into 24 strips, each covering full  $\eta$  (24 towers)  
1314 and 2 towers in  $\eta$ . Each strip is composed of  $2 \times 2$  tower modules. Thus each  
1315 full size super module includes 1152 towers and in total the EMCal is made up of  
1316 12288 towers.

1317 The build of individual towers is shown in Figure 35. Each tower is built up  
1318 from 76 alternating layers of 1.44 mm Pb and 77 layers of 1.76 mm polystyrene base  
1319 injection moulded scintillator. The lead tiles produce the shower and scintillator  
1320 tiles the light. Each tower scintillator is equipped with reflectors on all sides  
1321 to provide better gain and keep the four towers inside one module isolated. The  
1322 scintillation photons produced in the active volume of the tower are collected by 36

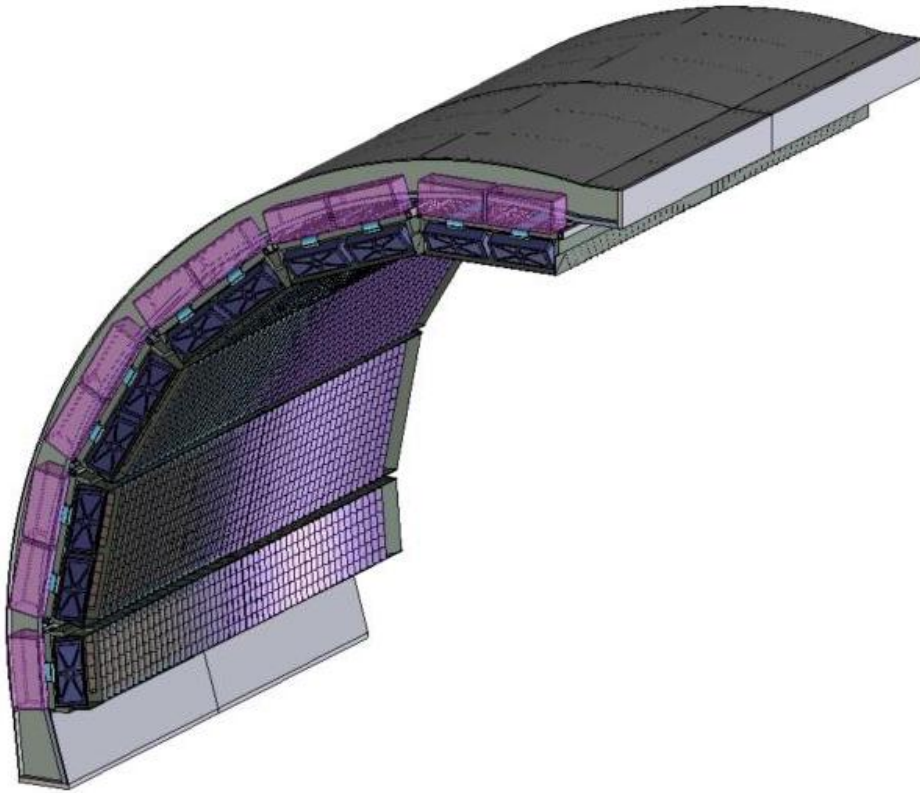


Figure 34: The EMCal detector arc, where the segmentation into 10 full size and 2  $\frac{1}{3}$ -sized (5 and 1 per side) supermodules can be seen.

1323 longitudinally placed wave length shifting light guide fibres. The light is eventually  
1324 directed to the Avalanche Photo Diodes (APD) for readout.

### 1325 2.3.5 Forward and trigger detectors

1326 ALICE includes a few small and specialised detectors of importance. The event  
1327 time is determined with very good precision ( $< 25$  ns) by the T0 detector [242].  
1328 T0 consists of two sets of Cherenkov counters that are mounted around the beam  
1329 pipe on both sides of the interaction point. T0 gives the luminosity measurement  
1330 in ALICE.

1331 Another small detector in the forward direction is the V0 detector [242]. This  
1332 consists of two arrays of segmented scintillator counters located at  $-3.7 < \eta <$   
1333  $-1.7$  and  $2.8 < \eta < 5.1$ . V0 is used as a minimum bias trigger and for rejection  
1334 of beam-gas background. Particle multiplicity in the forward direction can be  
1335 related to the event centrality. Thus V0 is the main detector used in centrality

## THE EMCAL Module Components

### Containment: 88 parts

- 1) Back (holes: 144 thru for fibers + springs + mech. support), 1
- 2) Compression (holes: 144 thru for fibers + springs), 1
- 3) Front Plate (holes: 144 thru for fibers + springs + mech. support), 1
- 4) 5) Plungers (10)
- 6) Belleville washers (75)

### Tensioning and Insulation:

#### 40 parts

- 7) Stainless steel straps (4)
- 8) Screws (24)
- 9) Flanges (8)
- 10) Light tight stickers (4)

### Sandwich:

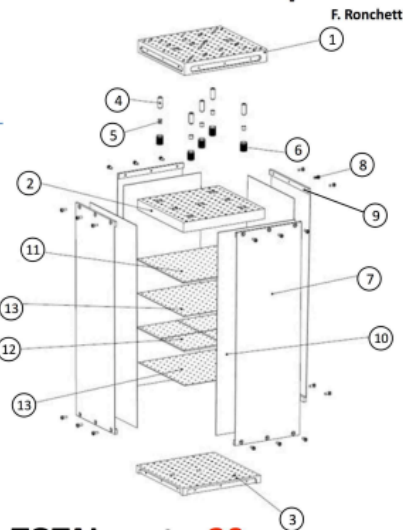
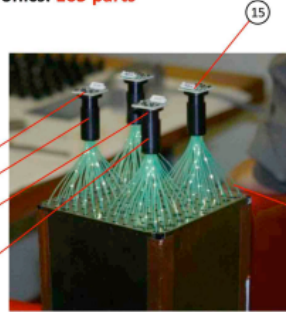
#### 538 parts

- 11) Lead tiles (76)
- 12) Scintillator tiles (308)
- 13) Bond paper sheets (154)

### Readout and Electronics:

#### 165 parts

- 14) WLS fibers (144)
- 15) APD (4)
- 16) CSP (4)
- 17) Light guides (4)
- 18) Mount (4)
- 19) Collars (4)
- 20) Diffuser (1)



**TOTAL parts: 20**

**TOTAL components: 831**

Plus cabling, GMS and mech. supports

Figure 35: The exploded EMCAL tower view

1336 determination in PbPb collisions.

1337 The multiplicity measurement of V0 is complimented by the forward multiplicity  
1338 detector (FMD) [242]. FMD includes five rings of silicon strip detectors that  
1339 make up the FMD. FMD gives acceptance in the range  $-3.4 < \eta < -1.7$  and  
1340  $1.7 < \eta < 5.0$ .

1341 During long shutdown 2 in 2019-2020, V0 and T0 will be replaced by the Fast  
1342 Interaction Trigger (FIT) detector [243]. For historical reasons elements of FIT are  
1343 also referred to as V0+ and T0+. FIT will allow centrality, event plane, luminosity  
1344 and interaction time determination in the continuous readout mode, that ALICE  
1345 will operate in after 2020.

1346 For photon multiplicity measurement ALICE has the photon multiplicity de-  
1347 tector (PMD) [244]. PMD uses two planes of gas proportional counters with a  
1348 cellular honeycomb structure. PMD gives the multiplicity and spatial distribution  
1349 of photons in the region  $2.3 < \eta < 3.7$ .

1350 On top of the ALICE magnet there is an array of 60 large scintillators called  
1351 the ALICE cosmic ray detector (ACORDE) [245]. ACORDE is used as a trigger  
1352 for cosmic rays for calibration and alignment.

1353 The only hadronic calorimeters in ALICE are the zero degree calorimeters

1354 (ZDC) [246], which are located next to the beam pipe in the machine tunnel  
1355 about 116 m from the interaction point. There are two sets of calorimeters. One  
1356 is made of tungsten, specialising in measuring neutrons, while the other, made of  
1357 brass, is specialised in measuring protons. ZDC is meant to detect spectators, i.e.  
1358 parts of the colliding ions that do not take part in the interaction. If there are more  
1359 spectators, the collisions is likely to be more peripheral. Thus ZDC gives informa-  
1360 tion about the centrality of the event especially in proton-lead collisions [201], but  
1361 also in Pb–Pb collisions [86].

1362 A new detector installed during the long shutdown 1 is the ALICE diffractive  
1363 detector (AD) [247]. AD consists of two assemblies, one in each side of the interac-  
1364 tion point, both made of two layers of scintillators. These assemblies are situated  
1365 about 17 m and 19.5 m away from the interaction points. The pseudorapidity cov-  
1366 erage is  $-6.96 < \eta < -4.92$  and  $4.78 < \eta < 6.31$ . AD greatly enhances ALICE’s  
1367 capability for diffractive physics measurements that require a large pseudorapidity  
1368 gap. During long shutdown 2 AD will be updated and integrated as a part of the  
1369 FIT detector.

### 1370 2.3.6 Muon spectrometer

1371 Outside the main magnet, ALICE has a spectrometer dedicated to measuring  
1372 muons [248]. In heavy ion physics muons are mainly used to measure the produc-  
1373 tion of the heavy quark resonances  $J/\psi$ ,  $\Psi'$ ,  $\Upsilon$ ,  $\Upsilon'$  and  $\Upsilon''$ .

1374 The muon spectrometer consists of three parts, the absorber, the muon tracker  
1375 and the muon trigger. The absorber is meant to remove the hadronic background  
1376 as efficiently as possible. After the absorber there are ten plates of thin cathode  
1377 strip tracking stations with high granularity, the muon tracker. After the muon  
1378 tracker there is a layer of iron to filter out any remaining particles, other than  
1379 muons. The muon trigger is located behind this layer. The trigger consists of four  
1380 resistive plate chambers.

### 1381 2.3.7 Triggers

1382 High energy physics experiments need triggers to select interesting physics. Ex-  
1383 periments such as CMS and ATLAS at CERN look for extremely rare events. To  
1384 produce these rare events LHC provides up to 40 million events each second. Such  
1385 amounts can’t be recorded real-time as many detectors require some time for the  
1386 readout, up to 1 ms/event in ALICE. Thus one uses triggers, i.e. a set of very fast  
1387 hardware based decisions on which events are to be saved. Additionally one needs  
1388 some confirmation that an event has even occurred to tell other detectors that the  
1389 event needs to be recorded.

1390 For ALICE the target event rates are 1 MHz for pp collisions, 0.1-2 kHz for  
1391 Pb–Pb collisions and 200 kHz for the 2013 p–Pb collisions.

1392 At ALICE the main system responsible for the trigger decisions is the AL-  
1393 ICE Central Trigger Processor (CTP) [249]. The CTP generates three levels of  
1394 hierarchical hardware triggers - Level 0, Level 1 and Level 2, (L0, L1 and L2 re-  
1395 spectively) before an event is accepted and transmitted to the Data Acquisition  
1396 system (DAQ). Afterwards additional software assessments are performed by the  
1397 High Level Trigger (HLT).

1398 Triggers can be roughly put into two classes, minimum bias triggers that make  
1399 sure no empty events are recorded, and rare triggers that require specific signatures  
1400 in ALICE detectors, such as large energy deposits in EMCal or two muons in the  
1401 muon arm acceptance.

## 1402 Minimum bias trigger

1403 Several of the ALICE detectors are used to make the initial minimum bias trigger  
1404 decisions. These include the SPD layers of ITS, V0 and T0. SPD can count the  
1405 number of hits in the first two layers of ITS. Minimum bias pp collisions typically  
1406 require at least one hit in either SPD or V0A/V0C. Similarly Pb–Pb triggers look  
1407 at both V0 and SPD hits. The p–Pb data has been mainly triggered using V0  
1408 information.

## 1409 EMCal trigger

1410 In addition to the minimum bias triggers, the most relevant trigger for this thesis  
1411 is the EMCal trigger. Parts of the EMCal trigger has been developed at the  
1412 University of Jyväskylä. Extensive details of the trigger and the development  
1413 work can be found in the thesis of Jiří Král [250]. Personally I have contributed  
1414 to the maintenance of the level 0 trigger.

1415 ALICE EMCal provides two levels of trigger signal, L0 and L1, which allows  
1416 triggering on either single shower deposits or integrated energy deposits in larger  
1417 ares, i.e. jets [251]. As inputs the trigger gets exclusive sets of  $2 \times 2$  EMCal towers,  
1418 to limit the number of channels that need to be processed. The L0 trigger then  
1419 checks for energy deposits within a rolling window of  $2 \times 2$  trigger channels ( $4 \times 4$   
1420 towers). Areas of  $4 \times 4$  towers most probably will contain only a single shower or  
1421 two adjacent showers coming from a single decayed  $\pi^0$ . Thus the trigger is called  
1422 the single shower trigger.

1423 For L0 the trigger decision is done in Trigger Region Units (TRU) that each  
1424 cover  $4 \times 42$  channels ( $8 \times 48$  towers). The amplitude from the sliding window  
1425 is compared to a constant threshold. Additionally a peak finding algorithm is  
1426 implemented to define correctly the time of the signal maximum. A single bit OR

1427 decision of all individual TRUs is forwarded to the CTP as the EMCAL L0 trigger  
1428 decision.

1429 The L0 information is additionally forwarded to the L1 trigger, which recom-  
1430 putes similar  $2 \times 2$  channel decisions to produce the single shower trigger, but L1  
1431 can perform the calculation also on the borders between trigger units. In addition  
1432 the L1 trigger can check for energy deposits inside a larger  $16 \times 16$  channel ( $32 \times 32$   
1433 towers) window, which is considered to be the jet trigger.

1434 The L1 trigger can compare up to two thresholds for each single shower and  
1435 jet trigger. There is a dedicated link in between the V0 detector and EMCAL STU,  
1436 which can provide centrality information that is used to compute a dynamical  
1437 threshold as a function of the V0 multiplicity.

1438 The trigger subsystem provides both the L0 and L1 decisions to the CTP and  
1439 DAQ.

## 1440 2.4 TPC upgrade

### 1441 2.4.1 ALICE upgrade during LS2

1442 During LS2 in 2019-2020 ALICE will go through significant modifications. The  
1443 goal is to be able have continuous readout [252] in heavy ion collisions at an  
1444 interaction rate of 50 kHz. ALICE will add a new Forward Interaction trigger  
1445 (FIT) [253] to provide trigger and timing replacing the V0 and T0 detectors. Also  
1446 the current FMD and AD detectors will be dismantled and their roles will be taken  
1447 over by FIT.

1448 Additionally the current inner tracking system (ITS) will be completely re-  
1449 placed. The current layered structure with three different technologies will be  
1450 replaced by a detector that uses pixel technology in all layers and with signifi-  
1451 cantly reduced pixel size. Additionally the first layer will be brought closer to the  
1452 beam pipe. The new ITS will have better tracking efficiency and better impact  
1453 parameter resolution [230].

1454 The muon detection will be complimented by the Muon Forward Tracker  
1455 (MFT) [254]. Based on the same technology as the new ITS, MFT will be placed  
1456 before the hadron absorber that sits in front of the existing muon spectrometer.  
1457 MFT should significantly increase the signal/background ratio in heavy quark  
1458 measurements [254].

### 1459 2.4.2 TPC upgrade

1460 Many subdetectors will make small improvements to enhance the readout rate.  
1461 The central trigger processor will be replaced and ALICE will introduce a new  
1462 framework  $O^2$  that combines both online data acquisition and offline analysis.

1463        The detector restricting the readout the most at the moment is the TPC.  
1464        The current wire chamber based system limits the readout rate to 3.5 kHz. To  
1465        achieve the 50 kHz readout rate goal the wire chambers will be replaced by a Gas  
1466        Electron Multiplier (GEM) based system. The GEMs are designed to minimise  
1467        ion backflow to allow continuous, ungated and untriggered readout. I have made  
1468        a personal contribution to the quality assurance of the new GEM readout of TPC.

1469        TPC has a total of 36 inner and 36 outer readout chambers. Each of these will  
1470        consist of 4 layers of GEM foils. The inner chambers will only have one foil for  
1471        each layer. The outer chambers are separated into three sections, each with its  
1472        own layer of foils. Each GEM foil is made up of a 50  $\mu\text{m}$  thick resistive capton  
1473        layer, coated on both sides by 5 $\mu\text{m}$  thick layers of copper. Each foils is separated  
1474        into a number (20-24 depending on the size of the foil) of distinct active areas.  
1475        The active areas are pierced densely with holes. They have 50-100 holes in the  
1476        area of a single  $\text{mm}^2$ . The density of holes changes from layer to layer. The two  
1477        middle layers of foils have a larger (double) pitch (smaller hole density) while the  
1478        top and bottom layers have a smaller (normal) pitch (larger hole density).

1479        The purpose of the multilayered structure is to reduce the ion backflow [255,  
1480        256]; not only one layer of GEM foils will be installed, but a 4 layer stack. In the  
1481        stack there are 2 standard pitch GEM foils, where the pitch size, i.e. the separation  
1482        of the holes inside a foil is around 140  $\mu\text{m}$ , and 2 large pitch GEM foils, there the  
1483        hole spacing is two times larger, 280  $\mu\text{m}$ . The two outer layers will have standard  
1484        pitch and the two middle layers have large pitch. The middle layers with large  
1485        pitch serve as extra insulator against the ion backflow. Additionally the setup  
1486        allows operating individual GEM foils at lower voltages and still have an increase  
1487        in the gain of a few orders of magnitude [257].

1488        The holes have a conical shape which they acquire during a two step chemical  
1489        etching process. The designed inner and outer diameters of the holes are  $50 \pm 5 \mu\text{m}$   
1490        and  $70 \pm 5 \mu\text{m}$  respectively. Figure 36 shows the cross-section of a hole alongside  
1491        with the operation principle of a GEM foil.

1492        The working principle of these foils is based on the Townsend avalanche phe-  
1493        nomenon [258], which is also used in proportional counters such as Geiger counters.  
1494        There is a large potential difference (140-400 V) applied to the two sides of the  
1495        foil, which results in large field in each hole. Electrons gain energy in the field and  
1496        if the electric field is strong enough, the free electron can gain sufficient velocity  
1497        (energy) to liberate another electron when it next collides with a molecule. The  
1498        two free electrons then travel along the electric field and can gain sufficient energy  
1499        from the electric field to cause further impact ionisations, and so on, leading to a  
1500        chain reaction. Under the right conditions a single electron entering any hole will  
1501        create an avalanche containing 100–1000 electrons; this is the gain of the GEM  
1502        foil.

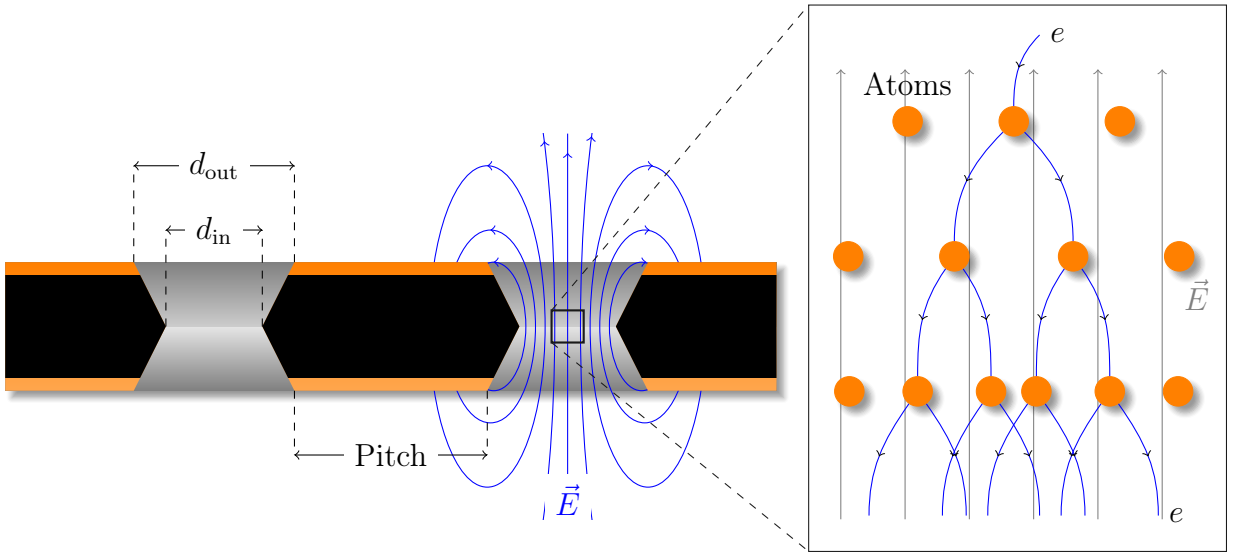


Figure 36: *left* Cross-section of a GEM foil. (Not to scale). The hole diameters are  $d_{in} = 50 \pm 5 \mu\text{m}$  and  $d_{out} = 70 \pm 5 \mu\text{m}$  and pitch is either 140 or 280  $\mu\text{m}$ . *right* The amplification of a GEM foil is based on the Townsend avalanche phenomenon [258]. Electrons entering the electric field inside the hole are accelerated. If they gain enough energy before colliding with atoms they can liberate additional electrons, which are further accelerated leading to a chain reaction.

1503 As opposed to wire chambers, which typically have one voltage setting, a GEM-  
 1504 based detector requires several independent voltage settings: there is a drift voltage  
 1505 which drives the electrons from the ionisation point to the GEM, an amplification  
 1506 voltage, and an extraction voltage that brings electrons from the GEM exit to the  
 1507 readout plane. In a multilayer system this is further complicated. The voltages  
 1508 between layers of foils can be tuned individually optimising amplification and  
 1509 preventing ion backflow.

### 1510 Quality Assurance of the GEM foils

1511 The GEM foils are produced at CERN, where they will undergo a basic QA (QA-B)  
 1512 procedure, that includes a coarse optical inspection for any large defects ( $\gtrsim 1 \text{ mm}$ )  
 1513 and a short term high voltage measurement. Afterwards the foils are sent for an  
 1514 advanced quality assurance (QA-A) procedure which is performed in one of the  
 1515 two QA-A centers, one in the Helsinki Institute of Physics (HIP) and one in the  
 1516 Wigner Research Centre in Budapest. Details of the QA-A procedure can be found  
 1517 in the thesis of Márton Vargyas [259] and in [260]. In the QA-A centers all foils  
 1518 are put through a detailed optical scanning process and a long term high voltage  
 1519 measurement. I was personally performing the QA production in Helsinki for the

1520 final 6 months of the project.

1521 The optical scan is performed with the help of a scanning robot. The setup  
1522 along with most of the software was developed at the Detector Laboratory of the  
1523 Helsinki Institute of Physics [261]. The optical scan is able to distinguish every  
1524 single hole on the GEM foil and measure their properties. The purpose of the  
1525 scan is two-fold; to catch defects that could affect the performance and classify the  
1526 foils based on their hole parameters. It is expected that these are connected with  
1527 the foil's electric properties [261]. For example, smaller holes create more intense  
1528 and focused fields, which would result in larger amplification of their avalanche  
1529 electrons, i.e. the local gain is expected to be larger.

1530 After the optical scanning, the foils are subjected to a long term (5-12 hours)  
1531 high voltage leakage current measurement. Each segment of the GEM foil is con-  
1532 nected to a high voltage of 500 V and the leakage current is measured separately  
1533 for each segment. The accepted leakage current in each segment is 0.16 nA. Foils  
1534 that fail the criteria are sent to CERN for recleaning or repairing, after which they  
1535 will go through the QA pipeline again.

1536 Additionally some foils will be put through a gain mapping procedure. This  
1537 process is time consuming and can only be performed in the QA-A center in  
1538 Budapest. Thus it was done for only a small subset of foils. However, by measuring  
1539 the gain in some foils the gain can be correlated with foil properties. Thus the  
1540 single foil gain can be predicted based on the results of the optical scan. Details  
1541 can be found in [259].

### **3 Event and track selection**

The  $\sqrt{s_{\text{NN}}} = 5.02$  TeV p–Pb ( $1.3 \cdot 10^8$  events,  $\mathcal{L}_{\text{int}} = 62 \text{ nb}^{-1}$ ) collisions were recorded in 2013 by the ALICE detector [217]. The details of the performance of the ALICE detector during LHC Run 1 (2009–2013) are presented in Ref. [262].

#### **3.1 Event selection**

This analysis uses both a minimum bias trigger and an EMCal based trigger to select the analysed events. For the 2013 p–Pb collisions minimum bias events are required to have signals in both V0A and V0C. The timing difference between the two stations is also used to reduce the contamination of the data sample from beam-gas events [262].

EMCal is used to provide the jet trigger used in triggered datasets. EMCal can be used to trigger on single shower deposits or energy deposits integrated over a larger area. Latter case is used for jet triggers. The EMCal trigger definition in the 2013 p–Pb collisions requires an energy deposit of either 10 GeV for the low threshold trigger or 20 GeV for the high threshold trigger in a  $32 \times 32$  patch size. Triggers, V0 and EMCal are discussed in more detail in sections 2.3.5, 2.3.7 and 2.3.4.

#### **3.2 Track reconstruction**

The analysis uses charged tracks that are reconstructed with the Inner Tracking System (ITS) [263] and the Time Projection Chamber (TPC) [231]. These are discussed in sections 2.3.1 and 2.3.2. A detailed overview of track reconstruction in ALICE can be found from [262].

The track reconstruction procedure is shown in Figure 37. The figure shows only one track, but in reality the reconstruction has to deal with many tracks. The main reconstruction of tracks starts in TPC. There are 159 tangential pad rows in the TPC readout chambers. The track reconstruction starts from the outermost layer and the hits are paired with hits in the next layer inwards, taking into account a proximity cut. When this track finding procedure hits the innermost pad row in TPC, this information is used as an initial seed for the track finding in ITS. Similar procedure of pairing adjacent layers with a proximity cut is repeated in ITS.

After the reconstruction of tracks in ITS is completed, all the tracks are extrapolated to their point of closest approach to the preliminary interaction vertex. Then the second track fitting step begins, this time starting from the interaction point and proceeding outwards. A Kalman filter [264] technique is used to do the new fit using the hits found in the previous stage. This time the tracks are matched

1578 also to the other detectors in the central barrel beyond TPC. When this step is  
1579 complete, a final refit from the outermost TPC pad rows towards the interaction  
1580 point is performed. The final track parameters come from this refit.

1581 With the final track parameters the primary vertex can be determined with  
1582 better accuracy than with only SPD information. The tracks are extrapolated to  
1583 the nominal beam line and a weighted average of the points of closest approach  
1584 determines the accurate primary vertex position.

1585 The final step of the track reconstruction is the determination of the secondary  
1586 vertices. For this, all the tracks whose distance of closest approach (DCA) to  
1587 the primary vertex is larger than a defined minimum value are selected. For these  
1588 tracks, points of closest approaches are determined for pairs of tracks. If the tracks  
1589 are sufficiently close to each other and show characteristics of short lived particle  
1590 decays, these points are identified as secondary vertices.

1591 Combining the information from the ITS and the TPC provides a resolution  
1592 ranging from 1 to 10 % for charged particles with momenta from 0.15 to 100 GeV/c.  
1593 For tracks without the ITS information, the momentum resolution is comparable  
1594 to that of ITS+TPC tracks below transverse momentum  $p_T = 10 \text{ GeV}/c$ , but for  
1595 higher momenta the resolution reaches 20 % at  $p_T = 50 \text{ GeV}/c$  [262, 266].

## 1596 Track selection

1597 In p–Pb collisions the tracks are selected following the hybrid approach [267]  
1598 which ensures a uniform distribution of tracks as a function of azimuthal angle  
1599 ( $\varphi$ ). The parameters in the approach are summarised in Table 2.

1600 The first requirements are on the quality of the track fit in ITS and TPC.  
1601 The ITS requirement only removes tracks that are clear outliers. For TPC the  
1602 requirement is much more strict. For step 1 it is required that a track has 3 out  
1603 of the 6 possible hits in ITS, one of which must be in the SPD. In step 2 this  
1604 is replaced by an additional vertex constraint, where the primary vertex itself is  
1605 added as a point to the track to improve the momentum resolution.

1606 For the TPC, 70 crossed pad rows out of the maximum 159 is required. This  
1607 measures the effective track length inside the TPC. This takes into account the  
1608 possibility of having pad rows missing in the middle of the track due to charge in  
1609 these clusters being below the threshold for some reason. Additionally it is required  
1610 that the ratio between crossed rows and findable clusters is at least 0.8. Findable  
1611 clusters are defined as the number of geometrically possible clusters which can be  
1612 assigned to a track, taking into account dead zones due to chamber boundaries  
1613 and limited  $\eta$ -acceptance. For both steps of the hybrid cut it is required that the  
1614 fraction of clusters shared with several tracks is less than 40%.

1615 The remaining cuts are meant to make sure that the measured tracks are really  
1616 produced in the primary collision. A track might gain a kink due to a particle

Table 2: Parameters in the hybrid track cut

Track Cut	Step 1	Step 2
$\chi^2 / \text{ITS cluster}$	< 36	< 36
$\chi^2 / \text{ITS cluster}$	< 4	< 4
Hits in ITS	3	0
ITS hit requirements	1 in SPD	No requirement
Vertex constraint	No	Yes
Number of crossed rows in TPC	70	70
TPC crossed rows over findable clusters	> 0.8	> 0.8
Fraction of shared TPC clusters	< 0.4	< 0.4
Kink daughters	Rejected	Rejected
$\text{DCA}_{xy}$	< 3.2 cm	< 3.2 cm
$\text{DCA}_z$	< 2.4 cm	< 2.4 cm
Other		Rejected by step 1

<sub>1617</sub> scattering decay. The particle after such a kink, a kink daughter, is rejected in  
<sub>1618</sub> the cuts, as it no longer describes the properties of the primary collisions. The  
<sub>1619</sub> final cuts are on the distance of closest approach (DCA) of the track to primary  
<sub>1620</sub> vertex. To have confidence that the track comes from the primary collision, the  
<sub>1621</sub> track must be close enough to the primary vertex. The cuts are different for the  
<sub>1622</sub> distance along ( $\text{DCA}_z$ ) and perpendicular to ( $\text{DCA}_{xy}$ ) the beam axis.

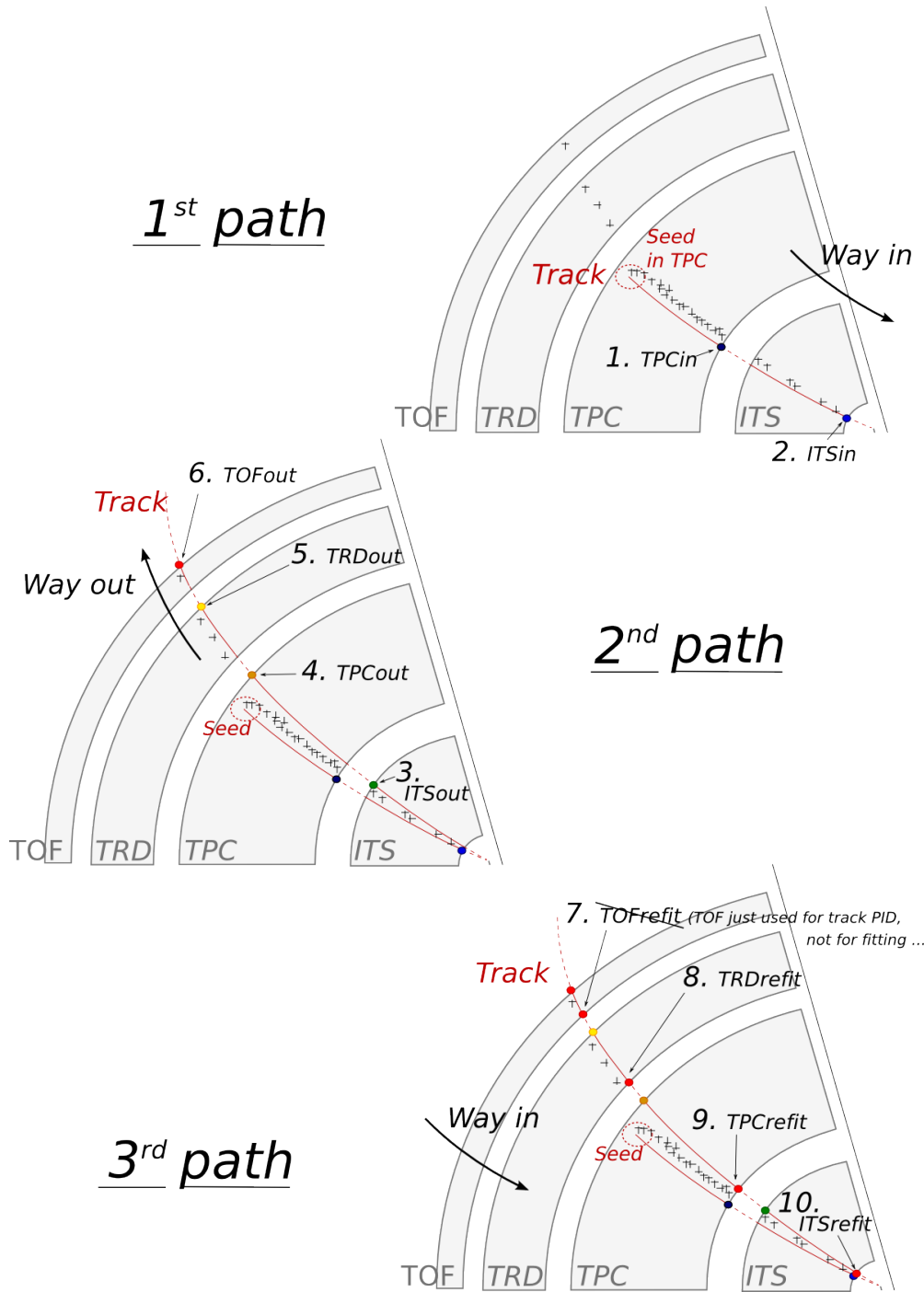


Figure 37: Principles of tracking in the ALICE experiment, showing the three successive paths allowing to build a track and refine its parameters. Numbers ranging from 1 to 10 mention the bits that are activated in case of success during the propagation of the Kalman filter at the considered stage. Figure from [265]

### 1623 3.3 Cluster selection

1624 Neutral particles used in jet reconstruction are reconstructed by the Electromagnetic  
 1625 Calorimeter (EMCal) [240]. The EMCal covers an area with a range of  
 1626  $|\eta| < 0.7$  in pseudorapidity and 100 deg in azimuth. EMCal is complimented with  
 1627 the Dijet Calorimeter (DCal) [241] and Photon Spectrometer (PHOS) [239] that  
 1628 are situated opposite of the EMCal in azimuth. PHOS covers 70 degrees in azimuth  
 1629 and  $|\eta| < 0.12$ . The DCal is technologically identical to EMCal. The DCal  
 1630 coverage spans over 67 degrees in azimuth, but in pseudorapidity the mid region  
 1631 is occupied by the PHOS. In between PHOS and DCal active volumes, there is a  
 1632 gap of 10 cm. DCal is fully back-to-back with EMCal.

1633 The clusters used in the analysis were obtained from the EMCal clusteriser.  
 1634 The parameters used in the clusteriser are summarised in Table 3. The clusteriser  
 1635 searches for a tower with energy deposit greater than a defined seed energy and  
 1636 merges all surrounding (sharing a side) towers with energy deposit higher than a  
 1637 defined threshold. In the next step all towers sharing a side with already included  
 1638 towers are added, again requiring that the energy deposits exceeds the threshold.  
 1639 The algorithm can identify local minima and halts the clustering in case that the  
 1640 neighbouring tower energy is higher. Already clustered towers are removed from  
 1641 the pool, so one tower can only be clustered once.

1642 Highly energetic calorimeter hits should spread into several towers as the elec-  
 1643 tromagnetic shower evolves. However, some clusters with high energy have their  
 1644 energy located in a single tower. These are believed to come from a slow neutron  
 1645 hitting the APD readout of the towers. They are referred to as exotic clusters.  
 1646 The measure of exotoxicity is denoted as

$$1 - \frac{E_{\text{cross}}}{E_{\text{max}}}, \quad (42)$$

1647 where  $E_{\text{max}}$  is the energy in the most energetic tower and  $E_{\text{cross}}$  is the sum of the  
 1648 four towers neighbouring the most energetic one. The closer this is to 1, the more

Table 3: Parameters used in the EMCal clusteriser

Setting	Value
Clusteriser seed	0.2 MeV
Clusteriser cutoff	0.05 MeV
Cells in cluster	> 1
Track matching radius	0.025
Fiducial cut	1 tower
Exotic cut	0.97
Minimal cluster Energy	0.3 GeV

1649 exotic the cluster is and the larger the probability that it is fake. Cut of 0.97 has  
1650 been adopted as default for analyses using EMCal, including the one presented in  
1651 this thesis. Any clusters above this cut are removed.

1652 A method of matching the cluster position to TPC track extrapolation is used  
1653 to suppress charged hadron contribution to hits in EMCal. Tracks identified by the  
1654 tracking detectors are extrapolated close to the EMCal surface, where the closest  
1655 cluster is found and the track extrapolation is continued until reaching the same  
1656 depth as the cluster. The remaining distance in between the extrapolated track  
1657 and the cluster is then used to reject hadronic hits. Clusters matched to charged  
1658 tracks are removed from the analysis as well as clusters being identified as fake.

## 1659 4 Analysis method

### 1660 4.1 Jet Finding

1661 The analysis uses reconstructed jets as estimates of the original parton. Jet recon-  
1662 struction essentially combines nearby tracks into jets.

1663 Collisions between hadrons are never as clean as electron-electron collisions.  
1664 Even for a proton-proton collision there are participant partons, that will produce  
1665 a soft background in addition to the hard scattering products. Jet reconstruction  
1666 must deal with this soft background. The reconstruction is never perfect, one can  
1667 have uncorrelated tracks that get included in the jet and some tracks originating  
1668 from the parton are missed by the reconstruction. There are several methods to  
1669 perform the reconstruction, all of which require some kind of size parameter, which  
1670 cuts out jet participants too far from the jet axis. The tracks that are grouped  
1671 into a jet are referred to as jet constituents.

1672 In each collision event, the jets are reconstructed using FastJet [268] with the  
1673 anti- $k_T$  algorithm [269]. Jets for  $R=0.4$  are selected in  $|\eta| < 0.25$  to satisfy the  
1674 fiducial acceptance of the EMCAL. In jet reconstruction both charged tracks with  
1675  $p_T > 0.15 \text{ GeV}/c$  and neutral clusters with  $p_T > 0.30 \text{ GeV}/c$  are considered. Clus-  
1676 ters that match charged tracks are removed before jet reconstruction. The analysis  
1677 is then performed by analysing the charged jet constituents and results are pre-  
1678 sented in terms of the jet transverse momentum  $p_{T,\text{jet}}$ .

#### 1679 4.1.1 Anti $k_T$ algorithm

1680 Jets are reconstructed using the anti- $k_T$  algorithm [269]. The algorithm works by  
1681 trying to undo the splittings through combining protojets. First the algorithm  
1682 creates a list of protojets. At the beginning the list is populated by converting  
1683 each track in the event into a protojet. Then the algorithm proceeds by combining  
1684 these protojets. A simplified picture of the process for a limited number of tracks  
1685 is shown in Figure 38

1686 The algorithm calculates distance measures for each individual protojet and  
1687 for each possible pair of protojets. For individual protojets this depends on the  
1688 transverse momentum of the track.

$$k_{T,i}^2 = p_{T,i}^{2p} \quad (43)$$

1689 For each pair of protojets the distance measure is calculated as

$$k_{Ti,j}^2 = \min(p_{Ti}^{2p}, p_{Tj}^{2p}) \frac{\Delta R_{i,j}^2}{D^2}, \quad (44)$$

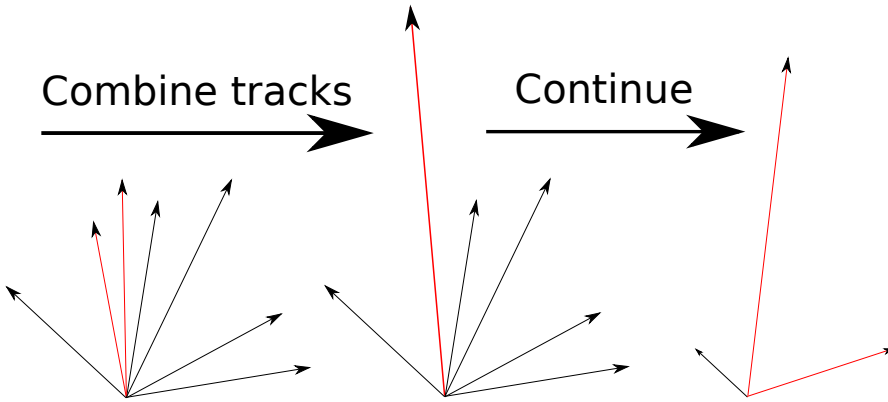


Figure 38: A simple example of the antil- $k_T$  algorithm in progress. The red tracks in the leftmost figure are identified to have the smallest  $k_{T,i}$  in the event and are combined into the red track of the middle figure. As this continues the remaining tracks are added to this or other jets. One tracks was deemed to be isolated enough to be counted as a protojet by itself. Note that the rightmost figure is zoomed out.

1690 where

$$R_{i,j} = (\phi_i - \phi_j)^2 + (y_i - y_j)^2. \quad (45)$$

1691 If  $k_{Ti}$  is the smallest quantity then the protojet is a jet and it is removed from  
 1692 further consideration. If  $k_{Ti,j}$  is the smallest quantity the two protojets  $i$  and  $j$  are  
 1693 merged. This is repeated until no protojets are left.

1694 The choice of the power  $p$  in the distance measure depends on the algorithm  
 1695 used

- 1696 •  $p = 1$ :  $k_T$  algorithm
- 1697 •  $p = 0$ : Cambridge Aachen algorithm
- 1698 •  $p = -1$ : anti- $k_T$  algorithm

1699 With the choice  $p = -1$  in anti- $k_T$  algorithm, the softest splittings are un-  
 1700 done first. One consequence of the power choice in the anti- $k_T$  algorithm is that  
 1701 reconstructed jets have a shape close to circular.

## 1702 4.2 Definition of $j_T$

1703 The reconstructed jet axis is used for  $j_T$  reference. Any charged track within a  
 1704 fixed cone with radius  $R$  is taken as a jet constituent, as opposed to using the  
 1705 constituent list provided by the jet algorithm. Anti- $k_T$  produces jets that are

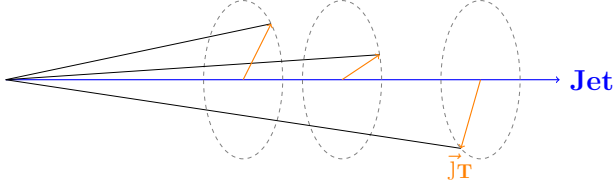


Figure 39: Illustration of  $\vec{j}_T$ . The jet fragmentation transverse momentum,  $\vec{j}_T$ , is defined as the transverse momentum component of the track momentum,  $\vec{p}_{\text{track}}$ , with respect to the jet momentum,  $\vec{p}_{\text{jet}}$ .

very circular in shape. Thus this doesn't change the constituent list considerably.  
Calorimeter clusters are used only in jet reconstruction.

The jet fragmentation transverse momentum,  $\vec{j}_T$ , is defined as the component of the constituent track momentum,  $\vec{p}_{\text{track}}$ , transverse to the jet momentum,  $\vec{p}_{\text{jet}}$ . It represents the transverse kick with respect to the initial hard parton momentum that is given to a fragmenting particle during the fragmentation process, which is a measure of the momentum spread of the jet fragments.

The resulting  $\vec{j}_T$  is illustrated in Fig. 39. The length of the  $\vec{j}_T$  vector is

$$j_T = \frac{|\vec{p}_{\text{jet}} \times \vec{p}_{\text{track}}|}{|\vec{p}_{\text{jet}}|}. \quad (46)$$

Resulting  $j_T$  distributions are shown as

$$\frac{1}{j_T} \frac{dN}{dj_T} \quad (47)$$

distributions. The logic behind this is that  $j_T$  is inherently a two-dimensional observable, comprised of  $j_{Tx}$  and  $j_{Ty}$  components. So the actual physical observable would be

$$\frac{d^2N}{dj_{Tx} dj_{Ty}} \quad (48)$$

Changing into polar coordinates with  $j_{Tr} = j_T$  and  $\theta$  gives

$$\frac{d^2N}{j_T dj_T d\theta}, \quad (49)$$

where  $j_T$  over the azimuth  $\theta$  should stay constant and it can be integrated over, which gives

$$\frac{1}{2\pi} \frac{dN}{j_T dj_T}. \quad (50)$$

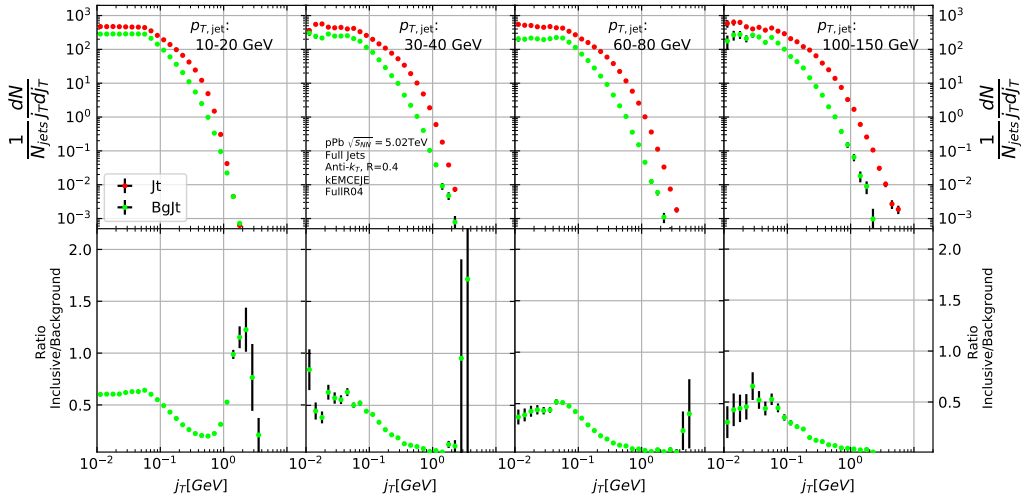


Figure 40: Inclusive  $j_T$  with background

1721 Results of the raw inclusive  $j_T$  distribution in four  $p_{T,\text{jet}}$  bins with background  
 1722 are shown in Figure 40. Background, i.e. the contribution from the underlying  
 1723 event, is further discussed in Section 4.4

### 1724 4.3 Unfolding detector effects

1725 The raw inclusive  $j_T$  distributions are corrected for the detector inefficiency with  
 1726 an unfolding procedure. The procedure uses response matrices obtained from a  
 1727 PYTHIA [270] simulation.

1728 Measured distributions are affected by two main factors; Limited acceptance -  
 1729 The probability to observe a given event is less than one and limited resolution -  
 1730 Quantity  $x$  cannot be determined exactly, but there is a measurement error. True  
 1731  $f(x)$  and measured  $g(y)$  distributions are connected by a convolution integral.  
 1732 Including statistical fluctuations this becomes

$$\hat{g}(y) = \int_a^b A(y, x) f(x) dx + \epsilon(y), \quad (51)$$

1733 where  $A$  is the detector response obtained by (for example) Monte Carlo simula-  
 1734 tions and  $\epsilon(y)$  is the term coming from statistical fluctuations. If  $x$  and  $y$  are  
 1735 discrete variables we have

$$\hat{g}_i = \sum_{j=1}^m A_{ij} f_j + \epsilon_i, \quad (52)$$

1736 where  $i$  and  $j$  give the  $j_T$  bins in the true and measured distributions.  $f_j$  and  
1737  $g_i$  give the counts in these bins. Or in matrix form

$$\hat{g} = Af + \epsilon, \quad (53)$$

1738 where  $\hat{g}$  and  $f$  are vectors corresponding to the measured and true histograms. If  
1739 the only detector effect is limited acceptance,  $A$  is a diagonal matrix, i.e.  $A_{ij} =$   
1740 0 for  $i \neq j$ . We want to deduce the true distribution  $f$ , when the measured  
1741 distribution  $g$  is known. In a general discrete case the (naive) solution is obtained  
1742 by the inverse matrix

$$\hat{f} = A^{-1}\hat{g} \quad (54)$$

1743 However this usually leads to oscillating solutions and determining the inverse  
1744 matrix can be difficult.

1745 Two common methods to perform this inversion are Bayesian and SVD unfold-  
1746 ing methods. Often the solution requires some additional *a priori* information.  
1747 For example the solution should be smooth in most cases.

#### 1748 4.3.1 Bayesian unfolding

1749 The bayesian (iterative) method is based on the Bayes formula [271].

$$P(C_i|E_j) = \frac{P(E_j|C_i) P_0(C_i)}{\sum_{l=1}^{n_C} P(E_j|C_l) P_0(C_l)}, \quad (55)$$

1750 i.e. the probability of Cause  $C_i$  ("truth") given Effect  $E_j$  ("observed") is propor-  
1751 tional to the probability of observing  $E_j$  given  $C_i$ ,  $P(E_j|C_i)$  (response matrix) and  
1752 the true distribution  $P_0(C_i)$ .

1753 In the unfolding procedure  $P_0$  is given some starting distribution, either a  
1754 uniform distribution or some guess of the final distribution. Taking into account  
1755 the inefficiency this gives

$$\hat{n}(C_i) = \frac{1}{\epsilon_i} \sum_{j=1}^{n_E} n(E_j) P(C_i|E_j), \quad (56)$$

1756 where

$$P(C_i|E_j) = \frac{P(E_j|C_i) P_0(C_i)}{\sum_{l=1}^{n_C} P(E_j|C_l) P_0(C_l)}, \quad (57)$$

1757 and  $n(E_j)$  are the observed frequencies. First  $P(C_i|E_j)$  is calculated with the  
1758 uniform distribution or best guess of the shape of the distribution. This is then  
1759 used to calculate the new distribution  $\hat{P}(C_i)$

$$\hat{N}_{true} = \sum_{i=1}^{n_C} \hat{n}(C_i), \quad \hat{P}(C_i) = P(C_i|\hat{n}(E)) = \frac{\hat{n}(C_i)}{\hat{N}_{true}} \quad (58)$$

1760  $P_0$  is then replaced with  $\hat{P}$  and the procedure is repeated until an acceptable  
1761 solution is found. One way to gauge the acceptability is measuring the change  
1762 between iterations. Initially there is a large change between iterations, but it  
1763 should get small when close to the final distribution. The number of iterations  
1764 should be as low as possible, as the errors increase when going further in the  
1765 iterations, but the number of iterations must be high enough so that the correct  
1766 distribution is extracted.

1767 The bayesian procedure alongside with the SVD unfolding method are imple-  
1768 mented in the RooUnfold package [272], which is used to perform the unfolding  
1769 in practice. SVD unfolding is another procedure that utilises the Singular Value  
1770 Decomposition (SVD) of the response matrix to find the inverse of the response  
1771 matrix [273].

## 1772 Error propagation in the Bayesian procedure

1773 The measured distribution has some statistical uncertainty, this should be reflected  
1774 in the unfolded distribution. Additionally the response matrix may have some  
1775 uncertainty if the statistics used in the Monte Carlo simulation were limited.

1776 For errors originating from the measured distribution RooUnfold uses the error  
1777 propagation matrix

$$\frac{\partial \hat{n}(C_i)}{\partial n(E_j)} = M_{ij} + \frac{\hat{n}(C_i)}{n_0(C_i)} \frac{\partial n_0(C_i)}{\partial n(E_j)} - \sum_{k=1}^{n_E} \sum_{l=1}^{n_C} \frac{n(E_k) \epsilon_l}{n_0(C_l)} M_{ik} M_{lk} \frac{\partial n_0(C_l)}{\partial n(E_j)}, \quad (59)$$

1778 where  $\hat{n}(C_i)$  is the unfolded result from Eq. 58. This depends upon the matrix  
1779  $\frac{\partial n_0(C_i)}{\partial n(E_j)}$ , which is  $\frac{\partial \hat{n}(C_i)}{\partial n(E_j)}$  from the previous iteration. In the first iteration,  $\frac{\partial n_0(C_i)}{\partial n(E_j)} = 0$   
1780 and  $\frac{\partial \hat{n}(C_i)}{\partial n(E_j)} = M_{ij}$ .

1781 The error propagation matrix  $V$  is used to obtain the covariance matrix on the  
1782 unfolded distribution

$$V(\hat{n}(C_k), \hat{n}(C_l)) = \sum_{i,j=1}^{n_E} \frac{\partial \hat{n}(C_k)}{\partial n(E_i)} V(\hat{n}(E_i), \hat{n}(E_j)) \frac{\partial \hat{n}(C_l)}{\partial n(E_j)}, \quad (60)$$

1783 where  $V(\hat{n}(E_i), \hat{n}(E_j))$  is the covariance matrix of the measurements. In count-  
1784 ing experiments common in particle physics, each bin is independently Poisson  
1785 distributed, with

$$V(\hat{n}(E_i), \hat{n}(E_j)) = n(E_i) \delta_{ij} \quad (61)$$

1786 The error propagation matrix for the response matrix is

$$\frac{\partial \hat{n}(C_i)}{\partial P(E_j|C_k)} = \frac{1}{\epsilon_i} \left( \frac{n_0(C_i) n(E_j)}{f_j} - \hat{n}(C_i) \right) \delta_{ik} - \frac{n_0(C_k) n(E_j)}{f_j} M_{ij} + \\ \frac{\hat{n}(C_i)}{n_0(C_i)} \frac{\partial n_0(C_i)}{\partial P(E_j|C_k)} - \frac{\epsilon_i}{n_0(C_i)} \sum_{l=1}^{n_E} \sum_{r=1}^{n_C} n(E_l) M_{il} M_{rl} \frac{\partial n_0(C_r)}{\partial P(E_j|C_k)}, \quad (62)$$

where  $\frac{\partial n_0(C_i)}{\partial P(E_j|C_k)}$  is the error propagation matrix from the previous iteration,  $\frac{\hat{n}(C_i)}{\partial P(E_j|C_k)}$ . For the first iteration, this is zero and the final two terms in Eq. 62 disappear.

The covariance matrix due to these errors is given by

$$V(\hat{n}(C_k), \hat{n}(C_l)) = \sum_{j,s=1}^{n_E} \sum_{i,r=1}^{n_C} \frac{\partial \hat{n}(C_k)}{\partial P(E_j|C_i)} V(P(E_j|C_i), P(E_s|C_r)) \frac{\partial \hat{n}(C_l)}{\partial P(E_s|C_r)}, \quad (63)$$

where  $V(P(E_j|C_i), P(E_s|C_r))$  can be taken as multinomial, Poisson or other distribution.

### 4.3.2 Toy Monte Carlo

A toy Monte Carlo simulation was performed to see the performance of unfolding in an ideal case. The simulations samples jet  $p_T$  values from the observed  $p_T$  distribution. Starting from this  $p_T$  the simulations starts creating tracks with

$$p_{\text{track}} = z_{\text{track}} p_{T,\text{jet}} \quad (64)$$

where  $z_{\text{track}}$  is sampled from the observed  $z$  distribution. Tracks are given random  $\eta$  and  $\phi$  values from uniform distributions centred at 0. All tracks below 0.15 GeV are discarded. Sampling is continued until the sum of the track transverse momenta exceeds the jet transverse momentum. The sum of all the track momenta is calculate. This is sum is then defined to be the jet.

Simultaneously a  $p_T$  dependant observation efficiency is applied to the tracks and a separate observed jet is calculated using only the observed tracks. Additionally a set of fake tracks is added to the observed jet. Fake tracks are generated identically to normal tracks, except for  $p_{T,\text{track}}$ , which is taken from an uniform distribution between 0.15 GeV and 1 GeV. Tracks are always either observed or not at the true momentum. No smearing is added to the observed momentum.

Afterwards the tracks are looped over for  $j_T$  calculation. For observed tracks we calculate  $j_T$  with respect to both the true jet axis and the observed jet. 2D Response matrix is filled with

$$(j_T^{\text{obs}}, p_{T,\text{jet}}^{\text{obs}}, j_T^{\text{true}}, p_{T,\text{jet}}^{\text{true}}) \quad (65)$$

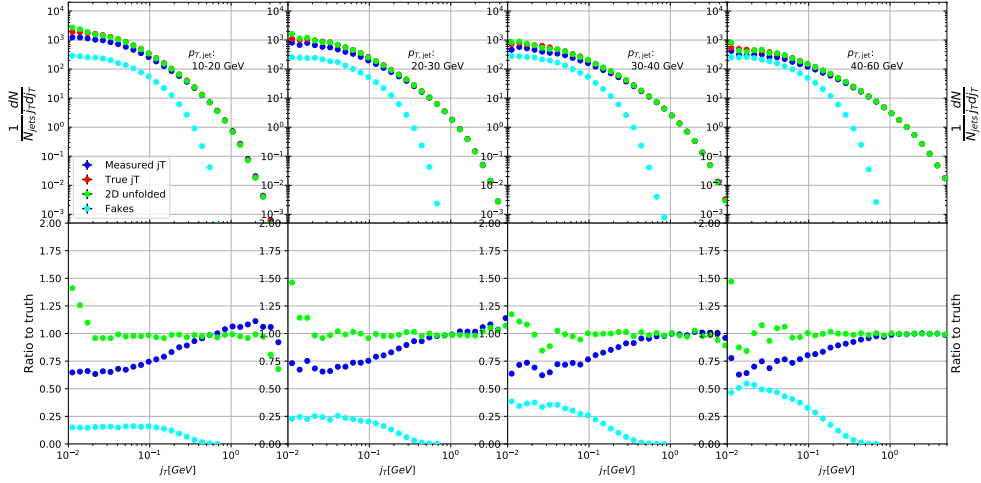


Figure 41: Results from unfolding in Toy Monte Carlo

1811 In practice this is done with a set of 3D histograms, where  $p_{T,\text{jet},\text{true}}$  determines  
 1812 the histogram index and the remaining three values the bin in the 3D histogram.

1813 After creating the response matrices, an identical procedure is carried out to  
 1814 the create testing data. Now instead of filling response matrices, 2D histograms  
 1815 are filled with  $(j_T^{\text{obs}}, p_{T,\text{jet}}^{\text{obs}})$  and  $(j_T^{\text{true}}, p_{T,\text{jet}}^{\text{true}})$

1816 The observed distributions are unfolded using the 2D Bayesian (iterative) algo-  
 1817 rithm of RooUnfold. Results are shown in Figure 41. Aside from some discrepancy  
 1818 at very low  $j_T$  the true distribution is retrieved well.

#### 1819 4.3.3 Pythia Response matrices

1820 A PYTHIA 6 simulation was carried out to determine the response matrices. The  
 1821 simulation used the Perugia 2011 [274] tune with  $\sqrt{s_{NN}}=5.02$  TeV. The detector  
 1822 response of the particle level tracks was simulated using GEANT3 [275, 276].

1823 Response matrices are filled through correlation between MC detector and  
 1824 particle level jets and tracks. When creating the response matrices detector level  
 1825 tracks in each event are first analysed using the same procedure as for data, but  
 1826 their  $j_T$  values are stored in an array. This is only done for tracks that are closer  
 1827 than the cone size,  $R$ , to a jet. Thus most tracks in the event will not have their  
 1828  $j_T$  values calculated. The analysis then moves to particle level (MC) tracks. There  
 1829 are analysed similarly, but for each track the code checks whether a corresponding  
 1830 detector level track existed and if that track had a  $j_T$  value. Finally the code  
 1831 checks for detector level tracks that don't have corresponding particle level track  
 1832 with a  $j_T$  value.

1833 There are several possibilities that have to be taken into account:

- We find a corresponding track with a  $j_T$  value. Response matrix is filled normally with  $(j_T^{\text{obs}}, p_{T,\text{jet}}^{\text{obs}}, j_T^{\text{true}}, p_{T,\text{jet}}^{\text{true}})$
- We don't find a corresponding track. Record  $(j_T^{\text{true}}, p_{T,\text{jet}}^{\text{true}})$  as a miss
- We find a corresponding track, but it didn't have  $j_T$  value. Most likely because it was not part of a jet in the detector level set. Similary record  $(j_T^{\text{true}}, p_{T,\text{jet}}^{\text{true}})$  as a miss
- For detector level tracks that have no correspondence in particle level set the code records  $(j_T^{\text{obs}}, p_{T,\text{jet}}^{\text{obs}})$  as a fake

In the analysis code the response matrix is made of an array of 3 dimensional histograms, with  $(j_T^{\text{obs}}, p_{T,\text{jet}}^{\text{obs}}, j_T^{\text{true}})$  as axes. The histogram index gives the  $p_{T,\text{jet}}^{\text{true}}$  value. The ranges in the response matrices of both  $j_T$  and  $p_{T,\text{jet}}$  match the ranges used for the end results. For  $j_T$  the range is between 0.01 GeV and 20 GeV and  $p_{T,\text{jet}}$  between 5 GeV and 500 GeV. The ranges are the same in detector and particle level.

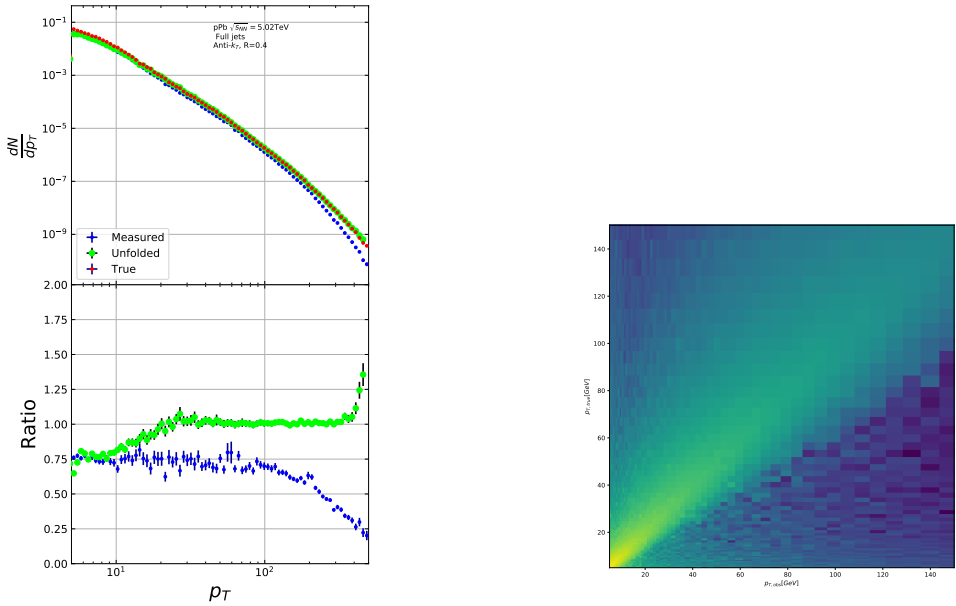
As a primary method unfolding is performed with an iterative (bayesian) algorithm using the RooUnfold [272] package. The number of iterations used is 4. As a default the true  $j_T$  distribution from the PYTHIA simulation is used as the prior.

#### 4.3.4 Unfolding closure test

The PYTHIA set is divided into 2 halves. First is used to fill the response matrices, as well as record missed and fake tracks. Second half is used to test the effectiveness of the unfolding method. Jet  $p_T$  distributions are shown in Figure 42a and response matrix are shown in Figure 42b. For the range where this analysis is performed,  $40 \text{ GeV} < p_{T,\text{jet}} < 150 \text{ GeV}$ , the  $p_{T,\text{jet}}$  distribution is recovered well. At low  $p_{T,\text{jet}}$  the true distribution can't be recovered. The primary reason is that jet with  $p_{T,\text{obs}} < 5 \text{ GeV}$  are not considered, although  $p_{T,\text{true}}$  would have been above 5 GeV. Thus these are missing from the response matrix and their contribution can't be unfolded. At high  $p_{T,\text{jet}}$  the situation is opposite. Jets with  $p_{T,\text{true}} > 500 \text{ GeV}$  are lost due to histogram limits. Thus jets just below this limit are overrepresented in the response matrix for  $p_{T,\text{obs}} \approx 500 \text{ GeV}$ .

Response matrices within single jet  $p_T$  bins are shown in Figure 43. Results from the closure test are shown in Figure 44. In the lowest jet  $p_T$  bins unfolding fails to recover the true distribution. The lowest jet  $p_T$  bins are dominated by combinatorial jets and thus the true detector response is likely not retrieved.

Above  $30 \text{ GeV} < p_{T,\text{jet}} < 40 \text{ GeV}$  the distribution is recovered well in the mid  $j_T$  region. At  $j_T < 0.1 \text{ GeV}$  there is clear discrepancy and hence the final results are shown only for  $j_T > 0.1 \text{ GeV}$ . Additionally there is some discrepancy at very high  $j_T$ . This is taken into account in the unfolding systematics.



(a) Unfolded jet  $p_T$  distribution in PYTHIA closure test      (b) Jet  $p_T$  response matrix from unfolding closure test

Figure 42: Jet  $p_T$  in unfolding closure test

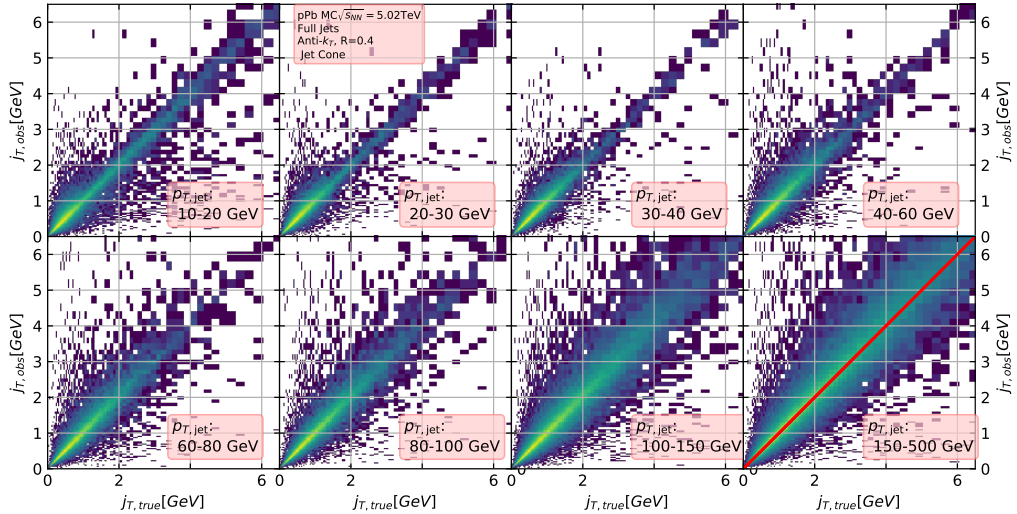


Figure 43:  $j_T$  Response matrices in individual  $p_{T,jet}$  bins

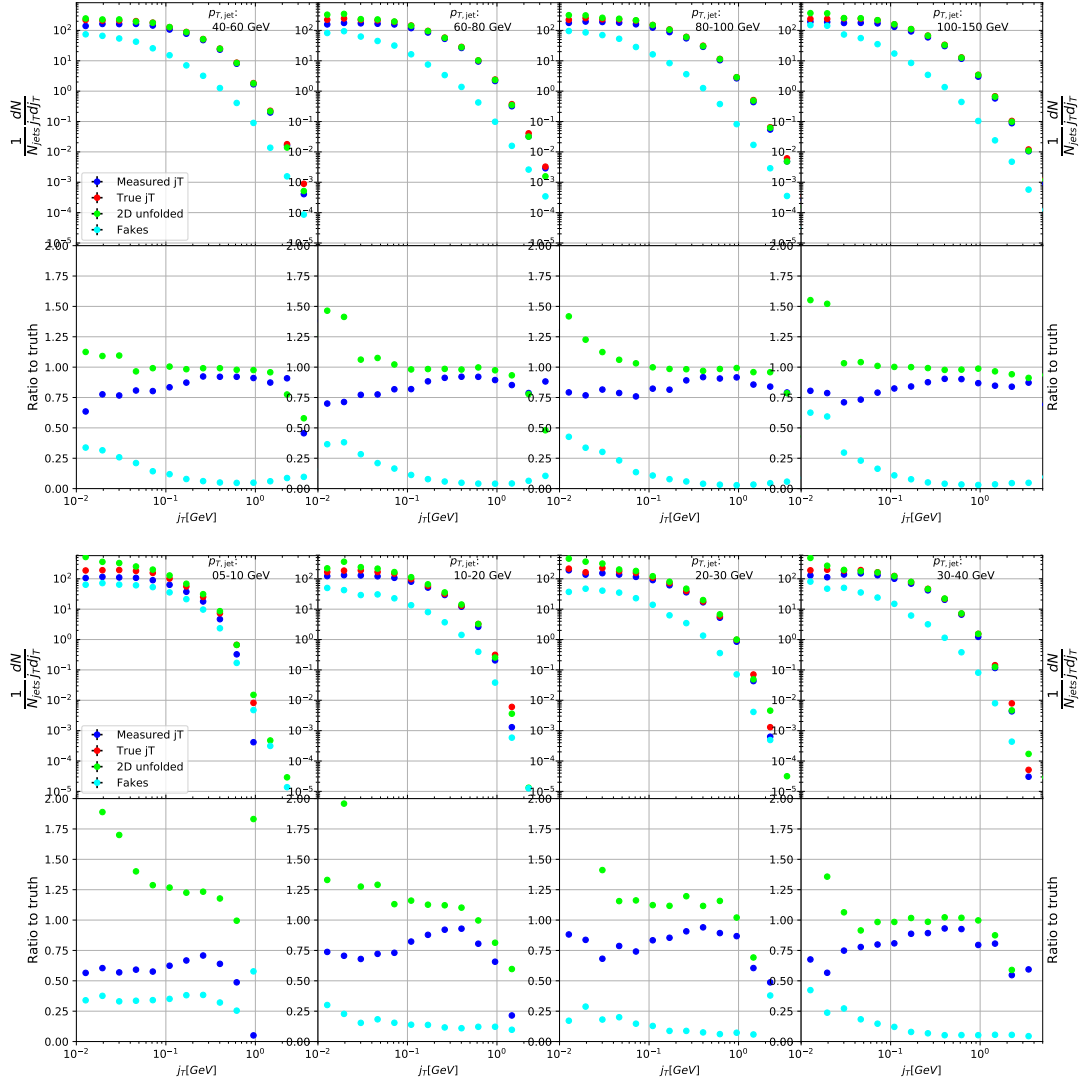


Figure 44: Pythia closure test results. Fake tracks include also tracks that do exist in the true dataset, but for one reason or another were not given  $j_T$  values.  $j_T$  is only calculated for tracks that are associated with jets

## 1871 4.4 Background

1872 When calculating  $j_T$  distributions for jet constituents there is a contribution from  
 1873 the underlying event (UE), i.e. tracks that just happen to be close to the jet axis.  
 1874 To find the signal coming from the actual jet we need to subtract the background  
 1875 (UE) contribution. On a jet-by-jet basis this is difficult to achieve reliably, so  
 1876 one must estimate the background contribution in the inclusive distribution. A  
 1877 schematic view of the background contribution is shown in Figure 45.

1878 We have two methods for background estimation. In the first we look at the  
 1879 direction perpendicular to the jet. This is assumed to be the region least likely to  
 1880 contain jet contributions. In the second method we randomly assign the tracks of  
 1881 event new  $\phi$  and  $\eta$  values. The result is thus guaranteed to be uncorrelated.

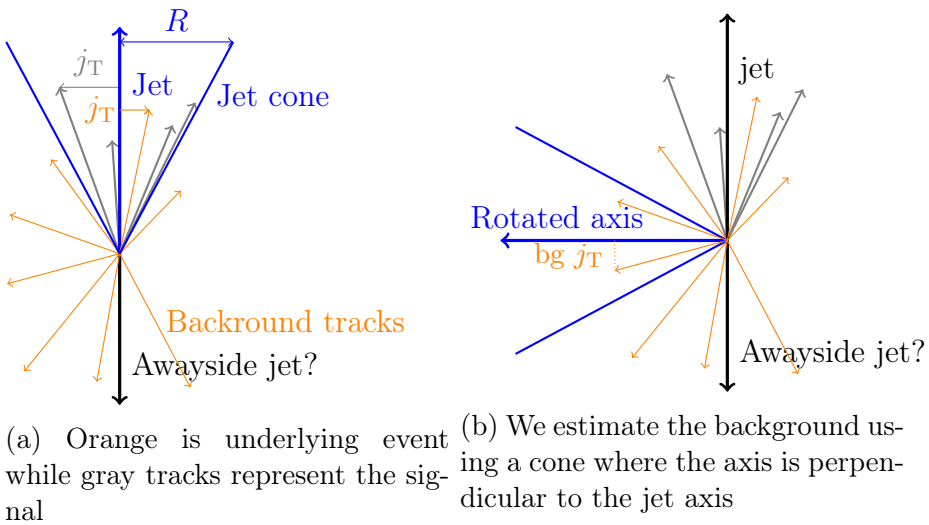


Figure 45: Background estimation

### 1882 4.4.1 Perpendicular cone background

1883 As a primary method to estimate the background we look at regions of the detector  
 1884 where there are no tracks from jets, but only uncorrelated tracks from the under-  
 1885 lying event. The underlying event is thus estimated by looking at an imaginary  
 1886 jet cone perpendicular to the observed jet axis ( $\frac{\pi}{2}$  Rotation in  $\phi$ ).

1887 After calculating the  $j_T$  values for tracks in the jet, we rotate the jet axis by  $\frac{\pi}{2}$   
 1888 in positive  $\phi$  direction. We check that there are no other jets closer than  $2R$  to the  
 1889 rotated axis. Otherwise background calculation is skipped for this jet. Probability  
 1890 of this happening is 1-2% depending on the jet  $p_T$  bin.

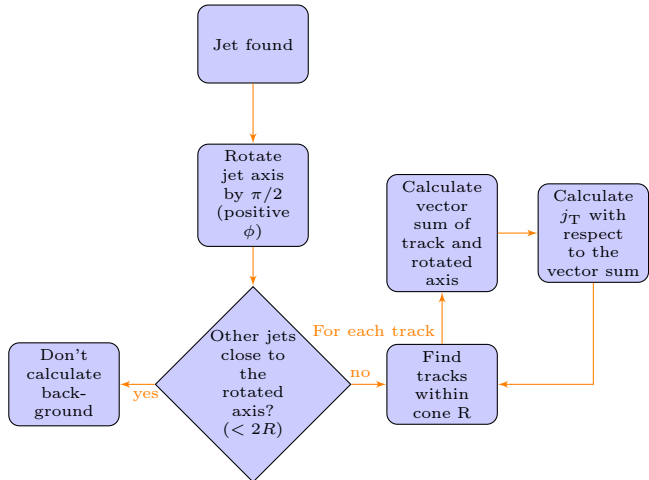


Figure 46: Flowchart representation of the perpendicular cone background procedure

1891 If we don't find other jets in the vicinity we move on to estimate the background.  
 1892 We find all tracks within a cone of radius  $R$  around the rotated axis and calculate  
 1893  $j_T$  of these tracks with respect to the rotated axis.

1894 This background procedure is a part of the reason for using charged tracks  
 1895 inside a fixed size cone, instead of jet constituents. To be representative of the  
 1896 actual underlying event contribution the size and shape of the background estima-  
 1897 tion region should match the area where  $j_T$  is calculated. The irregular shape of  
 1898 a jet would be hard to take into account when calculating background. Thus the  
 1899 regions are made to match by considering fixed size cones for  $j_T$ .

1900 One additional consideration is the issue of auto-correlations as the jet axis is  
 1901 simply a vector sum of all its constituents. Thus having an additional track in the  
 1902 jet from the underlying event moves the jet axis towards this track. Since the axis  
 1903 is now closer to the track, it has a smaller  $j_T$  value. Assuming a 1 GeV background  
 1904 track at the edge of a  $R = 0.4$  cone the  $j_T$  value would be 0.4 GeV. If this is added  
 1905 to a 5 GeV jet, the  $j_T$  value becomes 0.33 GeV after the jet axis moves. In a 50 GeV  
 1906 jet it would be 0.39 GeV. This is a region where the inclusive  $j_T$  distribution is  
 1907 dominated by background. The distribution is also steeply falling. Overestimating  
 1908 the background can lead to a situation where the background estimation exceeds  
 1909 the inclusive distribution.

1910 To take this effect into account we can't use a fixed axis for background, but  
 1911 it has to behave like a jet would when additional tracks are added. Thus before  
 1912 calculating  $j_T$  values we make a vector sum of the track and the axis used for back-  
 1913 ground, which is either the perpendicular cone axis or the random axis depending  
 1914 on the background method. In each case the momentum of this background axis

1915 is assumed to be the same as the jet which initiated the background estimation.

1916 In pPb data there is on average about one underlying event track in a  $R = 0.4$   
1917 cone. If there would be more, one should consider taking the vector sum of all  
1918 tracks inside the cone. As there is usually only one track and if there are more it's  
1919 unlikely that more than one has high momentum, taking the vector sum track-by-  
1920 track should be enough.

#### 1921 4.4.2 Random background

1922 In the random background method we look at all tracks in the event, except for  
1923 tracks close to jets found by the jet algorithm. We randomly assign new  $\eta$  and  $\phi$   
1924 values to all tracks using uniform distributions with  $|\eta| < 1.0$ .  $p_T$  values are kept  
1925 the same. To increase statistics there is a possibility to create a number of random  
1926 tracks for each actual track. In the analysis we do this 10 times for each track.  
1927 Again the track  $p_T$  value is kept the same.

1928 We create a random jet cone from uniform  $\eta$  and  $\phi$  distributions. Here  $|\eta| <$   
1929 0.25. Now we calculate  $j_T$  of the random tracks with respect to the random cone  
1930 axis. As in the perpendicular cone method auto-correlations are added before  
1931 calculating  $j_T$ .

1932 Comparison between perpendicular cone and random background in Figure 47.  
1933 The advantage of the random background method is that the procedure can be  
1934 repeated several times for each event, which allows producing additional statistics.  
1935 However, it seems that, especially in the highest  $p_{T,jet}$  bins there is some jet con-  
1936 tribution left at the high end. Naturally there is no correlation between the tracks  
1937 and the background axis, but if some high momentum tracks originating from jets  
1938 were not subtracted and happen to hit the edge of the background cone, they can  
1939 increase the high  $j_T$  yield in the background estimation.

1940 We observe that the results from perpendicular cone background show no ob-  
1941 servable change between  $p_{T,jet}$  bins. It is a good indication that the background is  
1942 actually dominated by the underlying event over the entire  $j_T$  region.

1943 Thus as a primary method of background estimation the perpendicular cone  
1944 method is used. The random background method is used to estimate systematic  
1945 contributions by comparing the final results obtained with this method to the  
1946 results obtained from the perpendicular cone method.

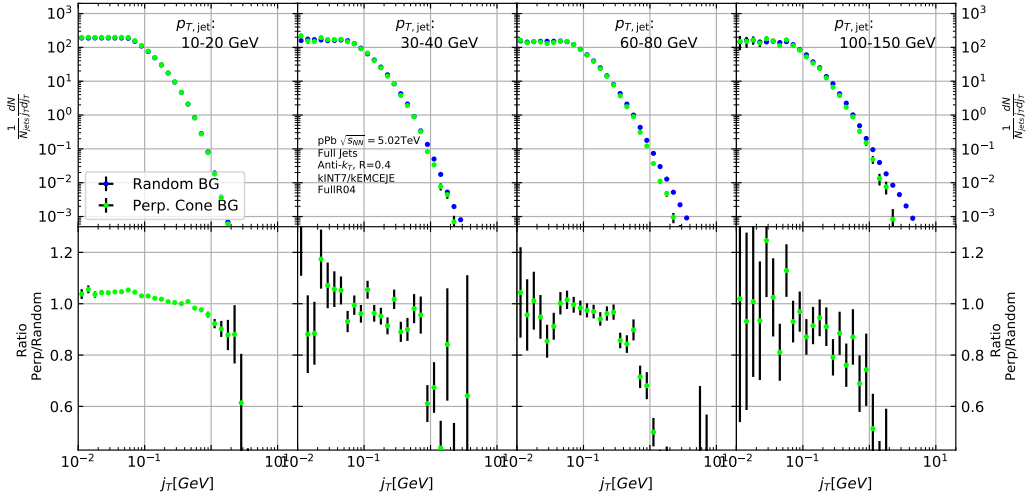


Figure 47:  $j_T$  background with two different methods

## 1947 4.5 Fitting

1948 After unfolding and background subtraction the resulting signal distributions are  
 1949 fitted with a 2 component function shown in Eq. 66. Gaussian distribution is used  
 1950 for low  $j_T$  and an inverse gamma function is used for high  $j_T$ . The Gaussian is  
 1951 taken to have the center at  $j_T = 0$ . In total this gives 5 parameters. The fitting  
 1952 procedure was inspired by the dihadron  $j_T$  analysis by ALICE [277]. The complete  
 1953 fitting function is

$$\frac{1}{N_{\text{jets}} j_T \text{d}j_T} \frac{\text{d}N}{\text{d}j_T} = \frac{B_2}{B_1 \sqrt{2\pi}} e^{-\frac{j_T^2}{2B_1^2}} + \frac{B_3 B_5^{B_4}}{\Gamma(B_4)} e^{-\frac{B_5}{j_T^{B_4+1}}} \quad (66)$$

1954 To achieve stable results the fitting is performed in two steps. First both  
 1955 components are fitted separately. Gaussian component is fitted to the low end of  
 1956  $j_T$ . Inverse gamma component is fitted to  $j_T$  above 1 GeV/c. After getting the  
 1957 results from the individual fits they are combined into a single function with initial  
 1958 values from the individual results and an additional fit is performed.

1959 After getting the fit function  $\sqrt{\langle j_T^2 \rangle}$  (RMS) and yield values are extracted  
 1960 separately from each component. The narrow component RMS is

$$\sqrt{\langle j_T^2 \rangle} = \sqrt{2} B_1, \quad (67)$$

1961 and the wide component RMS value is calculated as

$$\sqrt{\langle j_T^2 \rangle} = \frac{B_5}{\sqrt{(B_4 - 2)(B_4 - 3)}}, \quad (68)$$

<sup>1962</sup> where it is required that  $B_4 > 3$ .

<sup>1963</sup> The statistical errors can be calculated with the general error propagation  
<sup>1964</sup> formulas. As a result one gets errors for the narrow component RMS

$$\delta \sqrt{\langle j_T^2 \rangle} = \sqrt{2} \delta B_1 \quad (69)$$

<sup>1965</sup> and for the wide component RMS

$$\delta \sqrt{\langle j_T^2 \rangle} = \sqrt{\left( \frac{(5 - 2B_4) B_5 \delta B_4}{(2(B_4 - 2)(B_4 - 3))^{\frac{3}{2}}} \right)^2 + \left( \frac{\delta B_5}{\sqrt{(B_4 - 2)(B_4 - 3)}} \right)^2} \quad (70)$$

## **5 Systematic errors**

The main systematic uncertainties in this analysis come from the background estimation, the unfolding procedure and uncertainty in the tracking efficiency. The systematics in background estimation were studied using an alternative method to extract the background, the random background method and the uncertainty in tracking was studied by varying tracking efficiencies in a PYTHIA simulation.

The systematic uncertainty that arises from the unfolding procedure is estimated by performing the unfolding with two separate methods. Data corrected by the iterative unfolding method are used as the results and the SVD unfolding method is employed to estimate the uncertainty. In a PYTHIA closure test the true distribution was in general found to be between the unfolded distributions from the iterative and SVD method. The difference between the methods when unfolding data should give a reasonable estimate of the unfolding uncertainty. The resulting uncertainty is below 8% for both wide and narrow component RMS.

### **5.1 Background**

The uncertainty coming from background calculation is estimated by subtracting the background separately for the perpendicular cone and random background methods. Comparisons of the resulting signal distributions are shown in Figure 48.

Fits are then performed on both perpendicular cone and random background signals. Difference between them is taken as the systematic uncertainty. The fits for individual bins from the random background method are shown in Figure 49. Resulting differences between the methods for different components are shown in Figure 50. The dotted lines are put at  $\pm 5\%$  for the narrow component and at  $\pm 8\%$  for the wide component. These are taken as systematic estimates for the entire  $p_{T,jet}$  range.

### **5.2 Unfolding**

Unfolding is the second major source of systematic uncertainty. To estimate the uncertainty related to the unfolding procedure several checks are performed. The main systematic uncertainty estimation comes from comparing results performed using both SVD and Bayesian unfolding. Difference between the methods is taken as the systematic uncertainty. Since SVD unfolding does not have a two dimensional option, the unfolding is done bin by bin.

As in the background systematic estimation, fits are performed for both cases separately. Resulting differences between the methods for different components are shown in Figure 51. The dotted lines are at  $\pm 8\%$  for both components. These are taken to be the systematic uncertainty related to unfolding.

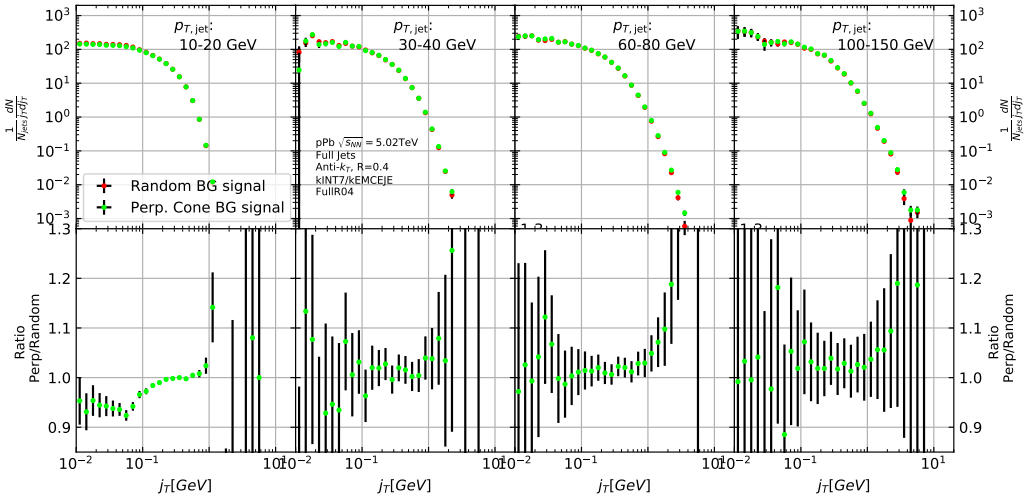


Figure 48: Comparison of the effect of background method on  $j_T$  signal.

Several other systematic checks were performed with the Bayesian unfolding procedure. They are described in the following sections. As these are small compared to the main uncertainty they are not included separately.

### 5.2.1 Effect of number of iterations

The iterative unfolding algorithm permits the change of number of iterations. The unfolding procedure was carried out using different numbers of iterations. The results from these different cases are shown in Figure 52. The results are compared to the default unfolding algorithm with 4 iterations. The difference in results between the different cases is mostly less than 2.5%.

### 5.2.2 Effect of different prior

The iterative algorithm requires a prior estimate of the shape of the distribution. As a default prior the truth (particle level) distribution is used. To test the effect of changing the prior we instead use the unfolded  $j_T$  distribution as prior. The results are compared to the unfolding algorithm with the default prior. This is shown in Figure 53. The difference in results between the different cases is mostly less than 2.5%.

### 5.2.3 Effect of $p_T$ truncation

As an additional check the unfolding is carried out with different  $p_{T,jet}$  truncation values. By default the full range of  $p_{T,jet} > 5\text{GeV}$  is used. We test the unfolding

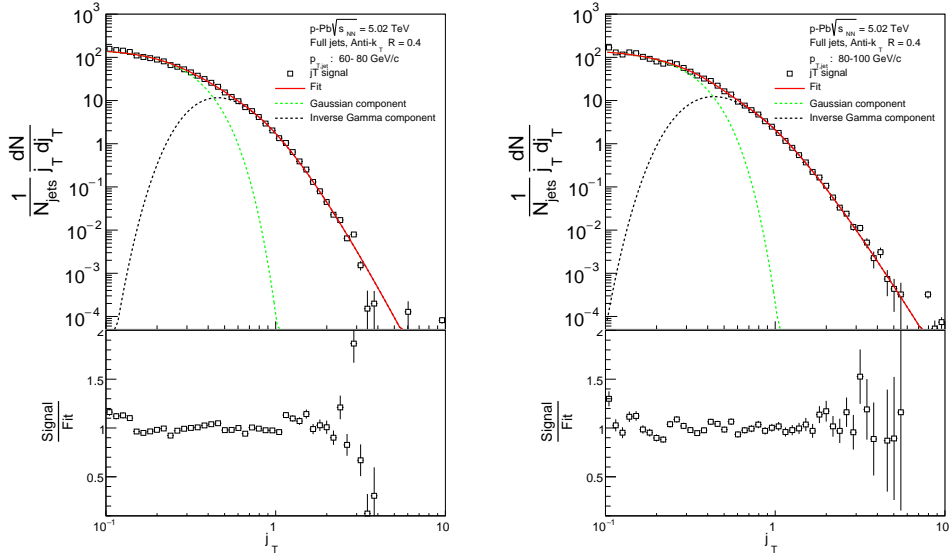


Figure 49:  $j_T$  signal with random background subtraction fits in different jet  $p_T$  bins

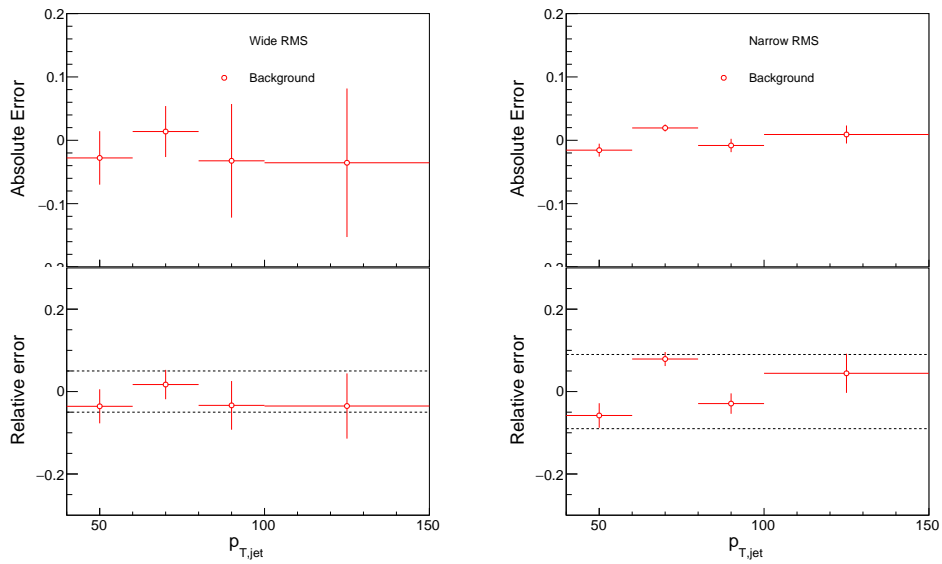


Figure 50: Differences between perpendicular cone and random background subtraction in the resulting RMS values.

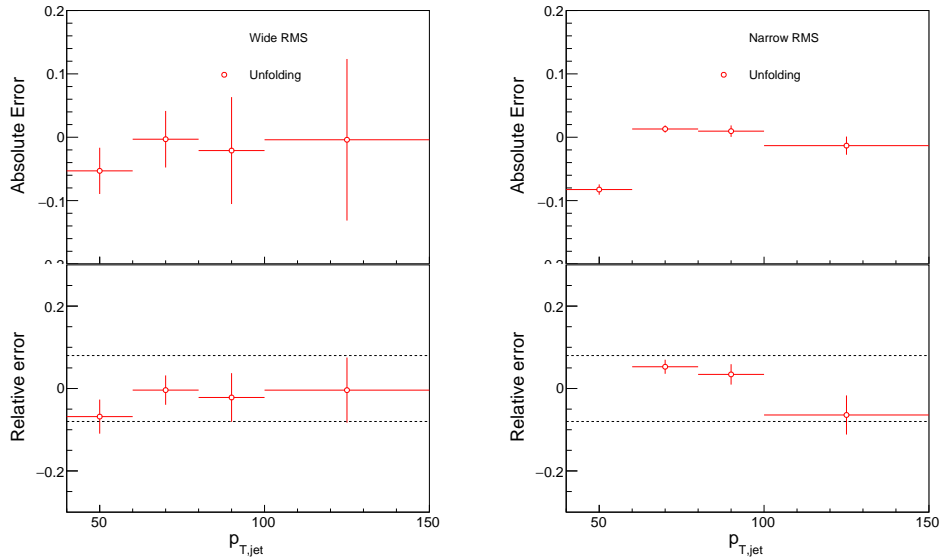


Figure 51: Differences between Bayesian and SVD unfolding in the resulting RMS values

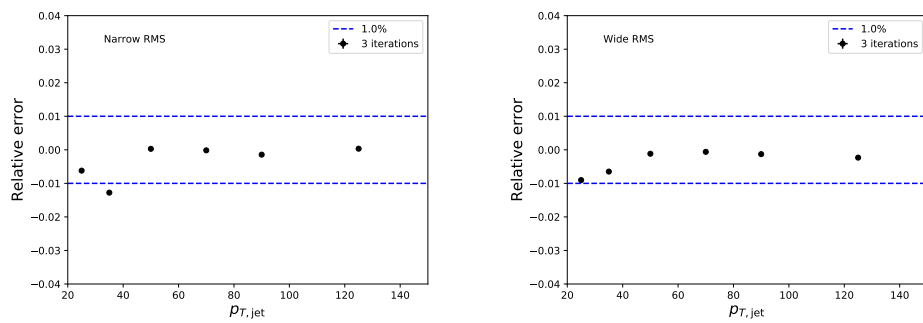


Figure 52: Unfolding with different number of iterations

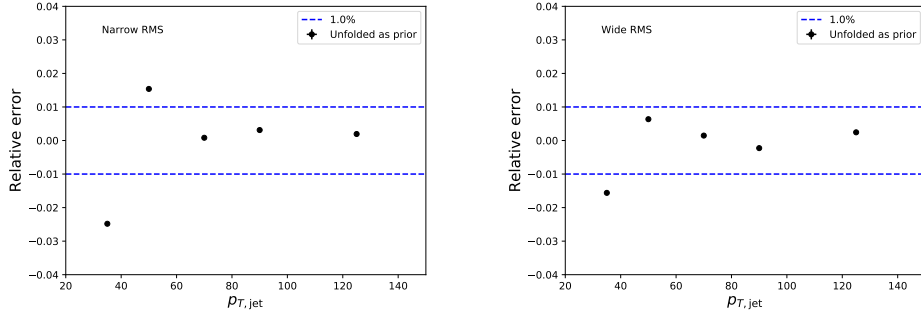


Figure 53: Effect of changing prior from true distribution in PYTHIA to the unfolded distribution.

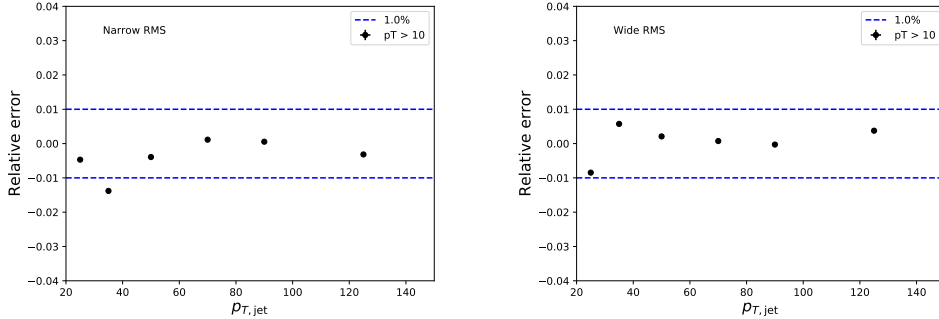


Figure 54: Effect of changing minimum jet  $p_T$  used in unfolding from 5 to 10 GeV

2021 by only using the response matrix for  $p_{T,\text{jet}} > 10 \text{ GeV}$ . The results of this test are  
2022 shown in Figure 54. The effects are strongest in the lower  $p_{T,\text{jet}}$  bins. Also in this  
2023 case the difference is less than 2.5 % in all  $p_{T,\text{jet}}$  bins.

### 2024 5.3 Tracking

2025 Systematic effects originating from uncertainty in the tracking efficiency are es-  
2026 timated through a PYTHIA simulation, where an artificial inefficiency of 3% is  
2027 introduced i.e. 3 % of tracks are randomly removed from each event. The effect  
2028 of this artificial inefficiency is shown in Figure 55. The systematic uncertainties  
2029 assigned to tracking efficiency are 4% for the narrow component and 5% for the  
2030 wide component.

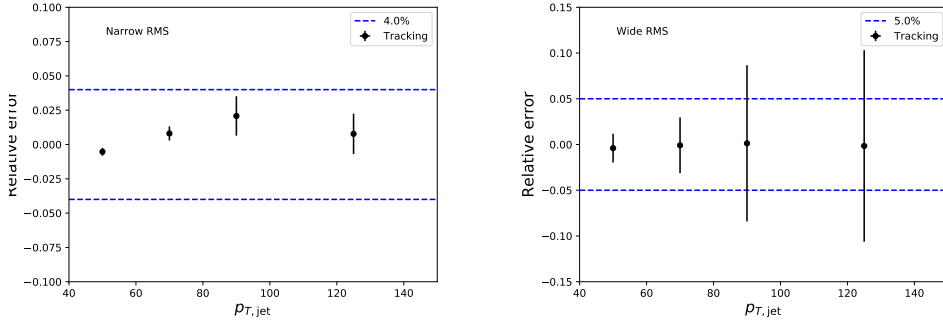


Figure 55: Relative systematic uncertainties resulting from tracking efficiency uncertainty.

## 2031 5.4 EMCAL clusters

2032 The analysis uses EMCAL clusters only in the reconstruction of jets. Thus the only  
 2033 way uncertainty in EMCAL performance can affect the results is through modifica-  
 2034 tion of jet momentum or axis.

2035 Uncertainty related to the EMCAL energy scale was estimated by scaling cluster  
 2036 energies up and down by 2 % in a PYTHIA particle level simulation. Similarly  
 2037 the jet momentum was scaled by  $\pm 2\%$  when determining the jet  $p_T$  bin. In this  
 2038 analysis EMCAL is used only in jet reconstruction, not for calculating  $j_T$ . The only  
 2039 ways EMCAL uncertainty can affect the analysis are changes in jet energy and jet  
 2040 axis. Jet axis shouldn't significantly change, so the main contribution should be  
 2041 changes in jet  $p_T$  bin.

2042 The resulting differences in the inclusive  $j_T$  distributions are shown in Fig-  
 2043 ure 56. Qualitatively the effect of scaling cluster energies is the same as scaling  
 2044 the jet energies.

2045 Like in the previous cases fits are performed for the unscaled case and for cases  
 2046 with  $\pm 2\%$  scaling. The resulting systematic uncertainties are shown in Figure 57.  
 2047 The uncertainty is taken to be 1% for both components.

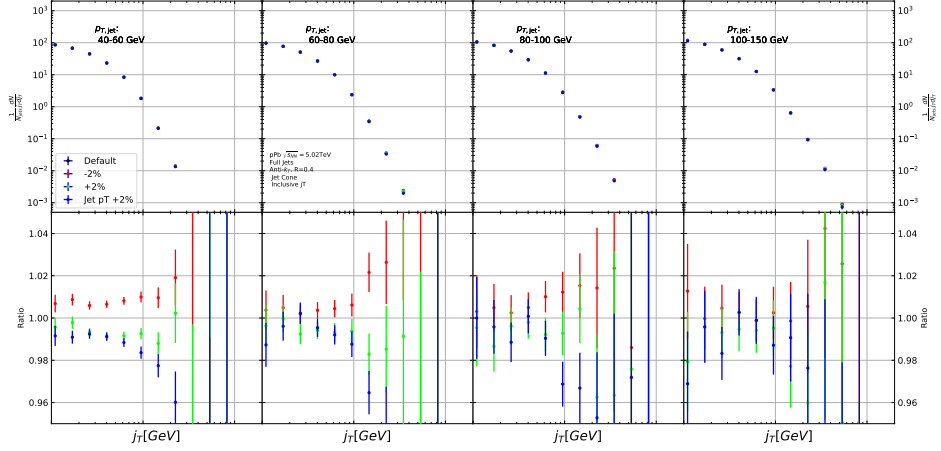


Figure 56: Results from PYTHIA simulations with Cluster energies scaled up and down by 2 %. Additionally jet momenta were scaled by 2 % when determining the jet  $p_T$  bin.

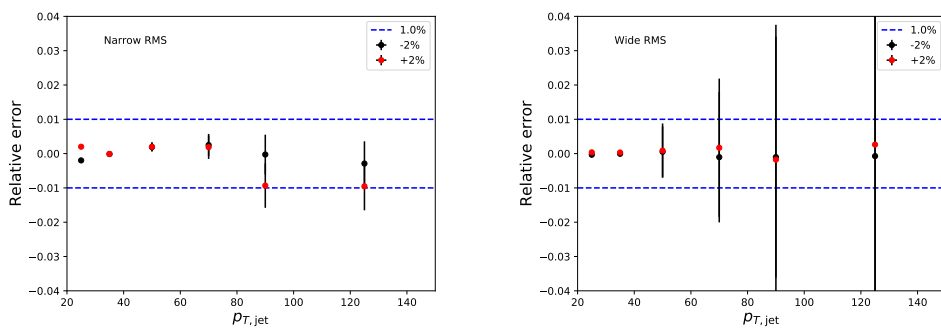


Figure 57: Relative systematic uncertainties resulting from cluster energy uncertainty.

## **2048 5.5 Summary of systematic uncertainties**

**2049** The different source of the systematic uncertainty are considered as uncorrelated  
**2050** and the values of each source are summed in quadrature. Resulting systematic  
**2051** uncertainties are shown in Table 4. The different source of the systematic un-  
**2052** certainty are considered to be uncorrelated and are thus combined bin-by-bin in  
**2053** quadrature to get the total systematic uncertainties. The resulting uncertainty  
**2054** is approximately 10 % for the wide component RMS and 13 % for the narrow  
**2055** component RMS.

Table 4: Summary of systematic uncertainties

Systematic	Wide RMS	Narrow RMS
Background	5 %	9 %
Unfolding	8 %	8 %
Tracking	4 %	5 %
EMCal	1 %	1 %
Total	10 %	13%

## 6 Results

In this section I present the final results for  $j_T$  signals. After unfolding and subtracting the background contribution we get the final  $j_T$  distributions. Figure 58 shows  $j_T$  distributions for two different  $p_{T,jet}$  bins with  $60 \text{ GeV} < p_{T,jet} < 80 \text{ GeV}$  and  $100 \text{ GeV} < p_{T,jet} < 150 \text{ GeV}$ . The distributions get wider with increasing  $p_{T,jet}$ . In part this is explained by kinematics; In a jet cone the cone size sets limits on the possible  $j_T$  values. For a given  $p_{T,track}$  the maximum  $j_T$  value is approximately

$$j_{T\max} \approx R \cdot p_{T,track}, \quad (71)$$

using the small angle approximation.

We fit the distribution using the two component fit function presented in Section 4.5. These are also shown in Figure 58. Fitting a Gaussian alone to the entire  $j_T$  distribution will produce a similar result as the Gaussian component in the two component fit. Thus the gaussian fit alone can't describe the full jet  $j_T$  distribution.

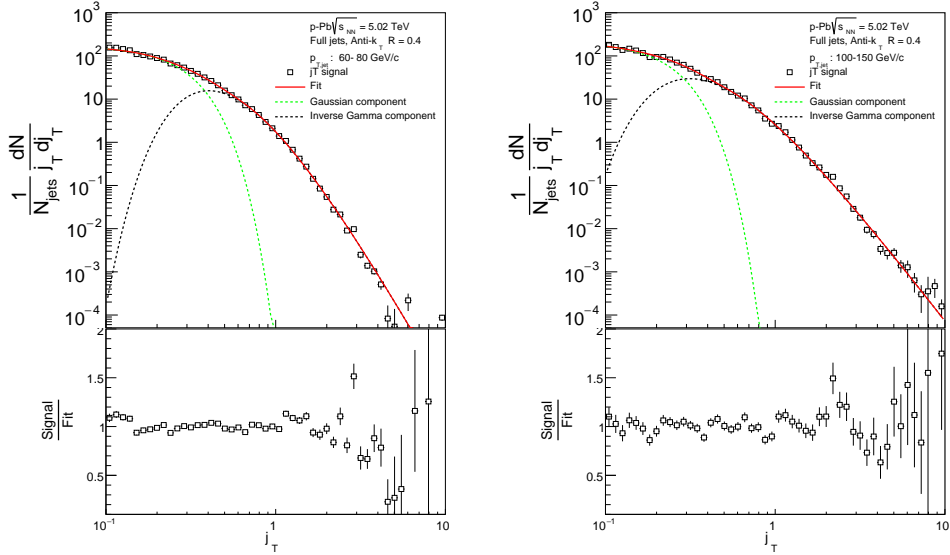


Figure 58:  $j_T$  signal distributions fitted with the two component model are shown in different jet  $p_T$  bins.

To characterise the widening of the  $j_T$  distribution we can then extract the RMS, i.e.  $\sqrt{\langle j_T^2 \rangle}$ , values of the fits. Resulting RMS values with systematic errors are shown separately for the two components in Figure 59. Here it is seen that the width of the narrow component shows only a weak dependence on the transverse

momentum of the jet,  $p_{T,jet}$ . The RMS value of the wide component on the other hand increases with increasing  $p_{T,jet}$ .

The RMS values for both components are compared to PYTHIA and Herwig simulations as shown in Figure 60. All the PYTHIA models reproduce the data well, both the wide and narrow component. For the narrow component Herwig gives RMS values comparable to the data. On the other hand, Herwig produces larger wide component  $\sqrt{\langle j_T^2 \rangle}$  values than data and PYTHIA, and this difference seems to get larger with increasing  $p_{T,jet}$ .

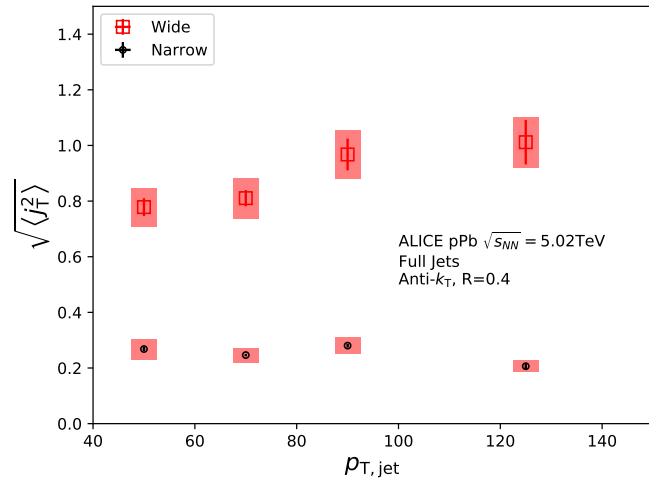


Figure 59: RMS values extracted from the fits are shown for the Gaussian (narrow) and inverse gamma (wide) components.

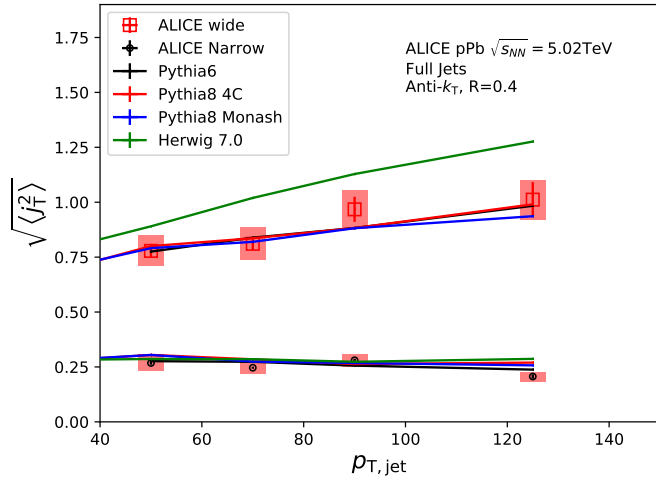


Figure 60: RMS values extracted from the fits are compared to Monte Carlo models. PYTHIA reproduces the data well for both the narrow and wide components. Herwig produces wider distributions.

## 2081 6.1 High multiplicity events

2082 The analysis was repeated taking only events with high multiplicity. Three dif-  
 2083 ferent multiplicity percentile cuts were used; 10 %, 1 % and 0.1 %. The centrality  
 2084 estimations were given by V0A. Resulting  $j_T$  signal distributions are shown in Fig-  
 2085 ure 61. From the figure one can observe no modification within the errors when  
 2086 tighter multiplicity cuts are introduced.

2087 As described in Section 1.5 no conclusive evidence of jet modification in  
 2088 p–Pb collisions has been observed. However, all previous observations have been  
 2089 done for minimum bias events. Most observables are based on measuring yield  
 2090 instead of jet shape and are thus sensitive to biases in the centrality selection.  
 2091 No previous jet shape measurements have been performed in high multiplicity  
 2092 p–Pb events, where collective motion was observed.

2093 As the statistics are limited in the high multiplicity runs, it was hard to achieve  
 2094 stable fits to the distributions. Thus the RMS values are not shown.

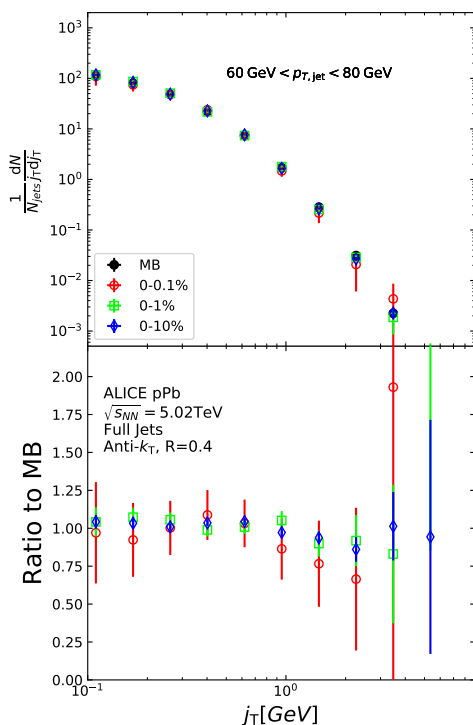


Figure 61:  $j_T$  distributions are shown for various multiplicity bins in p–Pb collisions.

## 2095 7 Discussion

### 2096 7.1 Comparing dihadron and jet $j_T$ results

2097 The jet fragmentation transverse momentum  $j_T$  has been studied previously at  
2098 ALICE using dihadron correlations [277]. The study took the leading hadron in  
2099 each event and calculated  $j_T$  for any near-side tracks with respect to the leading  
2100 hadron. Thus there is no kinematical limit to  $j_T$  from the jet cone. In the analysis  
2101 the background shape is estimated using pairs with large  $\Delta\eta$ . The normalisation of  
2102 the background is done when fitting the  $j_T$  distribution. The inclusive distribution  
2103 is fitted with a three component function, where one of the components is the  
2104 background contribution. After subtracting the background, what remains is the  
2105 signal distribution characterised by the two components. The resulting signal  
2106 distribution from the analysis is shown in Figure 62. The analysis was the first to  
2107 introduce this factorisation of  $j_T$  into components.

2108 To constrain the effects from kinematical differences between  $p_{T,\text{trigger}}$  bins the  
2109 analysis used bins of the fragmentation variable  $x_{\parallel}$ , which is the projection of the  
2110 associated particle momentum to the trigger particle normalised by the trigger  
2111 particle momentum

$$x_{\parallel} = \frac{\vec{p}_t \cdot \vec{p}_a}{\vec{p}_t^2}. \quad (72)$$

2112 The RMS results from the fitting in both pp and p–Pb collisions are shown in  
2113 Figure 63. Qualitatively the results are similar to jet  $j_T$  results. The RMS value  
2114 of the wide component has an increasing trend with respect to  $p_{T,t}/p_{T,jet}$ , while  
2115 the RMS value of the narrow component stays constant. Both components are  
2116 well described by PYTHIA simulations. As seen in the figures there is no difference  
2117 between minimum bias pp and p–Pb results in the dihadron analysis.

2118 Comparison between RMS values in dihadron  $j_T$  [277] and jet  $j_T$  is shown in  
2119 Figure 64. The dihadron trigger  $p_T$  bins are converted to jet  $p_T$  bins and vice versa.  
2120 Bin-by-bin comparison is still not possible, but general features can be identified.

2121 The trends are similar in dihadron and jet  $j_T$  results. Wide component RMS  
2122 values tend to increase with increasing  $p_{T,\text{trigger}}/p_{T,jet}$ . For  $x_{\parallel} < 0.4$  Narrow com-  
2123 ponent RMS increases slightly at low  $p_{T,\text{trigger}}$  in dihadron analysis. This trend  
2124 changes between  $x_{\parallel}$  bins; In larger  $x_{\parallel}$  bins the narrow component RMS is closer  
2125 to constant as is the case for jet  $j_T$ .

2126 The most striking difference is that dihadron  $j_T$  gives wider distributions with  
2127 larger RMS values. There are several possible causes for this difference. First, in  
2128 jet analysis the cone size limits width and thus the RMS values. The effect of this  
2129 limitation can be studied by changing the cone size as is described in Section 7.1.1.

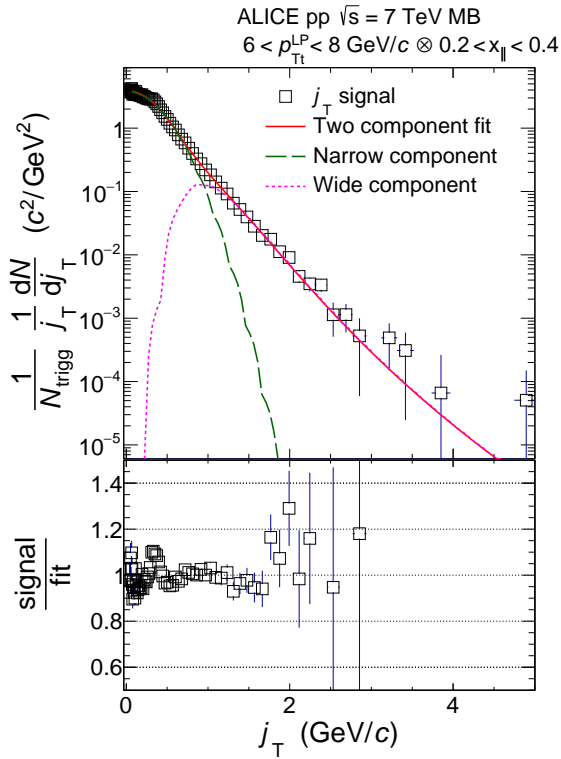


Figure 62: Measured  $j_T$  signal distribution using dihadron correlations is shown for  $6 < p_{Tt} < 8$  and  $0.2 < x_{||} < 0.4$ . The distribution is fitted with the same two component model used in this thesis.

2130 Second, the leading track is an imperfect estimate of the jet/original parton.  
 2131 Because the leading track in general is at an angle compared to the jet axis, the  
 2132 resulting  $j_T$  values are different. In practice the jet axis found by the jet finding  
 2133 algorithm tends to minimize the average  $j_T$  of jet constituents. Thus the yield  
 2134 at high  $j_T$  is limited and the RMS values are smaller. The effect of having the  
 2135 leading hadron as reference instead of the jet axis is discussed in Section 7.1.2

2136 Third, the results from the dihadron analysis are done in  $p_{T,\text{trigger}}$  bins. This  
 2137 favours hard jets, i.e. jets where the leading hadron carries a large momentum  
 2138 fraction and the jet multiplicity is small. In  $p_{T,\text{jet}}$  bins jets are more likely to be  
 2139 soft, i.e. they have a small leading momentum fraction and high multiplicity jets.

### 2140 7.1.1 Different $R$ parameters

2141 The size of the jet cone gives a limit for  $j_T$ . For a track with a fixed momentum  
 2142  $p$  this is a hard limit. This is conveniently seen as  $j_{T,\text{max}}$  can be given in terms of  
 2143 cone size  $R$  and momentum  $p$ . In the small angle approximation limit

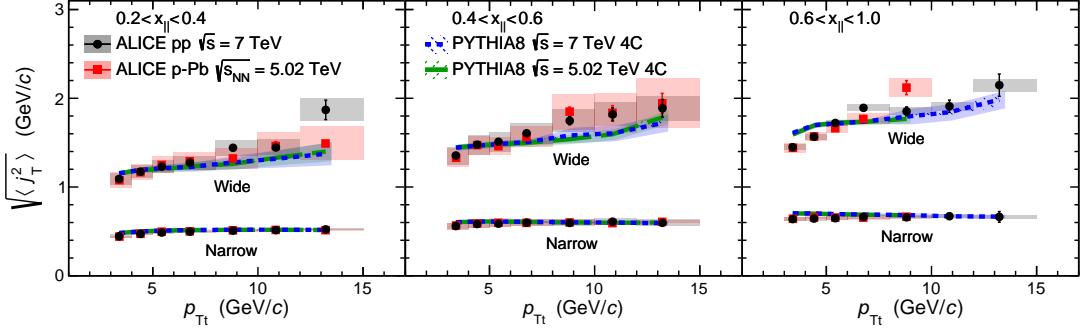


Figure 63: RMS values of the narrow and wide  $j_T$  components in the dihadron correlation analysis. Results from pp collisions at  $\sqrt{s} = 7$  TeV (circular symbols) and from p–Pb collisions at  $\sqrt{s_{NN}} = 5.02$  TeV (square symbols) are compared to PYTHIA 8 tune 4C simulations at  $\sqrt{s} = 7$  TeV (short dashed line) and at  $\sqrt{s} = 5.02$  TeV (long dashed line). Different panels correspond to different  $x_{\parallel}$ bins with  $0.2 < x_{\parallel} < 0.4$  on the left,  $0.4 < x_{\parallel} < 0.6$  in the middle, and  $0.6 < x_{\parallel} < 1.0$  on the right. The statistical errors are represented by bars and the systematic errors by boxes. [277]

$$j_{T,\max} \approx p \cdot R. \quad (73)$$

2144 Thus for tracks with  $p_{T,\text{track}} < p_{T0}$ , must be  $j_T < p_{T0} \cdot R$ . This illustrated in  
2145 Figure 65.

2146 We studied the effect of cone sizes on  $j_T$  distribution with a PYTHIA simulation.  
2147 Distributions with different cone sizes in different  $p_{T,\text{jet}}$  bins are shown in Figure 66.  
2148 The increase of high  $j_T$  with increasing cone size,  $R$ , is clearly seen in the individual  
2149  $j_T$  distributions. At low  $j_T$  there is no change within the errors.

2150 When looking at the RMS values from wide component we see an increase  
2151 or decrease of about 10% when going from  $R = 0.4$  to  $R = 0.5$  or  $R = 0.3$ ,  
2152 respectively. This is seen in Figure 67. The message from narrow component RMS  
2153 values is less clear. At low jet  $p_T$  the behaviour is similar, but at high  $p_T$  the order  
2154 is reversed.

### 2155 7.1.2 Leading tracks versus jet

2156 In comparison to the leading hadron the jet axis from jet reconstruction should  
2157 provide a better estimate of the original parton. The assumption is that because  
2158 the leading hadron is an imperfect estimate of the jet axis, low  $j_T$  tracks should  
2159 on average be shifted to higher  $j_T$ .

2160 Because the leading track is at an angle compared to the jet axis, the resulting  
2161  $j_T$  values are different. In practice the jet axis found by the jet finding algorithm

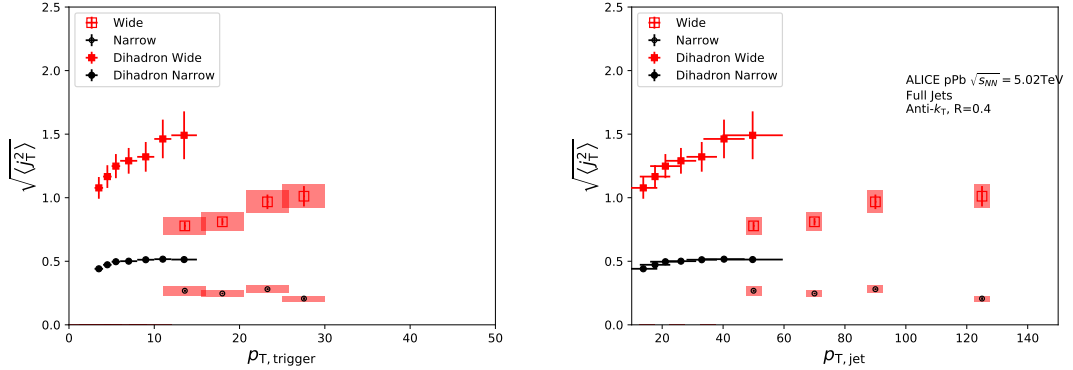


Figure 64: Jet  $j_T$  results are compared to results obtained in the dihadron analysis. Dihadron trigger  $p_T$  bins are converted to jet  $p_T$  bins using observed mean  $p_{T,\text{jet}}$  values in  $p_{T,\text{trigger}}$  bins. Dihadron results are for  $0.2 < x_{\parallel} < 0.4$

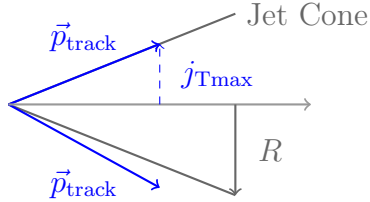


Figure 65:  $j_T$  has maximum value defined by the cone size and track momentum  $\vec{p}_{\text{track}}$

tends to minimise the average  $j_T$  of jet constituents, as at least the hardest constituents should be close to the jet axis. Thus the yield at high  $j_T$  is reduced and the RMS values get smaller. On the other hand, when using the leading hadron as a reference, it is naturally missing from the set of tracks for which  $j_T$  is calculated. This causes a decrease in the yield at low  $j_T$ .

We performed a PYTHIA study where  $j_T$  was calculated with respect to the leading track momentum, instead of the jet axis. The results are shown in Figure 68. The resulting  $j_T$  distributions are significantly wider than  $j_T$  distributions from using the jet axis as reference. The effect seems to be larger than that seen in comparing different  $R$  values.

A direct comparison between jet and dihadron  $j_T$  measurements is not possible. But combined with the  $R$  dependence of  $\sqrt{\langle j_T^2 \rangle}$  the difference between  $\sqrt{\langle j_T^2 \rangle}$  values in jet and dihadron analyses can be quantitatively understood.

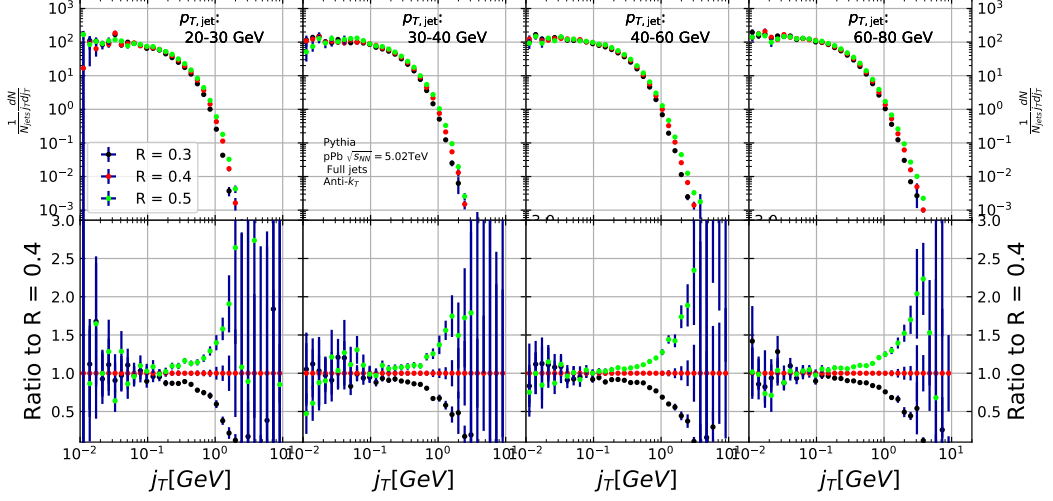


Figure 66: Effect of changing cone size on  $j_T$  distributions. The change is done both for the  $R$  parameter in the anti- $k_T$  algorithm, and for the size of the cone where  $j_T$  is calculated.

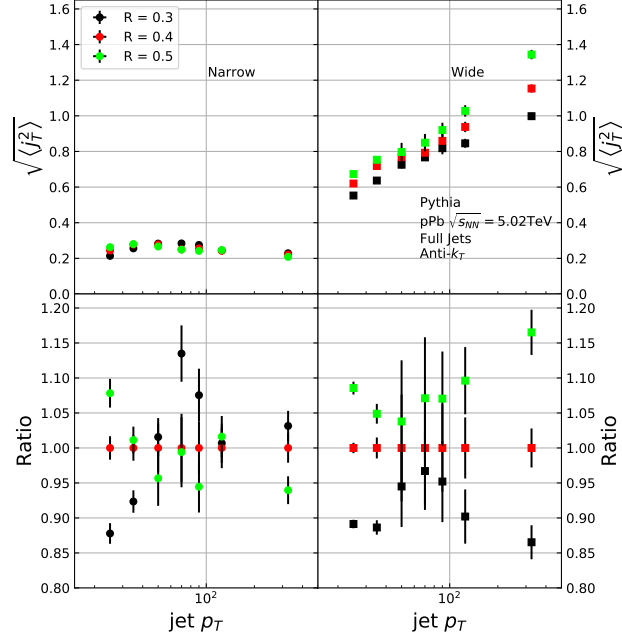


Figure 67: Effect of changing  $R$  parameter in jet finding on narrow and wide component RMS values. Wide component RMS values increase with increasing cone size.

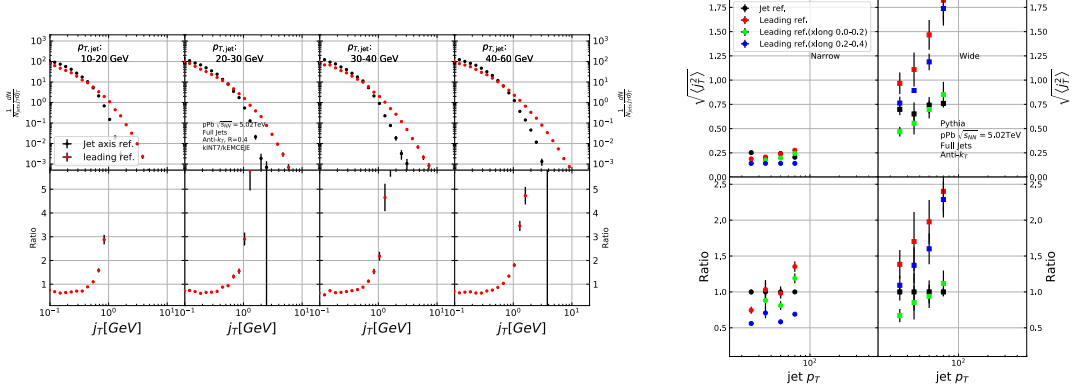


Figure 68: Results of calculating  $j_T$  with respect to the leading hadron, instead of the jet axis in a PYTHIA simulation are shown.

## 2175 8 Summary

2176 In this thesis I have studied the jet fragmentation transverse momentum at  
 2177  $\sqrt{s_{NN}} = 5.02$  TeV in p–Pb collisions. The analysis was performed using jets  
 2178 reconstructed with the anti- $k_T$  algorithm. The resulting  $j_T$  distributions were  
 2179 fitted with a two component model, which allows us to separate two distinct  
 2180 components. The width of the narrow component was found to depend weakly  
 2181 on jet  $p_T$ . The narrow component has been associated with the non-perturbative  
 2182 hadronisation process. This is consistent with the assumption that hadronisation  
 2183 is universal, i.e. it doesn't depend on the hard scattering.

2184 The width of the wide component was found to get larger with increasing  
 2185  $p_{T,jet}$ . This is in part explained by the changing kinematical limits when going  
 2186 to higher  $p_{T,jet}$  which allows higher  $p_{T,track}$ . Additionally the larger phase space  
 2187 allows stronger parton splitting.

2188 Both the narrow and wide component RMS values were well described by  
 2189 PYTHIA , but Herwig gave larger RMS values for the wide component than data. In  
 2190 the narrow component there was no difference between the models. Both describe  
 2191 the data well. This component was associated with hadronisation. At least in  
 2192 this context the different hadronisation algorithms of PYTHIA (string model) and  
 2193 Herwig (cluster model) give similar results.

Similar analysis has been performed with dihadron correlations [277]. Although a direct comparison between the results is not possible, they are qualitatively compatible with each other. The difference is understood to come from the different  $j_T$  reference, the cone size limitation in jet  $j_T$  analysis and the kinematical bias that arises from using  $p_{T,\text{trigger}}$  bins which favours harder jets than using  $p_{T,\text{jet}}$  bins. The dihadron analysis saw no difference between results in pp and p–Pb datasets and concluded that there were no cold nuclear matter effects. The same is expected to be true for the jet  $j_T$ . This is further supported by the agreement between PYTHIA and data as PYTHIA results are for pp collisions.

To study possible QGP effects in high multiplicity p–Pb collisions the analysis was repeated using different multiplicity selections. So far no jet observables have shown conclusive evidence of modification in p–Pb events. However these are primarily based on measuring yield, which makes them vulnerable to biases when selecting for multiplicity. Thus these measurements have been only performed in minimum bias events. As  $j_T$  is based on shape on a per-jet basis, it should not be sensitive to these selection biases. No effect was seen in any of the multiplicity selections. However, with the statistics available, the effect should be quite large ( $\gtrsim 20\%$ ) to be visible.

Naturally the next step would be extending the analysis to Pb–Pb data to gain better understanding of jet modification. Jet analysis in a heavy-ion collision with significant contributions from the underlying event has proved challenging [6]. However, experimental methods have improved in recent years. For the  $j_T$  analysis presented in this thesis the main challenge would be the background subtraction method. Because of anisotropic flow in heavy ion collisions the background inside the jet cone and a cone perpendicular to it would be different. It's unclear if the perpendicular cone method can be modified or if a completely new approach is required.

It has been shown that in Pb–Pb collisions jets become softer and wider because of medium-induced radiation [6]. On the other hand, the hot medium suppresses gluon jets more than quark jets. This has the opposite effect, narrowing jets, as gluon jets are naturally wider than quark jets [278]. How these different effects combine in  $j_T$  needs to be studied.

## 2226 References

- 2227 [1] D. J. Gross and F. Wilczek, Physical Review D **8**, 3633 (1973).
- 2228 [2] Particle Data Group, M. Tanabashi *et al.*, Phys. Rev. **D98**, 030001 (2018).
- 2229 [3] M. L. Perl, E. R. Lee, and D. Loomba, Mod. Phys. Lett. **A19**, 2595 (2004).
- 2230 [4] E. Shuryak, Phys. Reps. **61**, 71 (1980).
- 2231 [5] D. H. Perkins, *Introduction to high energy physics* (, 1982).
- 2232 [6] M. Connors, C. Nattrass, R. Reed, and S. Salur, Rev. Mod. Phys. **90**, 025005  
2233 (2018), 1705.01974.
- 2234 [7] J. L. Nagle and W. A. Zajc, Ann. Rev. Nucl. Part. Sci. **68**, 211 (2018),  
2235 1801.03477.
- 2236 [8] E. S., Monatshefte für Mathematik und Physik **26**, A38 (1915).
- 2237 [9] P. A. M. Dirac and N. H. D. Bohr, Proceedings of the  
2238 Royal Society of London. Series A, Containing Papers of  
2239 a Mathematical and Physical Character **114**, 243 (1927),  
2240 <https://royalsocietypublishing.org/doi/pdf/10.1098/rspa.1927.0039>.
- 2241 [10] S. Tomonaga, Prog. Theor. Phys. **1**, 27 (1946).
- 2242 [11] J. S. Schwinger, Phys. Rev. **75**, 651 (1948), [,59(1948)].
- 2243 [12] J. S. Schwinger, Phys. Rev. **74**, 1439 (1948), [,36(1948)].
- 2244 [13] R. P. Feynman, Phys. Rev. **74**, 1430 (1948).
- 2245 [14] M. L. Krauss, *The Greatest Story Ever Told—So Far: Why Are We Here?* (, 2017).
- 2247 [15] S. L. Glashow, J. Iliopoulos, and L. Maiani, Phys. Rev. **D2**, 1285 (1970).
- 2248 [16] A. Salam and J. C. Ward, Phys. Lett. **13**, 168 (1964).
- 2249 [17] S. Weinberg, Phys. Rev. Lett. **19**, 1264 (1967).
- 2250 [18] G. P. S. Occhialini and C. F. Powell, (1987), [Nature159,186(1947)].
- 2251 [19] C. M. G. Lattes, G. P. S. Occhialini, and C. F. Powell, Nature **160**, 453  
2252 (1947), [,99(1947)].

- 2253 [20] R. Bjorklund, W. Crandall, B. J. Moyer, and H. York, Phys. Review **77**,  
 2254 213 (1950).
- 2255 [21] O. Chamberlain, E. Segre, C. Wiegand, and T. Ypsilantis, Phys. Rev. **100**,  
 2256 947 (1955).
- 2257 [22] B. Cork, G. R. Lambertson, O. Piccioni, and W. A. Wenzel, Phys. Rev.  
 2258 **104**, 1193 (1957).
- 2259 [23] L. W. Alvarez *et al.*, Phys. Rev. Lett. **2**, 215 (1959).
- 2260 [24] R. Armenteros, K. Barker, C. Butler, A. Cachon, and C. York, The London,  
 2261 Edinburgh, and Dublin Philosophical Magazine and Journal of Science **43**,  
 2262 597 (1952), <https://doi.org/10.1080/14786440608520216>.
- 2263 [25] A. Bonetti, R. L. Setti, M. Panetti, and G. Tomasini, Il Nuovo Cimento  
 2264 (1943-1954) **10**, 1736 (1953).
- 2265 [26] R. Plano, N. Samios, M. Schwartz, and J. Steinberger, Il Nuovo Cimento  
 2266 (1955-1965) **5**, 216 (1957).
- 2267 [27] W. B. Fowler, R. P. Shutt, A. M. Thorndike, and W. L. Whittemore, Phys.  
 2268 Rev. **91**, 1287 (1953).
- 2269 [28] W. Heisenberg, Zeitschrift für Physik **77**, 1 (1932).
- 2270 [29] M. Gell-Mann, Phys. Rev. **125**, 1067 (1962).
- 2271 [30] V. E. Barnes *et al.*, Phys. Lett. **12**, 134 (1964).
- 2272 [31] M. Gell-Mann, Phys. Lett. **8**, 214 (1964).
- 2273 [32] G. Zweig, An SU(3) model for strong interaction symmetry and its break-  
 2274 ing. Version 2, in *DEVELOPMENTS IN THE QUARK THEORY OF*  
 2275 *HADRONS. VOL. 1. 1964 - 1978*, edited by D. Lichtenberg and S. P. Rosen,  
 2276 pp. 22–101, 1964.
- 2277 [33] O. Greenberg, Phys. Rev. Lett. **13**, 598 (1964).
- 2278 [34] H. Fritzsch and M. Gell-Mann, eConf **C720906V2**, 135 (1972), hep-  
 2279 ph/0208010.
- 2280 [35] Crystal Ball Collaboration, D. Williams *et al.*, Phys. Rev. **D38**, 1365 (1988).
- 2281 [36] W. Krolikowski, Nuovo Cim. **A27**, 194 (1975).

- 2282 [37] E. D. Bloom *et al.*, Phys. Rev. Lett. **23**, 930 (1969).
- 2283 [38] M. Breidenbach *et al.*, Phys. Rev. Lett. **23**, 935 (1969).
- 2284 [39] The nobel prize in physics 1990, <https://www.nobelprize.org/prizes/physics/1990/summary/>,  
2285 Accessed: Mon. 8 Apr 2019.
- 2286 [40] J. D. Bjorken, Phys. Rev. **179**, 1547 (1969).
- 2287 [41] J. D. Bjorken and E. A. Paschos, Phys. Rev. **185**, 1975 (1969).
- 2288 [42] R. P. Feynman, Phys. Rev. Lett. **23**, 1415 (1969), [,494(1969)].
- 2289 [43] D. J. Gross and F. Wilczek, Physical Review Letters **30**, 1343 (1973).
- 2290 [44] H. D. Politzer, Physical Review Letters **30**, 1346 (1973).
- 2291 [45] D. J. Gross and F. Wilczek, Physical Review D **9**, 980 (1974).
- 2292 [46] H. Georgi and H. D. Politzer, Physical Review D **9**, 416 (1974).
- 2293 [47] The nobel prize in physics 2004, <https://www.nobelprize.org/prizes/physics/2004/summary/>,  
2294 Accessed: Mon. 8 Apr 2019.
- 2295 [48] H. Fritzsch, M. Gell-Mann, and H. Leutwyler, Physics Letters B **47**, 365  
2296 (1973).
- 2297 [49] SLAC-SP-017, J. E. Augustin *et al.*, Phys. Rev. Lett. **33**, 1406 (1974), [Adv.  
2298 Exp. Phys.5,141(1976)].
- 2299 [50] E598, J. J. Aubert *et al.*, Phys. Rev. Lett. **33**, 1404 (1974).
- 2300 [51] C. Bacci *et al.*, Phys. Rev. Lett. **33**, 1408 (1974), [Erratum: Phys. Rev.  
2301 Lett.33,1649(1974)].
- 2302 [52] The nobel prize in physics 1976, <https://www.nobelprize.org/prizes/physics/1976/summary/>,  
2303 Accessed: Mon. 8 Apr 2019.
- 2304 [53] J. D. Bjorken and S. L. Glashow, Phys. Lett. **11**, 255 (1964).
- 2305 [54] I. Flegel and P. Söding, CERN courier (2004).
- 2306 [55] R. Brandelik *et al.*, Physics Letters B **86**, 243 (1979).
- 2307 [56] J. K. L. MacDonald, Phys. Rev. **43**, 830 (1933).
- 2308 [57] C. Berger *et al.*, Physics Letters B **86**, 418 (1979).

- 2309 [58] M. Kobayashi and T. Maskawa, Prog. Theor. Phys. **49**, 652 (1973).
- 2310 [59] The nobel prize in physics 2008, <https://www.nobelprize.org/prizes/physics/2008/summary/>,  
2311 Accessed: Mon. 8 Apr 2019.
- 2312 [60] S. W. Herb *et al.*, Phys. Rev. Lett. **39**, 252 (1977).
- 2313 [61] CDF, F. Abe *et al.*, Phys. Rev. Lett. **74**, 2626 (1995), hep-ex/9503002.
- 2314 [62] D0, S. Abachi *et al.*, Phys. Rev. Lett. **74**, 2422 (1995), hep-ex/9411001.
- 2315 [63] J. Collins and M. Perry, Phys. rev. Lett. **34**, 1353 (1975).
- 2316 [64] K. Rajagopal, SLAC Beam Line **31-2**, 9 (2001).
- 2317 [65] P. Kovtun, D. Son, and A. Starinets, Phys.Rev.Lett. **94**, 111601 (2005),  
2318 hep-th/0405231.
- 2319 [66] R. A. Lacey *et al.*, Phys. Rev. Lett. **98**, 092301 (2007).
- 2320 [67] E. Lofgren, *ACCELERATOR DIVISION ANNUAL REPORTS, 1 JULY*  
2321 *1972 12/31/1974* (, 1975).
- 2322 [68] D. S. Barton, Heavy ion program at bnl: Ags, rhic, in *Proc. 1987 Particle*  
2323 *Accelerator Conference, Washington, D.C., March, 1987*, 1987.
- 2324 [69] I. Vitev and M. Gyulassy, Phys.Rev.Lett. **89**, 252301 (2002), hep-  
2325 ph/0209161.
- 2326 [70] A. Kovalenko *et al.*, Status of the nuclotron, in *Proceedings of EPAC* Vol. 94,  
2327 pp. 161–164, 1994.
- 2328 [71] New state of matter created at cern, <https://home.cern/news/press-release/cern/new-state-matter-created-cern>, Accessed: Sat. 6 Apr 2019.
- 2330 [72] NA61/SHINE, K. Grebieszkow, PoS **CPOD2013**, 004 (2013).
- 2331 [73] PHENIX Collaboration, K. Adcox *et al.*, Nucl.Phys. **A757**, 184 (2005),  
2332 nucl-ex/0410003.
- 2333 [74] STAR Collaboration, J. Adams *et al.*, Nucl.Phys. **A757**, 102 (2005), nucl-  
2334 ex/0501009.
- 2335 [75] BRAHMS Collaboration, I. Arsene *et al.*, Nucl.Phys. **A757**, 1 (2005), nucl-  
2336 ex/0410020.
- 2337 [76] B. Back *et al.*, Nucl.Phys. **A757**, 28 (2005), nucl-ex/0410022.

- 2338 [77] LHCb, E. Maurice, Fixed-target physics at LHCb, in *5th Large Hadron*  
2339 *Collider Physics Conference (LHCP 2017) Shanghai, China, May 15-20,*  
2340 *2017*, 2017, 1708.05184.
- 2341 [78] S. A. Voloshin, A. M. Poskanzer, and R. Snellings, (2008), 0809.2949.
- 2342 [79] S. A. Voloshin, A. M. Poskanzer, A. Tang, and G. Wang, Phys.Lett. **B659**,  
2343 537 (2008), 0708.0800.
- 2344 [80] H. Holopainen, H. Niemi, and K. J. Eskola, Phys.Rev. **C83**, 034901 (2011),  
2345 1007.0368.
- 2346 [81] ALICE Collaboration, Phys. Rev. C **88**, 044909 (2013).
- 2347 [82] M. L. Miller, K. Reygers, S. J. Sanders, and P. Steinberg,  
2348 Ann.Rev.Nucl.Part.Sci. **57**, 205 (2007), nucl-ex/0701025.
- 2349 [83] R. Glauber, Lectures in theoretical physics, 1959.
- 2350 [84] A. Białłas, M. Bleszyński, and W. Czyż, Nuclear Physics B **111**, 461 (1976).
- 2351 [85] H. De Vries, C. W. De Jager, and C. De Vries, Atom. Data Nucl. Data Tabl.  
2352 **36**, 495 (1987).
- 2353 [86] ALICE, B. Abelev *et al.*, Phys. Rev. **C88**, 044909 (2013), 1301.4361.
- 2354 [87] PHENIX Collaboration, S. Afanasiev *et al.*, Phys.Rev. **C80**, 054907 (2009),  
2355 0903.4886.
- 2356 [88] D. Kharzeev, E. Levin, and M. Nardi, Nucl. Phys. **A747**, 609 (2005), hep-  
2357 ph/0408050.
- 2358 [89] W.-T. Deng, X.-N. Wang, and R. Xu, Phys. Rev. **C83**, 014915 (2011),  
2359 1008.1841.
- 2360 [90] TOTEM, G. Antchev *et al.*, Eur. Phys. J. **C79**, 103 (2019), 1712.06153.
- 2361 [91] B. Alver, M. Baker, C. Loizides, and P. Steinberg, (2008), 0805.4411.
- 2362 [92] P. Romatschke, Int.J.Mod.Phys. **E19**, 1 (2010), 0902.3663.
- 2363 [93] K. A. *et al.* [ALICE Collaboration], Phys. Rev. Lett **106** (2011), 032301.
- 2364 [94] J.-Y. Ollitrault, Phys. Rev. D **46**, 229 (1992).
- 2365 [95] J.-Y. Ollitrault, Phys.Rev. D **48**, 1132 (1993), hep-ph/9303247.

- <sup>2366</sup> [96] U. Heinz and P. Kolb, Nucl. Phys. **A702**, 269 (2002).
- <sup>2367</sup> [97] S. Voloshin and Y. Zhang, Z.Phys. **C70**, 665 (1996), hep-ph/9407282.
- <sup>2368</sup> [98] B. Alver and G. Roland, Phys.Rev. **C81**, 054905 (2010), 1003.0194.
- <sup>2369</sup> [99] A. Mocsy and P. Sorensen, (2010), 1008.3381.
- <sup>2370</sup> [100] A. P. Mishra, R. K. Mohapatra, P. Saumia, and A. M. Srivastava, Phys.Rev. **C77**, 064902 (2008), 0711.1323.
- <sup>2372</sup> [101] T. Abbott *et al.*, Phys. Rev. Lett. **70**, 1393 (1993).
- <sup>2373</sup> [102] B. Schenke, S. Jeon, and C. Gale, Phys.Lett. **B702**, 59 (2011), 1102.0575.
- <sup>2374</sup> [103] K. A. *et al.* [ALICE Collaboration], Phys. Rev. Lett. **107** (2011), 032301.
- <sup>2375</sup> [104] K. Aamodt *et al.*, Physics Letters B **708**, 249 (2012).
- <sup>2376</sup> [105] L. LD, Izv. Akad. Nauk Ser. Fiz. **17**, 51 (1953).
- <sup>2377</sup> [106] J. D. Bjorken, Phys. Rev. D **27**, 140 (1983).
- <sup>2378</sup> [107] G. Baym, B. L. Friman, J. P. Blaizot, M. Soyeur, and W. Czyz, Nucl. Phys. **A407**, 541 (1983).
- <sup>2380</sup> [108] H. von Gersdorff, L. McLerran, M. Kataja, and P. V. Ruuskanen, Phys. Rev. D **34**, 794 (1986).
- <sup>2382</sup> [109] H. Niemi, K. J. Eskola, and R. Paatelainen, Phys. Rev. **C93**, 024907 (2016), 1505.02677.
- <sup>2384</sup> [110] R. Paatelainen, K. J. Eskola, H. Holopainen, and K. Tuominen, Phys. Rev. **C87**, 044904 (2013), 1211.0461.
- <sup>2386</sup> [111] R. Paatelainen, K. J. Eskola, H. Niemi, and K. Tuominen, Phys. Lett. **B731**, 126 (2014), 1310.3105.
- <sup>2388</sup> [112] ALICE, J. Adam *et al.*, Phys. Rev. Lett. **117**, 182301 (2016), 1604.07663.
- <sup>2389</sup> [113] J. E. Bernhard, J. S. Moreland, S. A. Bass, J. Liu, and U. Heinz, Phys. Rev. C **94**, 024907 (2016).
- <sup>2391</sup> [114] ALICE, S. Acharya *et al.*, Phys. Rev. **C97**, 024906 (2018), 1709.01127.
- <sup>2392</sup> [115] ALICE, S. Acharya *et al.*, Phys. Lett. **B773**, 68 (2017), 1705.04377.

- <sup>2393</sup> [116] A. Metz and A. Vossen, Prog. Part. Nucl. Phys. **91**, 136 (2016), 1607.02521.
- <sup>2394</sup> [117] R. Placakyte, Parton Distribution Functions, in *Proceedings, 31st International Conference on Physics in collisions (PIC 2011): Vancouver, Canada, August 28-September 1, 2011*, 2011, 1111.5452.
- <sup>2397</sup> [118] V. N. Gribov and L. N. Lipatov, Sov. J. Nucl. Phys. **15**, 438 (1972), [Yad. Fiz.15,781(1972)].
- <sup>2398</sup>
- <sup>2399</sup> [119] G. Altarelli and G. Parisi, Nucl. Phys. **B126**, 298 (1977).
- <sup>2400</sup> [120] Y. L. Dokshitzer, Sov. Phys. JETP **46**, 641 (1977), [Zh. Eksp. Teor. Fiz.73,1216(1977)].
- <sup>2401</sup>
- <sup>2402</sup> [121] J. Pumplin *et al.*, JHEP **07**, 012 (2002), hep-ph/0201195.
- <sup>2403</sup> [122] ZEUS, H1, A. M. Cooper-Sarkar, PoS **EPS-HEP2011**, 320 (2011), 1112.2107.
- <sup>2404</sup>
- <sup>2405</sup> [123] J. Butterworth *et al.*, J. Phys. **G43**, 023001 (2016), 1510.03865.
- <sup>2406</sup> [124] T. Sjöstrand and P. Z. Skands, Eur. Phys. J. **C39**, 129 (2005), hep-ph/0408302.
- <sup>2407</sup>
- <sup>2408</sup> [125] T. Sjöstrand *et al.*, Comput. Phys. Commun. **191**, 159 (2015), 1410.3012.
- <sup>2409</sup> [126] M. Bahr *et al.*, Eur. Phys. J. **C58**, 639 (2008), 0803.0883.
- <sup>2410</sup> [127] A. Buckley *et al.*, Phys. Rept. **504**, 145 (2011), 1101.2599.
- <sup>2411</sup> [128] Y. L. Dokshitzer, V. A. Khoze, A. H. Müller, and S. I. Troian, *Basics of Perturbative QCD* (Editions Frontières, Gif-sur-Yvette, France, 1991).
- <sup>2412</sup>
- <sup>2413</sup> [129] Y. I. Azimov, Y. L. Dokshitzer, V. A. Khoze, and S. I. Trovan, Zeitschrift für Physik C Particles and Fields **27**, 65 (1985).
- <sup>2414</sup>
- <sup>2415</sup> [130] B. Andersson, G. Gustafson, G. Ingelman, and T. Sjöstrand, Physics Reports **97**, 31 (1983).
- <sup>2416</sup>
- <sup>2417</sup> [131] ALICE Collaboration, K. Aamodt *et al.*, Phys.Lett. **B696**, 30 (2011), 1012.1004.
- <sup>2418</sup>
- <sup>2419</sup> [132] WA98 Collaboration, M. Aggarwal *et al.*, Eur.Phys.J. **C23**, 225 (2002), nucl-ex/0108006.
- <sup>2420</sup>
- <sup>2421</sup> [133] D. G. d'Enterria, Phys.Lett. **B596**, 32 (2004), nucl-ex/0403055.

- <sup>2422</sup> [134] PHENIX Collaboration, A. Adare *et al.*, Phys.Rev.Lett. **101**, 232301 (2008),  
<sup>2423</sup> 0801.4020.
- <sup>2424</sup> [135] STAR Collaboration, J. Adams *et al.*, Phys.Rev.Lett. **91**, 172302 (2003),  
<sup>2425</sup> nucl-ex/0305015.
- <sup>2426</sup> [136] A. Dainese, C. Loizides, and G. Paic, Eur.Phys.J. **C38**, 461 (2005), hep-  
<sup>2427</sup> ph/0406201.
- <sup>2428</sup> [137] I. Vitev, J.Phys. **G30**, S791 (2004), hep-ph/0403089.
- <sup>2429</sup> [138] C. A. Salgado and U. A. Wiedemann, Phys.Rev. **D68**, 014008 (2003), hep-  
<sup>2430</sup> ph/0302184.
- <sup>2431</sup> [139] N. Armesto, A. Dainese, C. A. Salgado, and U. A. Wiedemann, Phys.Rev.  
<sup>2432</sup> **D71**, 054027 (2005), hep-ph/0501225.
- <sup>2433</sup> [140] T. Renk, H. Holopainen, R. Paatelainen, and K. J. Eskola, Phys.Rev. **C84**,  
<sup>2434</sup> 014906 (2011), 1103.5308.
- <sup>2435</sup> [141] CMS Collaboration, S. Chatrchyan *et al.*, Eur.Phys.J. **C72**, 1945 (2012),  
<sup>2436</sup> 1202.2554.
- <sup>2437</sup> [142] PHENIX, S. S. Adler *et al.*, Phys. Rev. **C76**, 034904 (2007), nucl-  
<sup>2438</sup> ex/0611007.
- <sup>2439</sup> [143] PHENIX, A. Adare *et al.*, Phys. Rev. **C88**, 064910 (2013), 1309.4437.
- <sup>2440</sup> [144] ALICE, B. Abelev *et al.*, Phys. Lett. **B719**, 18 (2013), 1205.5761.
- <sup>2441</sup> [145] CMS, S. Chatrchyan *et al.*, Phys. Rev. Lett. **109**, 022301 (2012), 1204.1850.
- <sup>2442</sup> [146] W. H. H. Bethe and, Proc.Roy.Soc.Lond. **A146** (1934).
- <sup>2443</sup> [147] L. D. Landau and I. Pomeranchuk, Dokl. Akad. Nauk Ser. Fiz. **92**, 535  
<sup>2444</sup> (1953).
- <sup>2445</sup> [148] A. B. Migdal, Phys. Rev. **103**, 1811 (1956).
- <sup>2446</sup> [149] P. Bosted *et al.*, Quantum-mechanical suppression of bremsstrahlung\*, 1993.
- <sup>2447</sup> [150] R. Baier, Y. L. Dokshitzer, A. H. Mueller, S. Peigne, and D. Schiff, Nucl.  
<sup>2448</sup> Phys. **B484**, 265 (1997), hep-ph/9608322.
- <sup>2449</sup> [151] A. Majumder and M. Van Leeuwen, Prog.Part.Nucl.Phys. **A66**, 41 (2011),  
<sup>2450</sup> 1002.2206.

- <sup>2451</sup> [152] F. Dominguez, C. Marquet, A. Mueller, B. Wu, and B.-W. Xiao, Nucl.Phys. **A811**, 197 (2008), 0803.3234.
- <sup>2453</sup> [153] M. Gyulassy, P. Levai, and I. Vitev, Nucl.Phys. **B571**, 197 (2000), hep-ph/9907461.
- <sup>2455</sup> [154] U. A. Wiedemann, Nucl.Phys. **B588**, 303 (2000), hep-ph/0005129.
- <sup>2456</sup> [155] P. B. Arnold, G. D. Moore, and L. G. Yaffe, JHEP **0112**, 009 (2001), hep-ph/0111107.
- <sup>2458</sup> [156] X.-N. Wang and X.-f. Guo, Nucl.Phys. **A696**, 788 (2001), hep-ph/0102230.
- <sup>2459</sup> [157] T. Sjostrand, S. Mrenna, and P. Z. Skands, Comput.Phys.Commun. **178**, 852 (2008), 0710.3820.
- <sup>2461</sup> [158] I. Lokhtin and A. Snigirev, Eur.Phys.J. **C45**, 211 (2006), hep-ph/0506189.
- <sup>2462</sup> [159] N. Armesto, L. Cunqueiro, and C. A. Salgado, Nucl.Phys. **A830**, 271C (2009), 0907.4706.
- <sup>2464</sup> [160] K. Zapp, G. Ingelman, J. Rathsman, J. Stachel, and U. A. Wiedemann, Eur.Phys.J. **C60**, 617 (2009), 0804.3568.
- <sup>2466</sup> [161] T. Renk, Phys.Rev. **C79**, 054906 (2009), 0901.2818.
- <sup>2467</sup> [162] ALICE, J. Adam *et al.*, Phys. Lett. **B746**, 1 (2015), 1502.01689.
- <sup>2468</sup> [163] ATLAS, G. Aad *et al.*, Phys. Rev. Lett. **114**, 072302 (2015), 1411.2357.
- <sup>2469</sup> [164] CMS, V. Khachatryan *et al.*, Phys. Rev. **C96**, 015202 (2017), 1609.05383.
- <sup>2470</sup> [165] STAR, L. Adamczyk *et al.*, Phys. Rev. Lett. **112**, 122301 (2014), 1302.6184.
- <sup>2471</sup> [166] CMS, V. Khachatryan *et al.*, JHEP **02**, 156 (2016), 1601.00079.
- <sup>2472</sup> [167] A. Kurkela and U. A. Wiedemann, Phys. Lett. **B740**, 172 (2015), 1407.0293.
- <sup>2473</sup> [168] JETSCAPE, Y. Tachibana *et al.*, Jet substructure modification in a QGP from a multi-scale description of jet evolution with JETSCAPE, 2018, 1812.06366.
- <sup>2476</sup> [169] P. Aurenche and B. G. Zakharov, Eur. Phys. J. **C71**, 1829 (2011), 1109.6819.
- <sup>2477</sup> [170] A. Beraudo, J. G. Milhano, and U. A. Wiedemann, Phys. Rev. **C85**, 031901 (2012), 1109.5025.

- <sup>2479</sup> [171] A. Beraudo, J. G. Milhano, and U. A. Wiedemann, JHEP **07**, 144 (2012), 1204.4342.
- <sup>2480</sup>
- <sup>2481</sup> [172] J. Casalderrey-Solana, Y. Mehtar-Tani, C. A. Salgado, and K. Tywoniuk, Phys. Lett. **B725**, 357 (2013), 1210.7765.
- <sup>2482</sup>
- <sup>2483</sup> [173] F. D'Eramo, M. Lekaveckas, H. Liu, and K. Rajagopal, JHEP **05**, 031 (2013), 1211.1922.
- <sup>2484</sup>
- <sup>2485</sup> [174] A. Ayala, I. Dominguez, J. Jalilian-Marian, and M. E. Tejeda-Yeomans, Phys. Rev. **C94**, 024913 (2016), 1603.09296.
- <sup>2486</sup>
- <sup>2487</sup> [175] G. Moliere, Z. Naturforsch. **A2**, 133 (1947).
- <sup>2488</sup> [176] CMS, S. Chatrchyan *et al.*, Phys. Rev. **C84**, 024906 (2011), 1102.1957.
- <sup>2489</sup> [177] C. Aidala *et al.*, Phys. Rev. **C95**, 034910 (2017), 1609.02894.
- <sup>2490</sup> [178] PHENIX, S. S. Adler *et al.*, Phys. Rev. Lett. **91**, 072303 (2003), nucl-ex/0306021.
- <sup>2491</sup>
- <sup>2492</sup> [179] BRAHMS, I. Arsene *et al.*, Phys. Rev. Lett. **91**, 072305 (2003), nucl-ex/0307003.
- <sup>2493</sup>
- <sup>2494</sup> [180] PHOBOS, B. B. Back *et al.*, Phys. Rev. Lett. **91**, 072302 (2003), nucl-ex/0306025.
- <sup>2495</sup>
- <sup>2496</sup> [181] STAR, J. Adams *et al.*, Phys. Rev. Lett. **91**, 072304 (2003), nucl-ex/0306024.
- <sup>2497</sup> [182] PHENIX, A. Adare *et al.*, Phys. Rev. Lett. **115**, 142301 (2015), 1507.06273.
- <sup>2498</sup> [183] E735, T. Alexopoulos *et al.*, Phys. Rev. **D48**, 984 (1993).
- <sup>2499</sup> [184] MiniMax, T. C. Brooks *et al.*, Phys. Rev. **D61**, 032003 (2000), hep-ex/9906026.
- <sup>2500</sup>
- <sup>2501</sup> [185] C. Shen, Z. Qiu, and U. Heinz, Phys. Rev. **C92**, 014901 (2015), 1502.04636.
- <sup>2502</sup> [186] PHENIX, A. Adare *et al.*, Phys. Rev. **C94**, 064901 (2016), 1509.07758.
- <sup>2503</sup> [187] CMS, V. Khachatryan *et al.*, JHEP **09**, 091 (2010), 1009.4122.
- <sup>2504</sup> [188] C. A. Salgado and J. P. Wessels, Ann. Rev. Nucl. Part. Sci. **66**, 449 (2016).
- <sup>2505</sup> [189] ATLAS, G. Aad *et al.*, Phys. Rev. Lett. **116**, 172301 (2016), 1509.04776.
- <sup>2506</sup> [190] ALICE, S. Acharya *et al.*, JHEP **09**, 032 (2017), 1707.05690.

- 2507 [191] C. Shen, J.-F. Paquet, G. S. Denicol, S. Jeon, and C. Gale, Phys. Rev. **C95**,  
2508 014906 (2017), 1609.02590.
- 2509 [192] H. Niemi and G. S. Denicol, (2014), 1404.7327.
- 2510 [193] PHENIX, C. Aidala *et al.*, Nature Phys. **15**, 214 (2019), 1805.02973.
- 2511 [194] CMS, C. Collaboration, (2018).
- 2512 [195] CMS, V. Khachatryan *et al.*, JHEP **04**, 039 (2017), 1611.01664.
- 2513 [196] ATLAS, G. Aad *et al.*, Phys. Rev. **C90**, 044906 (2014), 1409.1792.
- 2514 [197] X. Zhang and J. Liao, (2013), 1311.5463.
- 2515 [198] C. Park, C. Shen, S. Jeon, and C. Gale, Nucl. Part. Phys. Proc. **289-290**,  
2516 289 (2017), 1612.06754.
- 2517 [199] K. Tywoniuk, Nucl. Phys. **A926**, 85 (2014).
- 2518 [200] CMS, A. M. Sirunyan *et al.*, Phys. Lett. **B776**, 195 (2018), 1702.00630.
- 2519 [201] ALICE, J. Adam *et al.*, Phys. Rev. **C91**, 064905 (2015), 1412.6828.
- 2520 [202] F. Sikler, (2003), hep-ph/0304065.
- 2521 [203] Cern, <https://home.cern/>, Accessed: Wed. 17 Apr 2019.
- 2522 [204] 2019.
- 2523 [205] P. M. Watkins, Contemp. Phys. **27**, 291 (1986).
- 2524 [206] NA61/SHINE, A. Laszlo, Nucl. Phys. **A830**, 559C (2009), 0907.4493.
- 2525 [207] NA62 Collaboration, F. Hahn *et al.*, CERN Report No. NA62-10-07, 2010  
2526 (unpublished).
- 2527 [208] NA63 Collaboration, R. Mikkelsen, U. Uggerhoj, and T. Wistisen, CERN  
2528 Report No. CERN-SPSC-2014-033. SPSC-SR-146, 2014 (unpublished).
- 2529 [209] AWAKE, S. Döbert, p. TH1A04. 5 p (2018).
- 2530 [210] R. Losito, E. Laface, and W. Scandale, p. 3 p (2009).
- 2531 [211] DIRAC, C. P. Schuetz, The Dirac experiment at CERN, in *Proceedings, 38th Rencontres de Moriond on QCD and High-Energy Hadronic Interactions: Les Arcs, France, March 22-29, 2003*, 2003, hep-ph/0305121.

- <sup>2534</sup> [212] E. M. Dunne *et al.*, Science **354**, 1119 (2016),  
<sup>2535</sup> <https://science.sciencemag.org/content/354/6316/1119.full.pdf>.
- <sup>2536</sup> [213] n\_TOF, P. M. Milazzo *et al.*, AIP Conf. Proc. **1109**, 84 (2009).
- <sup>2537</sup> [214] Cern experiments, 2019.
- <sup>2538</sup> [215] O. S. Brüning *et al.*, *LHC Design Report*CERN Yellow Reports: Monographs  
<sup>2539</sup> (CERN, Geneva, 2004).
- <sup>2540</sup> [216] L. Evans and P. Bryant, JINST **3**, S08001 (2008).
- <sup>2541</sup> [217] ALICE, K. Aamodt *et al.*, JINST **3**, S08002 (2008).
- <sup>2542</sup> [218] ATLAS, G. Aad *et al.*, JINST **3**, S08003 (2008).
- <sup>2543</sup> [219] CMS, S. Chatrchyan *et al.*, JINST **3**, S08004 (2008).
- <sup>2544</sup> [220] LHCb, A. A. Alves, Jr. *et al.*, JINST **3**, S08005 (2008).
- <sup>2545</sup> [221] LHCf, O. Adriani *et al.*, JINST **3**, S08006 (2008).
- <sup>2546</sup> [222] TOTEM, G. Anelli *et al.*, JINST **3**, S08007 (2008).
- <sup>2547</sup> [223] MoEDAL, B. Acharya *et al.*, JHEP **08**, 067 (2016), 1604.06645.
- <sup>2548</sup> [224] ATLAS, G. Aad *et al.*, Phys. Lett. **B716**, 1 (2012), 1207.7214.
- <sup>2549</sup> [225] CMS, S. Chatrchyan *et al.*, Phys. Lett. **B716**, 30 (2012), 1207.7235.
- <sup>2550</sup> [226] T. ALICE Collaboration *et al.*, Journal of Instrumentation **3**, S08002 (2008).
- <sup>2551</sup> [227] ALICE, K. Aamodt *et al.*, Phys. Rev. Lett. **105**, 252301 (2010), 1011.3916.
- <sup>2552</sup> [228] ALICE, G. Dellacasa *et al.*, (2000).
- <sup>2553</sup> [229] ALICE, G. Dellacasa *et al.*, (1999).
- <sup>2554</sup> [230] ALICE, I. Belikov, EPJ Web Conf. **125**, 01004 (2016), 1607.01171.
- <sup>2555</sup> [231] J. Alme *et al.*, Nucl. Instrum. Meth. **A622**, 316 (2010), 1001.1950.
- <sup>2556</sup> [232] for the ALICE, C. Zampolli, Particle Identification with the ALICE de-  
<sup>2557</sup> tector at the LHC, in *Proceedings, PLHC2012: Physics at the LHC 2012*  
<sup>2558</sup> (*PLHC2012*): Vancouver, BC, Canada, June 4-9, 2012, 2012, 1209.5637.

- 2559 [233] ALICE Collaboration, P. Cortese, *ALICE transition-radiation detector: Technical Design Report*Technical Design Report ALICE (CERN, Geneva,  
2560 2561 2001).
- 2562 [234] ALICE, G. Dellacasa *et al.*, (2000).
- 2563 [235] ALICE, S. Beole *et al.*, (1998).
- 2564 [236] ALICE, B. Abelev *et al.*, Phys. Lett. **B717**, 162 (2012), 1205.5724.
- 2565 [237] ALICE, J. Adam *et al.*, Phys. Lett. **B754**, 235 (2016), 1509.07324.
- 2566 [238] ALICE, R. Reed, J. Phys. Conf. Ser. **446**, 012006 (2013), 1304.5945.
- 2567 [239] ALICE, G. Dellacasa *et al.*, (1999).
- 2568 [240] ALICE, P. Cortese *et al.*, (2008).
- 2569 [241] J. Allen *et al.*, Report No. CERN-LHCC-2010-011. ALICE-TDR-14-add-1,  
2570 2010 (unpublished).
- 2571 [242] ALICE, P. Cortese *et al.*, (2004).
- 2572 [243] ALICE, A. I. Maevskaya, (2018), 1812.00594.
- 2573 [244] ALICE Collaboration, *ALICE Photon Multiplicity Detector (PMD): Technical Design Report*Technical Design Report ALICE (CERN, Geneva, 1999).
- 2574
- 2575 [245] ACORDE, A. Fernández *et al.*, Nucl. Instrum. Meth. **A572**, 102 (2007),  
2576 physics/0606051.
- 2577 [246] ALICE, G. Dellacasa *et al.*, (1999).
- 2578 [247] A. Villatoro Tello, AIP Conference Proceedings **1819** (2017).
- 2579 [248] ALICE, S. Beole *et al.*, (1996).
- 2580 [249] ALICE, M. Krivda *et al.*, JINST **11**, C03051 (2016).
- 2581 [250] J. Král, *Intrinsic transverse momentum distribution of jet constituents in p-Pb collisions at ALICE*, PhD thesis, University of Jyväskylä, 2014.
- 2582
- 2583 [251] J. Kral, T. Awes, H. Muller, J. Rak, and J. Schambach, Nuclear Instruments  
2584 and Methods in Physics Research Section A: Accelerators, Spectrometers,  
2585 Detectors and Associated Equipment **693**, 261 (2012).

- 2586 [252] ALICE Collaboration, B. Abelev *et al.*, CERN Report No. CERN-LHCC-  
2587 2012-012. LHCC-I-022. ALICE-UG-002, 2012 (unpublished).
- 2588 [253] A. Maevskaya, EPJ Web Conf. **204**, 11003 (2019).
- 2589 [254] Report No. CERN-LHCC-2015-001. ALICE-TDR-018, 2015 (unpublished).
- 2590 [255] F. Sauli, L. Ropelewski, and P. Everaerts, Nucl. Instrum. Meth. **A560**, 269  
2591 (2006).
- 2592 [256] ALICE TPC, M. Ball, K. Eckstein, and T. Gunji, JINST **9**, C04025 (2014).
- 2593 [257] The ALICE Collaboration, Report No. CERN-LHCC-2013-020. ALICE-  
2594 TDR-016, 2013 (unpublished).
- 2595 [258] P. F. Little, *Secondary Effects* (Springer Berlin Heidelberg, Berlin, Heidel-  
2596 berg, 1956), pp. 574–662.
- 2597 [259] M. Vargyas, *Jet shape modification in Pb-Pb collisions at  $\sqrt{s_{NN}} = 2.76 \text{ TeV}$  using two-particle correlations*, PhD thesis, University of Jyväskylä, 2018.
- 2599 [260] ALICE TPC upgrade, J. E. Brücke and T. E. Hildén, The GEM QA Proto-  
2600 col of the ALICE TPC Upgrade Project, in *5th International Conference on*  
2601 *Micro Pattern Gas Detectors (MPGD2017) Temple University, Philadelphia,*  
2602 *USA, May 22-26, 2017*, 2018, 1811.07043.
- 2603 [261] T. Hildén *et al.*, Nucl. Instrum. Meth. **A770**, 113 (2015), 1704.06691.
- 2604 [262] ALICE, B. B. Abelev *et al.*, Int. J. Mod. Phys. **A29**, 1430044 (2014),  
2605 1402.4476.
- 2606 [263] ALICE, K. Aamodt *et al.*, JINST **5**, P03003 (2010), 1001.0502.
- 2607 [264] R. Fruhwirth, Nucl. Instrum. Meth. **A262**, 444 (1987).
- 2608 [265] A. Maire, Track reconstruction principle in ALICE for LHC run I and run  
2609 II. Principes de reconstruction de traces dans ALICE pour les runs I et II  
2610 du LHC, General Photo, 2011.
- 2611 [266] ALICE, B. Abelev *et al.*, JHEP **03**, 053 (2012), 1201.2423.
- 2612 [267] ALICE, B. Abelev *et al.*, Phys. Lett. **B719**, 29 (2013), 1212.2001.
- 2613 [268] M. Cacciari, G. P. Salam, and G. Soyez, Eur. Phys. J. **C72**, 1896 (2012),  
2614 1111.6097.

- <sub>2615</sub> [269] M. Cacciari, G. P. Salam, and G. Soyez, JHEP **04**, 063 (2008), 0802.1189.
- <sub>2616</sub> [270] T. Sjöstrand, S. Mrenna, and P. Z. Skands, Comput. Phys. Commun. **178**, 852 (2008), 0710.3820.
- <sub>2617</sub>
- <sub>2618</sub> [271] G. Upton and I. Cook, *A Dictionary of Statistics* (, 2008).
- <sub>2619</sub> [272] Roounfold: Root unfolding framework, <http://hepunx.rl.ac.uk/~adye/software/unfold/RooUnfold.html>, 2013.
- <sub>2620</sub>
- <sub>2621</sub> [273] A. Hocker and V. Kartvelishvili, Nucl. Instrum. Meth. **A372**, 469 (1996), hep-ph/9509307.
- <sub>2622</sub>
- <sub>2623</sub> [274] P. Z. Skands, Phys. Rev. **D82**, 074018 (2010), 1005.3457.
- <sub>2624</sub> [275] R. Brun, R. Hagelberg, M. Hansroul, and J. C. Lassalle, *Simulation program for particle physics experiments, GEANT: user guide and reference manual* (CERN, Geneva, 1978).
- <sub>2625</sub>
- <sub>2626</sub>
- <sub>2627</sub> [276] R. Brun *et al.*, (1994).
- <sub>2628</sub> [277] ALICE, S. Acharya *et al.*, JHEP **03**, 169 (2019), 1811.09742.
- <sub>2629</sub> [278] Y.-T. Chien and I. Vitev, JHEP **05**, 023 (2016), 1509.07257.